Theses and Dissertations   Graduate School

2016

Diagnostics and Degradation Investigations of Li-Ion Battery Electrodes using Single Nanowire Electrochemical Cells

Naveen kumar reddy Palapati
palapatinkr@vcu.edu

Naveen kumar reddy Palapati
Virginia Commonwealth University, asubramanian@vcu.edu

Copyright

2016

Naveen kumar reddy Palapati

Diagnostics and Degradation Investigations of Li-Ion Battery Electrodes using Single Nanowire Electrochemical Cells

A dissertation submitted in partial fulfillment of the requirements for the degree of Doctor of Philosophy at Virginia Commonwealth University

By

NAVEEN KUMAR REDDY PALAPATI

Bachelor in Mechanical Engineering – GRIET/JNTU, Hyderabad, India, 2008

Director: ARUNKUMAR SUBRAMANIAN, Ph.D.
Assistant Professor
Department of Mechanical and Nuclear Engineering
School of Engineering
Virginia Commonwealth University

Virginia Commonwealth University
Richmond, Virginia
June 2016

Dedication

This dissertation is gratefully dedicated
To my parents,
Sister,
Beloved grandparents,
And all of my friends,
Without whom none of my success would be possible.

I hope that this achievement will bring eternal peace to my late grandfather Palapati Subba Reddy.

Candidate's Certificate

I hereby declare that the work presented in this dissertation is original and was performed by me in the Laboratory of Integrated Nanosystems under the supervision of Dr. Arunkumar Subramanian, Assistant professor in the Department of Mechanical and Nuclear Engineering, Virginia Commonwealth University, Richmond, Virginia. This dissertation work has not been submitted for a degree to any other University or Institution.

_____

Naveen kumar reddy Palapati

Acknowledgements

Firstly, I would like to thank all the people who have helped me and gave moral support in working on my research project.

I would like to thank my supervisor Dr. Arunkumar Subramanian for providing me such an opportunity to conduct research under his guidance. I would like to thank the funding agencies that provided financial support for completing my Ph.D. research study. I would also like to thank the financial and technical support given to me by the Department of Mechanical and Nuclear Engineering. A very special thanks to Dr. Karla Mossi.

I would like to gratefully acknowledge the materials research group of Dr. Ekaterina Pomerantseva and her student Bryan Byles, from Drexel University, for providing us with the nanomaterials to conduct research on understanding the nanomaterial behavior of manganese oxide materials for lithium-ion battery applications.

In addition, I would like to thank my committee members, Dr. Ram Gupta, Dr. Daren Chen, Dr. Indika Arachchige, Dr. Wei-Ning Wang, and Dr. Gokul Vasudevamurthy from VCU, Dr. Ganapathi Subramania from Sandia National Labs for happily agreeing to serve in my committee and sharing their valuable thoughts about my research.

At this time, I would like to thank several contributors who have worked along with me in several different projects: Dr. Ram Gupta from Chemical and Life Science Engineering, VCU and his student Muslum Demir, Dr. Supriyo Bandopadhyay from Electrical and Computer Engineering, VCU and his student Dr. Iftekhar Hossein, Dr. Daren Chen from Mechanical and Nuclear Engineering, VCU and his student Di Liu, and Dr. James T. McLeskey from Randolph-Macon College.

I wish to thank my former and current lab mates for their help and support in completing the tasks, and providing valuable feedback and positive suggestions.

I would like to extend my support to Dr. John Nogan, Integration Lab Manager, and James, Anthony R from Sandia National Laboratories, Dr. Dmitry Pestov and Dr. Carlos Castano Londono from the Nanomaterials Core Characterization facility, VCU, Dr. Gary Atkinson and Josh Starliper from the Virginia Microelectronics Center, VCU for helping me in getting trained on equipment, and providing me with their valuable thoughts and ideas in accomplishing my research tasks. Also, I would like to thank Dr. Vamsi Yadavalli from Chemical and Life Science Engineering, VCU for his help in getting me trained on AFM.

Lastly, I would like to thank again my parents for believing in me and giving me the freedom to pursue my interests.

Table of Contents

Chapter 5. Nanomechanical Characterization

Chapter 6. Degradation Study

List of Figures

List of Abbreviations

Abstract

Fig: Single NW Electrochemical Device

Portable energy storage devices, which drive advanced technological devices, are improving the productivity and quality of our everyday lives. In order to meet the growing needs for energy storage in transportation applications, the current lithium-ion (Li-ion) battery technology requires new electrode materials with performance improvements in multiple aspects: (1) energy and power densities, (2) safety, and (3) performance lifetime. While a number of interesting nanomaterials have been synthesized in recent years with promising performance, accurate capabilities to probe the intrinsic performance of these high-performance materials within a battery environment are lacking. Most studies on electrode nanomaterials have so far used traditional, bulk-scale techniques such as cyclic voltammetry, electrochemical impedance spectroscopy, and Raman spectroscopy. These approaches give an ensemble-average estimation of the electrochemical properties of a battery electrode and does not provide a true indication of the performance that is intrinsic to its material system. Thus, new techniques are essential to understand the changes happening at a single particle level during the operation of a battery.

The results from this thesis solve this need and study the electrical, mechanical and size changes that take place in a battery electrode at a single particle level.

Single nanowire lithium cells are built by depositing nanowires in carefully designed device regions of a silicon chip using Dielectrophoresis (DEP). This work has demonstrated the assembly of several NW cathode materials like $LiFePO_4$, pristine and acid-leached α-MnO_2, todorokite – MnO_2, acid and nonacid-leached $Na_{0.44}MnO_2$. Within these materials, α-MnO_2 was chosen as the model material system for electrochemical experiments. Electrochemical lithiation of pristine α-MnO_2 was performed inside a glove box. The volume, elasticity and conductivity changes were measured at each state-of-charge (SOC) to understand the performance of the material system. The NW size changes due to lithiation were measured using an Atomic Force Microscope (AFM) in the tapping mode. Electronic conductivity changes as a function of lithiation was also studied in the model α-MnO_2 NWs and was found to decrease substantially with lithium loading. In other measurements involving a comparison between the alpha and todorokite phases of this material system, it was observed that the rate capability of these materials is limited not by the electronic but, by the ionic conductivity.

Mechanical degradation of a battery cathode represents an important failure mode, which results in an irreversible loss of capacity with cycling. To analyze and understand these degradation mechanisms, this thesis has tested the evolution of nanomechanical properties of a battery cathode. Specifically, contact-mode AFM measurements have focused on the SOC-dependent changes in the Young's modulus and fracture strength of an α-MnO_2 NW electrode,

2

which are critical parameters that determine its mechanical stability. These changes have been studied at the end of the first discharge step, 1 full electrochemical cycle, and 20 cycles. The observations show an increase in Young's modulus at low concentrations of lithium loading and this is attributed to the formation of new Li-O bonds within the tunnel-structured cathode. As the lithium loading increases further, the Young's modulus was observed to reduce and this is hypothesized to occur due to the distortions of the crystal at high lithium concentrations. The experimental-to-theoretical fracture strength ratio, which points to the defect density in the crystal at a given stoichiometry, was observed to reduce with electrochemical lithium insertion / cycling. This capability has demonstrated lithiation-dependent mechanical property measurements for the first time and represents an important contribution since degradation models, which are currently in use for materials at any size scale, always assume constant values regardless of the change in stoichiometry.

Chapter 1. Introduction

1.1) Introduction to batteries:

A battery is a device that performs two basic functions in an alternating fashion: (1) storing electrical energy or charge within its constituent elements during the "charging" process, and (2) delivering the stored energy or charge, on-demand, to an external load during the "discharging" process. Batteries are made up of one or more electrochemical cells, which are connected in a suitable way to generate the desired output voltage and current. This is accomplished by converting the chemical energy stored in their components into electrical energy. The energy capacity and performance life of a battery depends on factors such as size and shape of each cell, chemical reactions at the interface of cathode and anode material with the electrolyte, electrical/mechanical stability of electrodes, chemical stability of the electrolyte, charge capacity of the electrode materials, and operating temperature/ environment [1,2]. Batteries are mainly classified as primary or secondary cells. Primary cells are designed for one-time use, whereas secondary cells can be re-used by charging them with an external power supply. With growing energy needs, it has become increasingly essential to improve the performance of current-generation batteries in terms of their technological performance metrics such as capacity, size, lifetime, safety and environmental sustainability [3–6].

Over the years, many different electrochemical systems have been employed to build batteries. These differ in terms of the underlying electrochemical reaction, ionic charge carrier

concentration, and the electrode/electrolyte material system. The first demonstrated rechargeable battery was the Lead-acid battery, which was invented by Gaston Plante in 1859. This technology is still in use today in automobile and heavy duty appliance batteries. The key drawback with this system is that it is bulky, with high maintenance costs and less energy density[7]. After several years of experiments, NiCd (Nickel-cadmium) batteries emerged as a solution involving an alkaline electrolyte. Because cadmium is toxic, NiMH (Nickel-metal hydride) batteries were proposed in 1989 owing to their improved lifetime and safety characteristics[8]. In recent decades, lithium (Li) metal has also been considered for batteries because of its useful properties such as light weight and high electro-positivity[9]. However, batteries made of pure lithium were found to be unstable and unsafe, as lithium is highly reactive to atmosphere and dendrite formation from Li anodes results in catastrophic failure due to short circuits[10,11]. Because of such explosive properties, lithium has always been extracted from the earth core as lithium minerals, in the form of rocks or from lithium chloride salts.

A key approach to overcome these technological limitations and deliver high-performance electrical energy storage involves the use of a lithium-ion (Li-ion) electrochemistry, which employs a Li insertion anode instead of pure Li metal to improve safety[12]. Unlike a lithium metal battery, a Li-ion battery does not have lithium metal as an electrode but is made of other materials and lithium ions move between the electrodes through the electrolyte in a reversible fashion, thereby generating electricity in an outer circuit. A Li-ion battery has four major components: an anode, a cathode, an electrolyte and a separator. Typical Li-ion batteries have

solid electrodes and a non-aqueous electrolyte[13], while there is emerging research on systems with solid electrolytes and gaseous or liquid electrodes.
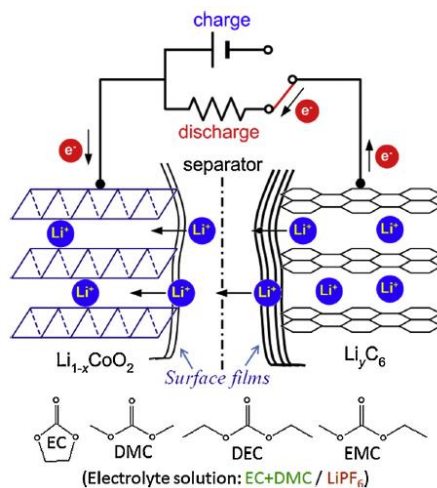
Figure 1.1: Schematic of a Li-ion battery, image reproduced from ref. [14]

In a battery, the anode and cathode perform the roles of the negative and positive electrodes, respectively. An anode material in a Li-ion battery is chosen to have high electro positivity while the cathode material used will decide the voltage and capacity of the battery system. Most of the batteries are manufactured in a discharged state and companies recommend charging the device to full capacity in the first cycle. Li-ion batteries do not accept high initial charging current and need a charger to initially charge it with a constant current profile. During a charging cycle, an external power source supplies the electrons and force the lithium ions to move from cathode to anode, while the opposite reaction occurs during a discharge cycle to deliver power to an external load. This process in which lithium ions are inserted and removed back and forth during the charging/discharging process is also called as the "Rocking chair" mechanism, and the process of inserting Li ions into the material itself is referred to as "lithiation." Figure 1.1 shows the discharge process in a typical Li-ion battery with $LiCoO_2$ and C as the representative cathode and

anode materials, respectively[14]. The electrochemical cycle in this battery can be better understood by the following reactions occurring between LiCoO₂ cathode and C anode[15].

At Cathode:

$$LiCoO_2 \rightleftharpoons Li_{1-x}CoO_2 + x\,Li^+ + xe^- \qquad (1)$$

At Carbon Anode:

$$C + xLi^+ + xe^- \rightleftharpoons Li_xC \qquad (2)$$
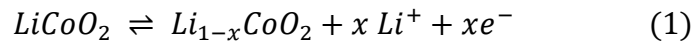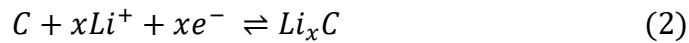
In the above equations, the reaction proceeding from the left hand-side to right hand-side represents the charging process, while the reverse process represents discharging. The total chemical reaction of the cell is given as:

$$LiCoO_2 + C \rightleftharpoons Li_xC + Li_{1-x}CoO_2 \qquad (3)$$
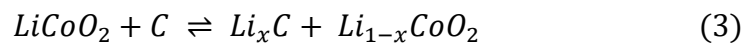
Here x varies between 0 and 1.

Early research was focused on improving the battery system by understanding the redox reactions at the electrode surface, especially at the Li anode where porous deposits are formed. These deposits penetrated the separator barrier between the anode and cathode through the separator, and eventually resulted in short circuiting the battery[16]. This phenomena is often termed as dendrite formation[17]. While the dendrite problem was solved by replacing the Li anode

with other Li insertion materials such as graphite: volume expansion, structural and electronic conductivity changes due to lithiation are still open issues that limit the storage capacity and cycle-life of batteries[18,19]. Newer Li-ion batteries, which solve these problems associated with traditional batteries, are thus essential. Specifically, in order to make this battery system suitable for use in transportation and next-generation portable electronics, improvements are essential in the areas of charge capacity, lifetime performance and safety aspects of today's lithium-ion batteries. Furthermore, it has other disadvantages such as high manufacturing costs and safety issues arising from the explosive nature of the underlying chemical reaction[20]. Current research is focused on delivering improvements in each of these areas and global attention is focused on each component within a battery such as the electrodes, electrolyte, and their packaging.
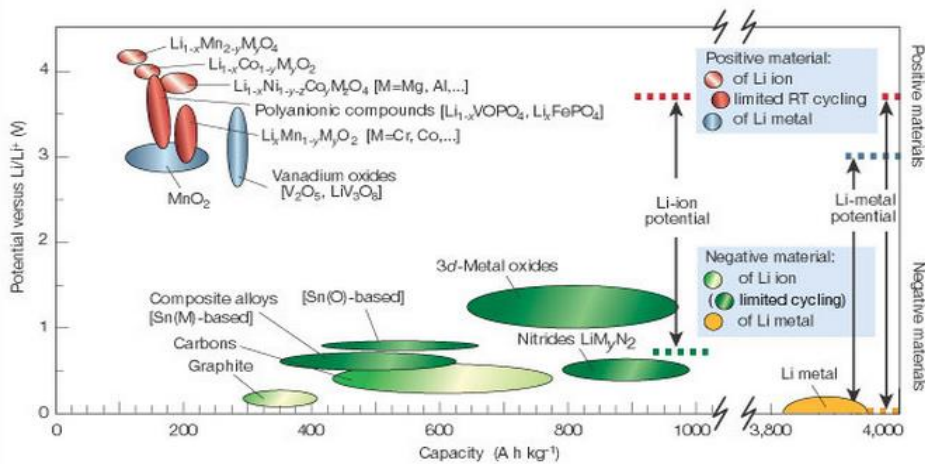
Figure 1.2: Voltage versus capacity for cathode and anode materials, image reproduced from ref. [21]

In order to deliver improvements in the electrode material systems, new knowledge is essential to understand the lithiation-related, electrode material property changes at the atomic-to-nanoscale. The focus of this dissertation is on delivering new knowledge related to the

performance of next-generation electrode material systems. The electrode material system has a key impact on the performance of a Li-ion battery and this is shown using the output voltage vs. capacity chart shown in Figure 1.2 for different electrode materials[21]. Different materials have been studied for use as electrodes in Li-ion batteries in order to increase safety and storage capacity[22–25]. For anodes, early reports indicated the use of carbonaceous materials, including graphite have been implemented[26,27]. But these materials form a passivating layer at the interface of anode and electrolyte, called the Solid electrolyte interface (SEI), and this layer causes instability of the electrode[28]. Other carbonaceous materials were later studied to overcome the problem, but they resulted in high irreversible capacities during the first cycle, which eventually continued for the rest of the cycles. This prompted more studies with different materials such as transition metal oxides, which offer two-to-three time's higher capacity than carbon but, were found to undergo structural degradation due to large volume changes[29]. Lithium alloys were considered much before carbonaceous materials and offered great advantages, but they also exhibited drawbacks related to very large changes in volume. Recently, it was found that reducing their dimensions will considerably help in stabilizing these volume changes in anode materials[30].

Cathode materials also play an equal role in storing and releasing lithium ions in a repeatable manner. Therefore, cathodes are also required to maintain stability during the electrochemical cycling process and it is essential to focus attention on improving their storage capacity as well, just as with anodes (see Figure 1.3 [31] and Figure 1.4 [32]).
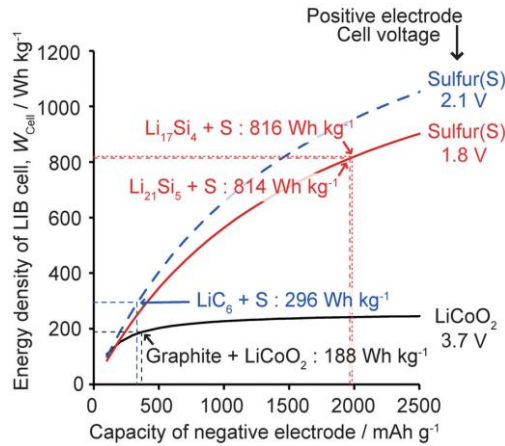
Figure 1.3: Energy density of a LIB cell vs capacity of a negative electrode material, image reproduced from ref. [31]

Battery potential is the electrochemical potential difference between the voltages of cathode and anode materials. Higher the difference in the potential between the two, higher the potential of the battery. Moreover, the output voltage of a LIB cell (W_{cell}) cannot always be improved by just increasing the energy capacity of anode, but depend on increasing the energy capacity of the cathode.
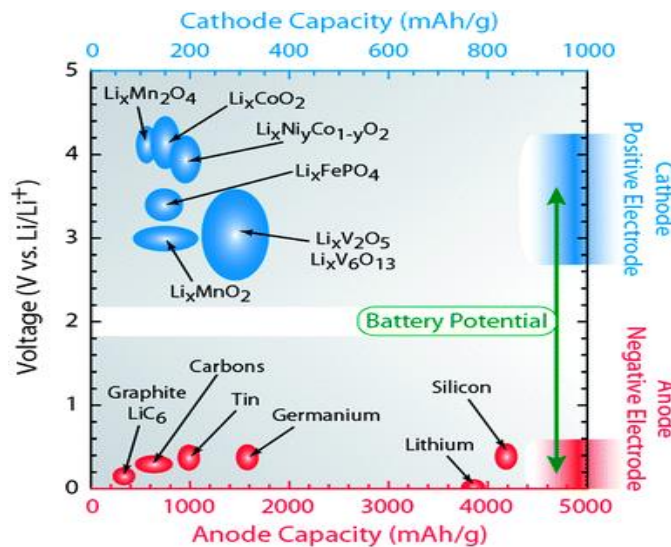
Figure 1.4: Electrochemical reduction potential with reference to Li metal vs. Li-ion capacity for some common anode and cathode materials, image reproduced from ref. [32]

10

From Fig. 1.3, it can be seen that the energy density of the LIB cell remains close to 250 Wh Kg^{-1}, unless the cathode material is changed from $LiCoO_2$ to sulphur. When combined with an anode having lithiated graphite, the energy density increases to 296 Wh Kg^{-1}. Fig. 1.4 gives the energy capacity for various anode and cathode materials.

Layered or crystalline lithium metal oxides were initially studied for cathodes for their high capacity and low manufacturing costs. $LiCoO_2$ was the first cathode material that showed good performance and was used in the commercial Sony battery developed by Goodenough and Mizushima[33]. It is still the most widely used material for cathodes. Because of the low availability of cobalt in the environment, other metals such as manganese, chromium, and nickel etc. were implemented for better use, and to reduce the costs involved in manufacturing[34,35]. Among these, $LiMn_2O_4$ has gained much interest but, it has its drawbacks of low specific capacity and formation of unstable compounds during lithiation. Lithium iron phosphate ($LiFePO_4$) has also been used in commercial batteries for its advantages of safety, high specific capacity and lower costs[36,37]. It has an olivine structure as shown in Figure 1.5, and has a favorable 3D framework with one-dimensional movement of lithium ions. Iron stays in the center during discharge and recharge cycles and forms strong oxygen covalent bonds[37].
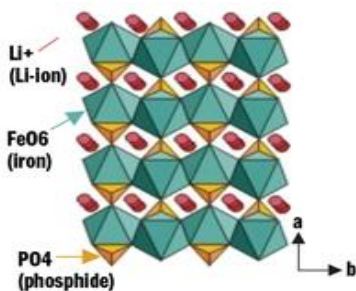
Figure 1.5: Olivine crystal structure of $LiFePO_4$, image reproduced from ref. [37]

Similar to anodes, reducing the dimensions of materials for cathodes has helped in increasing the power density of batteries[38]. Recently, NIST (National Institute of Standards and Technology) developed the world's smallest reference material (RM) 8027 which has a potential use in cathodes of Li-ion batteries[39].

Lithium oxidizes in aqueous solutions to form lithium monoxide (Li_2O) or lithine (LiOH) depending on the reaction with water. Hence, electrolytes need to be non-aqueous and are usually made of organic carbonates like ethylene carbonate or diethyl carbonate in ternary solutions such as lithium hexafluorophosphate ($LiPF_6$), (as shown in Fig. 1.1), lithium perchlorate ($LiClO_4$) , lithium hexafluoroarsenate monohydrate ($LiAsF_6$) , lithium tetrafluoroborate ($LiBF_4$) and lithium triflate ($LiCF_3SO_3$)[40].
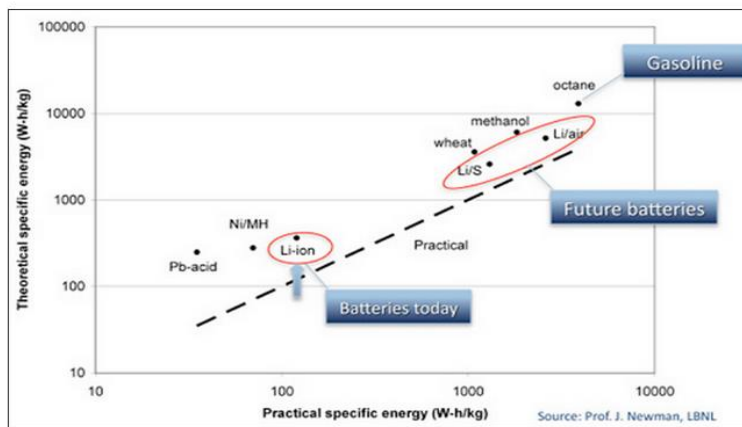
Figure 1.6: Watt-hour per kilogram (W-h/Kg) capacity for various energy sources, image reproduced from ref. [51]

In addition to Li-ion electrochemistry, there are ongoing studies towards building better batteries using other electrochemical systems such as lithium-air[41–43], lithium-oxygen [44,45], lithium-sulphur[46–48], sodium-ion [49,50], and sodium-oxygen (Na-O), among others. These technologies have

the potential to revolutionize the current battery industry, and the estimated storage

performance of these future systems are shown in Figure 1.6 and Figure 1.7 [51,52].
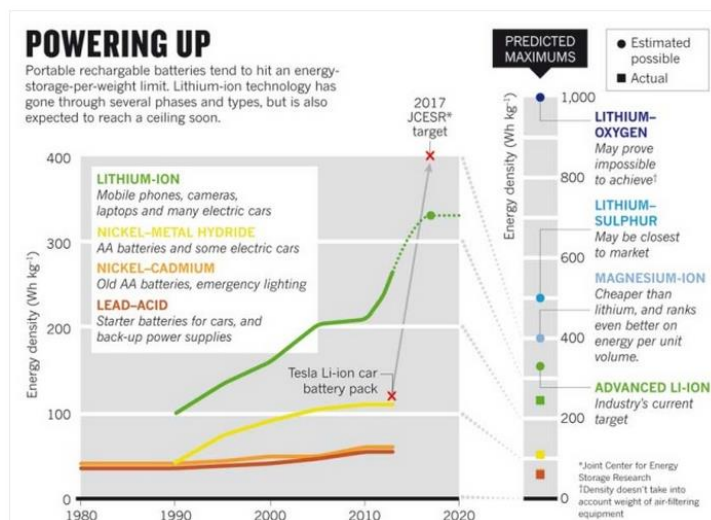
Figure 1.7: The Rechargeable Battery Revolution, image reproduced from ref. [52]

1.2) Nanostructured electrodes for batteries:

There is a need to improve the current state of batteries, especially to be able to reach a position

where batteries can completely replace the automobile engines running on fossil fuels.

Nanotechnology can help in building better and safer batteries at a reasonable cost, because

material properties are different at the nanoscale when compared to their bulk counterparts[53].

Electrodes in a battery are made of mixed ionic or electronic solid conductors, while the

electrolyte is made of an ionic conductor. Since batteries rely heavily on the conductivity of

materials in the cell, it is important to study the ionic behavior of solid materials in detail at a

nanoscale level, the study of which is also termed Nanoionics[54,55]. Li-ion battery performance can

be improved by increasing the reaction rate at which lithium ions are inserted and removed from

an electrode surface. This can be achieved by designing a new material structure, improving

crystallinity and also increasing the diffusivity of lithium ions in the solid state. The current limit for diffusivity of lithium ions in solid state is 10^{-8} cm^2 s^{-1} [56]. The movement of ions in a Li-ion battery depends strongly on its diffusivity (τ) and is given by this equation [57]:

$$\tau = \frac{L_{ion}{}^2}{D_{Li}} \qquad (4)$$

where L_{ion} = Diffusion length, and D_{Li} = Diffusion coefficient.

Diffusion length depends on the geometry of the material while the diffusion coefficient depends on both size and shape of the material. Hence by controlling the size and shape, the rate of diffusion can be controlled[58]. In the case of nanostructured electrodes, the short diffusion paths result in high rates of Li-ion movement and offer high rate capabilities in batteries. The advantages offered by nanosized electrodes in batteries are given below[57] :

- ❖ Increase in surface area of the electrode, thereby providing short diffusion path for ionic transport. This also increases the rate at which lithium ions insert and get removed from the electrodes.
- ❖ High surface area results in increasing the contact area between electrode and electrolyte thereby increasing the rate of reactions.
- ❖ Because of reduced dimensions, there is a change in thermodynamics of some of the reactant materials. Inactive materials such as Li_2O and LiF become reactive at the nanoscale thereby contributing to the increase in reactions.

14

❖ Nanostructures have better structural integrity during intercalation owing to their crystalline or layered properties.

However, using nanomaterials in batteries have some disadvantages such as agglomeration, high inter particle resistance and uncontrolled surface reactions, and research is focused on finding solutions for it[59]. Another major hurdle relates to the manufacturing cost involved in the synthesis of nanomaterials for fabricating the electrodes. At the same time, the goal of the automobile industry is to reduce the cost of manufacturing batteries over half by the year 2020[60]. A recent study by researchers at MIT and 24M company have developed a new manufacturing technique that replaces the conventional solid electrodes with similar semisolid colloidal suspension of particles, thereby reducing the cost of battery by half. This is a promising sign for bright future of Li-ion batteries[61]. Very fast intercalation and de-intercalation process in Li-ion batteries also results in undesired and uncontrolled reactions thereby damaging the battery. This rate of reaction is higher in nanoparticles, even though their structural stability is much better than their bulk counterparts. These limitations to the use of nanomaterials in battery technology are target areas for current research. While this thesis has offered some solutions for these problems, covering every aspect listed here is beyond the scope of this work[62,63].

1.3) Past Research on Nanostructured Electrodes:

Nanomaterials in the form of nanoparticles, nanowires/nanotubes/nanorods, and nanoporous structures have been studied for use in various electrode chemistries in batteries. In addition to

electrodes, nanomaterials in the form of amorphous or crystalline polymers have been used in both solid and liquid state electrolytes to increase mobility and surface charge effects[58,64]. Separators made of nanoporous membranes are used to arrest the movement of dendrites to a major extent between the electrodes, thereby preventing short circuit failure[65]. Nanocoatings for the electrodes were studied to reduce electrode decomposition caused by SEI formation in a carbonaceous anode[66], and in a different study, they were found to increase the capacity of a battery[67]. Figure 1.8 gives a similar idea where a mechanical clamping around a nanowire prevents the formation of SEI layer[68]. Materials such as iron oxide (Fe_3O_4) nanoparticles[69], and carbon nanotubes encapsulated with TiO_2 nanoparticles[70] have shown to produce durable and high rate capable electrodes, which can improve the cyclability of the battery. Also, studies are being made to form various 2D, 3D structures for electrodes[71–77] so as to better accommodate for the volume expansion of these materials during the charge/discharge cycles. Nanostructured materials such as graphene, tin, silicon etc. are now being studied for use as anode material [78–81] and materials such as MnO_2, silicon, carbon and sulphur etc. for use as cathode material[82–85].
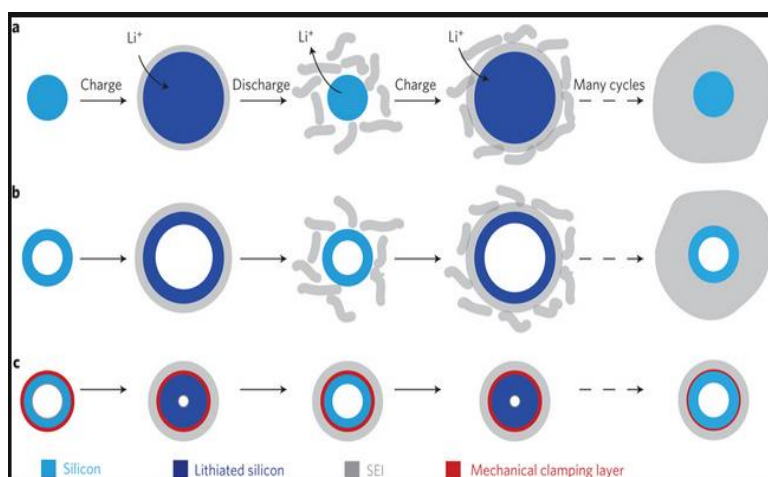
Figure 1.8: SEI formation on Silicon surfaces a) Solid Si nanowire. b) Si nanotube, and
c) Mechanical constraining layer on a Si nanotube, image reproduced from ref. [68]

One dimensional nanostructures such as nanowires, nanorods and nanotubes offer advantages over nanoparticles owing to their anisotropy[86] and to their capability for being single crystalline. They have also been used extensively in other applications such as photovoltaics[87] and nanoelectronics[88]. As discussed in the earlier section, the unique properties of such nanostructures help in improving the performance of current generation Li-ion batteries. Si is perhaps the most studied nanomaterial for use as a battery anode. While Si nanowires retained their high initial capacity of roughly about $4200mAhg^{-1}$ for several charge-discharge cycles, the lithiation process causes a 400% increase in volume[18]. While fracture and cracking in nanostructured silicon is less of a problem as compared to bulk Si, there are other concerns such as large volume changes, reduction in electronic conductivity and elastic softening. Other nanomaterials used for battery components were also found to have similar challenges associated with them, particularly because of stress and strain being induced during cycling. These issues need to be further investigated, if nanomaterials are to be used in future battery electrodes. In terms of cathodes, materials such as hollandite and todorokite were found to provide efficient ionic and electronic pathways in the crystal structure for increased storage of Li^+ and Na^+ ions during lithiation.

Techniques such as cyclic voltammetry[89], galvanostatic cycling[31], electrochemical impedance spectroscopy (EIS)[90,91], Raman spectroscopy[92,93], X-ray photoelectron spectroscopy (XPS)[94], X-ray diffraction etc. were extensively used for understanding the electrochemical change in nanomaterials over several charging/discharging cycles, but the drawback associated with these measurements is that they give an average information on the electrochemical properties in a

bulk-scale quantities of the nanomaterial. Figure 1.9 gives the cyclic charge-discharge curves of a nanopore battery array having V_2O_5 as cathode, pre-lithiated V_2O_5 as anode, ruthenium (Ru) current collector and a conventional 1:1 EC: DEC electrolyte[95].
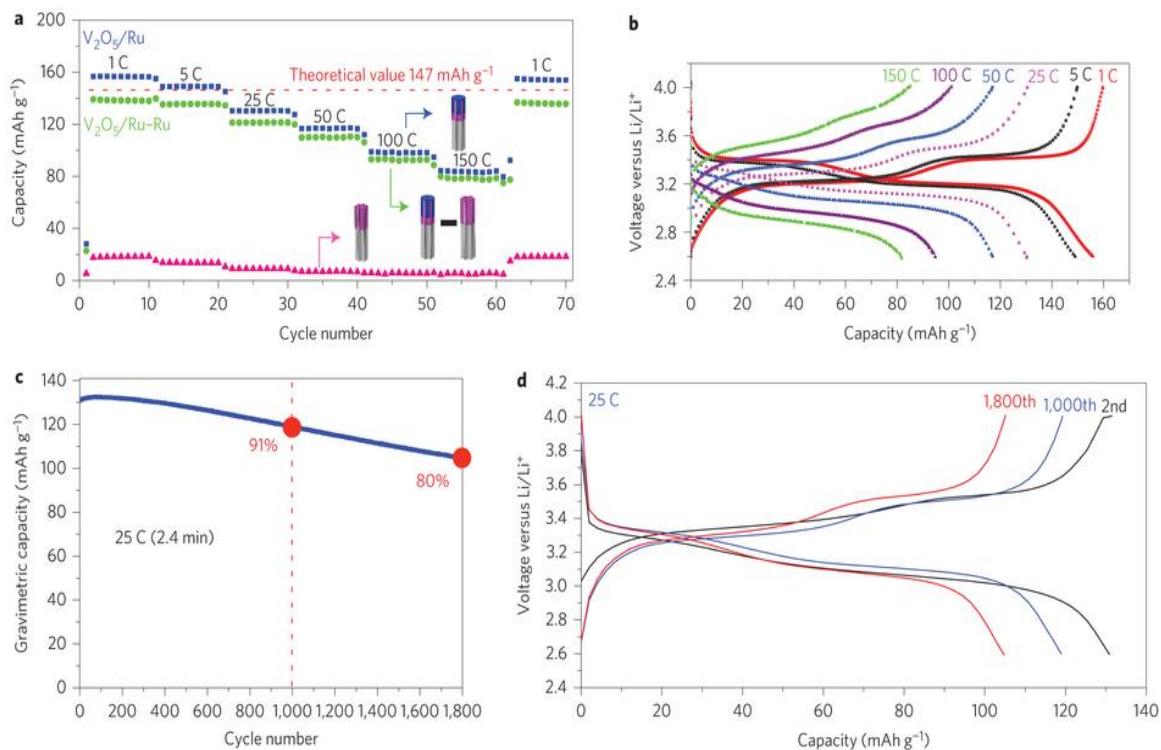
Figure 1.9: Electrochemical charge–discharge of a half-cell device at high-rate cycle life. a) Rate performance of V_2O_5/Ru-nanotube battery (blue), O_3-treated Ru current collector (pink) and pure contribution of V_2O_5 (green). b) Galvanostatic charge–discharge cycling curves of V_2O_5/Ru-nanotube cathode at various C rates. c) V_2O_5/Ru-nanotube cathode has 91% of the original capacity after 1,000 cycles and 80% after 1,800 cycles when cycled at 25 C. d) Charge–discharge curves at the second, 1,000th and 1,800th cycles. Image reproduced from ref. [95]

In order to truly understand the performance of a nanomaterial, these have to be tested for their performance at the single nanowire or particle level. Until recently, there has been a lack of proper techniques to evaluate the fundamental mechanism during electrochemistry in a battery at an individual single nanowire. Huang et al. performed the first electrochemical study inside a

TEM, with a SnO$_2$ nanowire acting as a working electrode in a battery, having LiCoO$_2$ as a cathode, as shown in Figure 1.10[96,97].
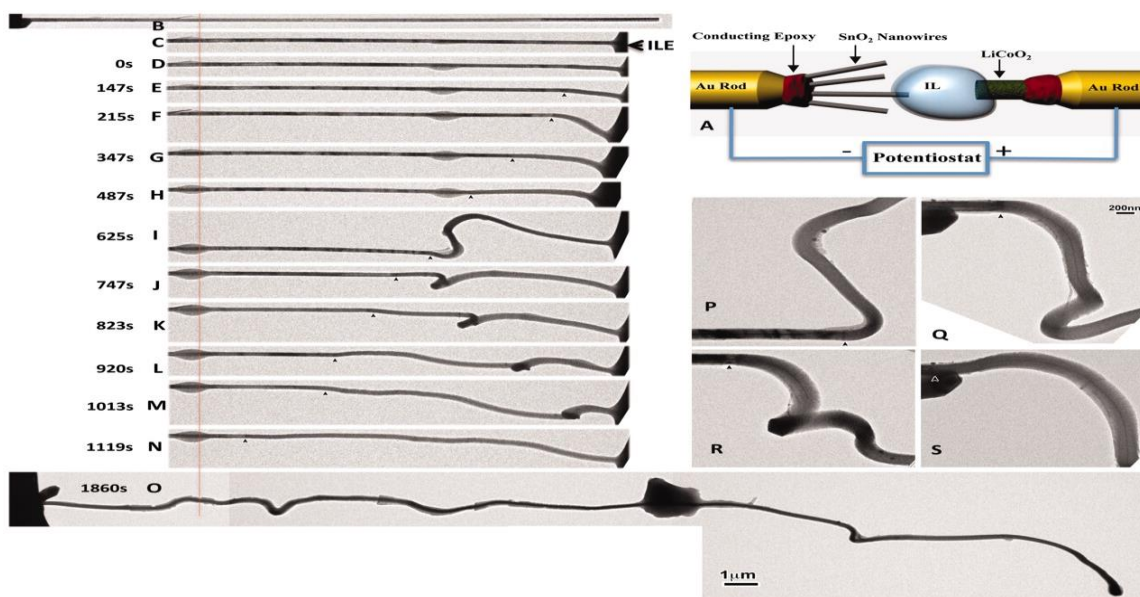
Figure 1.10: Time-lapse structure evolution of a SnO$_2$ nanowire anode during charging at −3.5 V against a LiCoO$_2$ cathode. The single-crystal nanowire was elongated 60% and the diameter increased 45% (resulting in a 240% volume expansion) after charging for 1860 s. (**A**) Schematic of the experimental setup. The initially straight nanowire (**B** and **C**) became significantly twisted and bent after charging (**D** to **S**). The chemical reaction front progressed along the nanowire's longitudinal direction, with the front clearly visible, as pointed out by arrowheads in (E) to (S). The red line in (B) to (O) marks a reference point to track the change of the nanowire length. (P) to (S) are sequential high-magnification images showing the progressive migration of the reaction front, swelling, and the twisted morphology of the nanowire after the reaction front passed by. The big dark particle in the middle of (O) is an island of gelled ILE. Because of the long cumulative electron beam exposure time during the recording of TEM images, the ILE front became gelled (with high viscosity) at this spot. Image reproduced from ref. [96]

This study gave a direct correlation of the properties of the material with its electrochemical lithiation, which means a direct study of the electrochemical reaction inside that material without the influence of any other inactive material such as a binder. There have since been several reports that applied the same principle of in situ TEM study for other materials and electrochemical systems[98–101]. For better understanding of the dynamic changes in properties at the atomic or nanoscale, such single nanowire studies are necessary and can be done using high

resolution equipment such as transmission electron microscopes (TEMs), scanning electron microscopes (SEMs), and atomic force microscopes (AFMs). But the challenge is to create new characterization techniques that can perform these battery diagnostics with high accuracy[101].

1.4) Original contributions of this dissertation:

The previously mentioned in situ TEM technique, however, can only provide the information regarding morphology, structural and compositional changes happening in a material over the life cycle of a battery[102]. For an understanding of the other electrochemistry related changes in a battery electrode such as its electronic conductivity and Young's modulus, the key is to construct a device that has the capability to work as a battery with one single NW as a working electrode and to study the properties of it. There were several reports that tested different properties of several nanomaterials in this way[6,92]. But, most of these studies have targeted anode materials and there are very few reports on cathode materials.

To address this need, Subramanian et al. [103] has recently demonstrated a single nanowire electrochemical cell, which was constructed on silicon chips. This cell integrated a beta-MnO_2 nanowire cathode in the form of a doubly-clamped beam across gold nanoelectrode current collectors. This platform has been used in the past to study the electrical, mechanical, structural and compositional changes in the single nanowire cathode as a function of its lithium content or state-of-charge (SOC). This thesis has used this recently demonstrated on-chip, single nanowire platform to test several new material systems at a single nanowire or nanoparticle level for their

performance in batteries. Specifically, single nanowires of potential cathode materials were deposited on to device regions using the Dielectrophoresis (DEP) technique. While the devices are fabricated in an array, each nanowire location can be individually tested for their electrical and mechanical properties. The fabrication procedure, which involves dielectrophoretic (DEP) assembly, and the factors that control it are discussed in chapter 2.

Chapter 3 presents the electrochemical lithiation results from two different material systems: α-MnO_2 and acid-leached α-MnO_2. The NWs are characterized using SEM and AFM imaging. The tapping mode scans are further analyzed to measure the diameter changes of these nanowires as a function of lithium content inside the electrode material. Also, pure electrolyte dip tests are presented to verify that the changes are caused by electrochemical lithiation and not, due to a chemical reaction.

Conductivity of the material plays a major role in determining the rate capability of a battery. Hence, it is essential to understand the electronic conductivity of the battery material system. This thesis has presented electronic conductivity data for a number of different battery materials at a single particle-level for the first time. This includes measurements from materials such as bio-derived graphitic carbon particles, α-MnO_2, acid-leached α-MnO_2 and todorokite-MnO_2. Also, the changes in conductivity with lithiation are measured for the α-MnO_2 and acid-leached α-MnO_2 NW system. Detailed information on this experimental procedure and its results are discussed in chapter 4.

Chapter 5 presents the nanomechanical measurements performed on single NW cathodes. These measurements are performed to obtain the Young's Modulus (YM) and ultimate strength of the electrodes. These material properties are essential to study the lithiation induced stresses and mechanical failure in battery materials. This work has determined the YM for two different material systems at the single NW level for the first time. These include LiFePO$_4$, and α-MnO$_2$ NWs.

Mechanical degradation of a battery cathode represents an important failure mode, which results in an irreversible loss of capacity with cycling. To analyze and understand these degradation mechanisms, this thesis has tested the evolution of nanomechanical properties of a battery cathode and these results are presented in Chapter 6. Specifically, contact-mode AFM measurements have focused on the SOC-dependent changes in the Young's modulus and fracture strength of an α-MnO$_2$ NW electrode, which are critical parameters that determine its mechanical stability. These changes have been studied at the end of the first discharge step, 1 full electrochemical cycle, and 20 cycles.

Chapter 7 presents the main conclusions and recommendations, which have emerged from this doctoral dissertation.

Chapter 2. Single NW Battery Device

2.1) Device Overview:

The single NW devices are constructed on silicon wafers. Each wafer produces around 200 chips, and Figure 2.1 shows the electrode and device regions on one such chip [103]. The fabricated chip has an array of 200 to 400 devices. The devices have a common large pad on the left to which all the electrode pairs are connected. Each electrode pair has a gap ranging between 400nm to 1000nm between them. The height of the pads is about 100 nm from the silicon nitride substrate surface. Each device has a single pad, which is capacitively coupled to the left pad, on the right hand side and this works as an individual terminal for single NW electrical measurements.
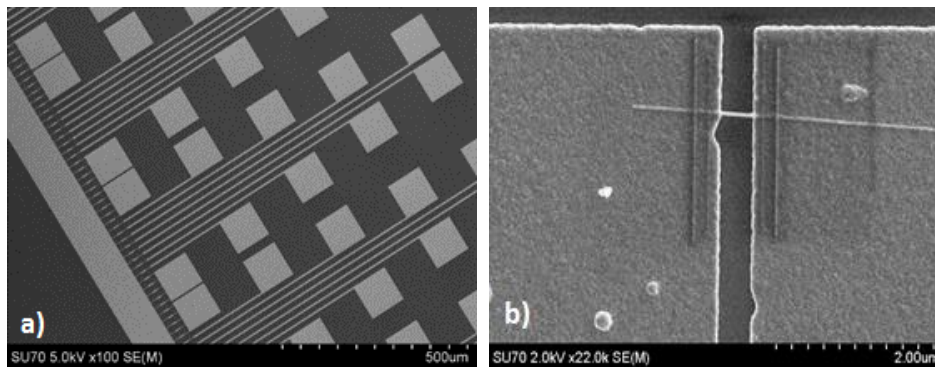
Figure 2.1: a) SEM Image of fabricated chip with one large electrode on the left, individual pads to the right. b) SEM Image of one location with α-MnO$_2$ NW, clamped using EBID.

2.2) Dielectrophoresis:

Dielectrophoresis or DEP is the process in which any neutral particle, when placed in a non-uniform field experiences a dipole moment, and becomes polarizable. The force of this dipole

moves the particle in the direction of field maxima. From the fundamentals of physics, it is understood that a positively charged particle is attracted to and moves towards a negative field whereas a negatively charged particle moves towards a positive field. In both cases, the movement of the particle will be in the direction of position of maximum field. In Figures 2.2 and 2.3, the particle will always move to the left because of the presence of strong field. Positive field is maximum in Fig. 2.2, while the negative field is maximum in Fig. 2.3[104]. Also, DEP is independent of the type of applied field, which means that the movement of a polarized particle will always be in one direction, irrespective of whether it is AC or DC in nature. When a DC source is connected to the positive terminal, the particles always move towards the left pad. Similarly, when an AC source is connected, there will be alternative positive and negative maxima on the left pad and so the movement of the polarized particle will always be to the left. Also, the particle need not be conductive to undergo these effects. As long as the particle is polarizable in an applied field, it will move in the direction of field maxima.
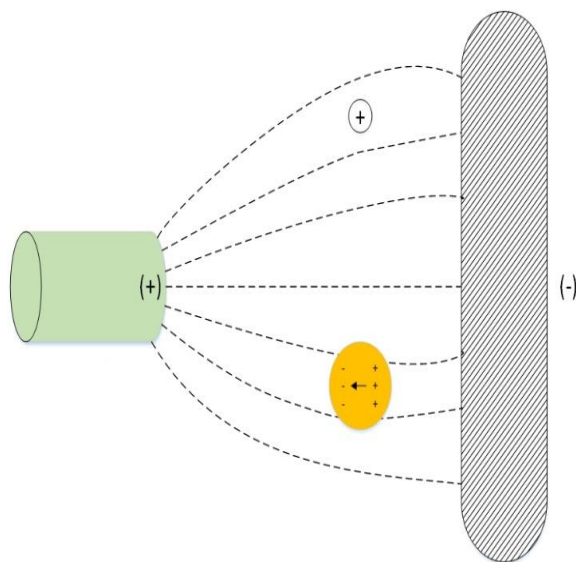
Figure 2.2: Particles move towards Positive maxima – DEP,
Image redrawn using ref. [104].
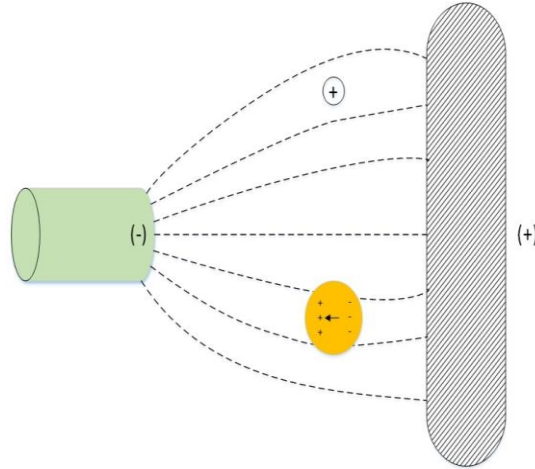
Figure 2.3: Particles move towards Negative maxima – DEP,
Image redrawn using ref. [104].

The DEP force is inversely proportional to the distance of the particle from the electrodes. DEP is dependent on the following parameters: voltage, time, frequency, shape of field regions, gap between positive and negative terminals, shape and size of particle, and initial contact position[105,106] . The time averaged DEP force acting on an ellipsoid particle in a medium is given by this formula[107].

$$< F_{DEP} > = \frac{1}{2} \left[Re(\tilde{p}.\nabla)E^* \right] = \frac{1}{2} v \, Re[\widetilde{\alpha}]\nabla(E.E^*) \qquad (5)$$

$$= \frac{3}{2} \pi r^2 l \; \epsilon_m \, Re \left\{ \frac{\epsilon_p^* - \epsilon_m^*}{\epsilon_m^*} \right\} \nabla |E|^2 \qquad (6)$$

where

V = Volume of nanowire $= \pi * r^2 * l$

a, b, c = half-length of major ellipsoid axes

α = Term for polarizability of the body = $3*\epsilon_m*K$

ε^*_p = Complex Permittivity of particle

ε^*_m = Complex Permittivity of medium

E = External Electric field intensity

∇ = Gradient
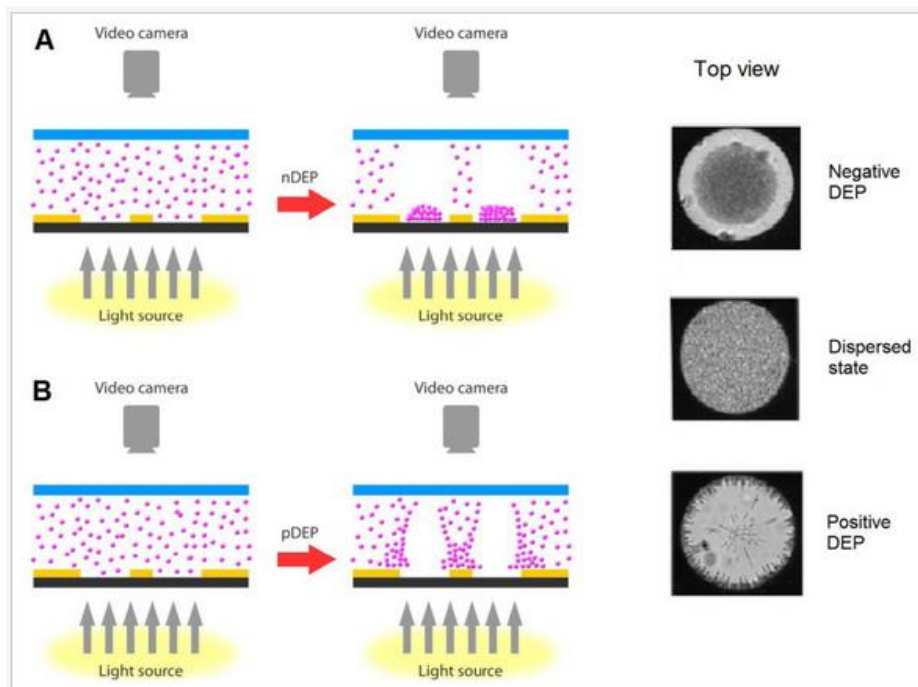
Figure 2.4: Dielectrophoresis - A) Negative DEP, and B) Positive DEP, image reproduced from ref. [108]

Some other applications for DEP based on non-uniform electric fields are listed below:

- ❖ Separate live from dead cells

- ❖ Pollution control

❖ Maser or laser control

❖ Fresh water treatment

❖ Particulate matter separation

❖ Fabrication based application: nanowire based gas detectors, micro-nanosensors, transistor gates, diode, photovoltaics etc.

Figure 2.4 gives an example for the use of dielectrophoresis in dispersing live yeast cells in a dot micro system[108]. Here, the particle movement is influenced to occur in the positive or negative DEP regime, depending on the control parameters.

2.3) Device Fabrication:

Most steps in the chip nanofabrication process were performed at the Sandia-Los Alamos Center for Integrated Nanotechnologies (CINT), a U.S Department of Energy, Office of Basic Energy Sciences user facility in Albuquerque, New Mexico. This facility was chosen because of the availability of sophisticated laboratory equipment's such as an advanced Electron beam lithography system (JEOL 6300FS), versatile Electron beam deposition system (Temescal FC-2000) etc. The fabrication process starts with a 4 inch, 450 µm thick silicon wafer and results in ≈ 200 chips per wafer. The chips contain different electrode designs and have dimensions of 4 mm x 6 mm.

First step in the fabrication process is to deposit a 200nm low stress silicon nitride film on the silicon wafer. Silicon nitride is chosen instead of silicon oxide to assist further fabrication steps, which involves the use of strong acids such as sulfuric acid and the use of strong bases like TMAH. Each wafer is subjected to two steps of photolithography. First step results in gold pad and connecting line fabrication. Here, chromium acting as an adhesion layer. This step consists of photolithography followed by metal deposition and lift-off. The second step consists of an etching of silicon nitride in select regions to provide contact to the silicon substrate. The third and final step involves electron beam lithography (EBL) definition of gold nanoelectrodes in the device region with an accuracy in the range of tens of nanometers. Here, the wafer is developed, deposited with metal and finally a lift-off step is performed to remove the unwanted and excess metal on the wafer. Once this is complete, the wafer is coated with a layer of photo resist, attached to a tape and diced into individual chips, each having a dimension of 4mm in width and 6mm in height. These wafers are vacuum sealed and transported to VCU for carrying out further experiments. A small portion of the photo resist layer remains on the wafer after dicing and prevents the chips from getting contaminated from any kind of particulates until they are ready for use.

2.4) DEP Experimental Procedure:

A single nanowire is deposited across the left and right pads using DEP, which is explained next. To realize the electrical circuit for DEP, a negative potential is applied to the substrate (Ground Electrode G) while all the right side individual electrodes (Electrode F) are at a floating potential.

A positive potential or biasing potential is applied to the large left pad (Electrode B). A liquid droplet, with nanowires suspended in it, is poured on top of the chip. Because of the difference in permittivity of the nanowire with respect to the medium, the nanowires get polarized, align in the direction of the field and are attracted towards electric field maxima. An AC signal drives this DEP process and Figure 2.5 shows the equivalent electrical circuit[109] .
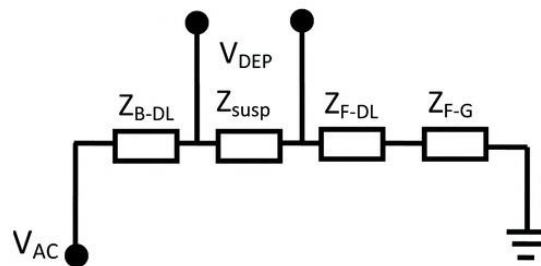
Figure 2.5: Equivalent Electrical circuit, image reproduced from ref. [109]

Since the biasing electrode and floating electrode come in contact with liquid suspension, there exists a double layer capacitance between the electrode and liquid. This is shown by the impedance terms Z_{B-DL} and Z_{F-DL}. In addition, there is impedance between the suspension and bias electrode (Z_{susp}). Finally, there is impedance offered by the capacitive coupling between gate and floating electrodes (Z_{F-G}). By calculating the magnitude of these individual components, it is possible to evaluate the current or voltage acting on each individual nanowire in the device region.

The experimental setup for Dielectrophoresis is shown in Figure 2.6.[110]
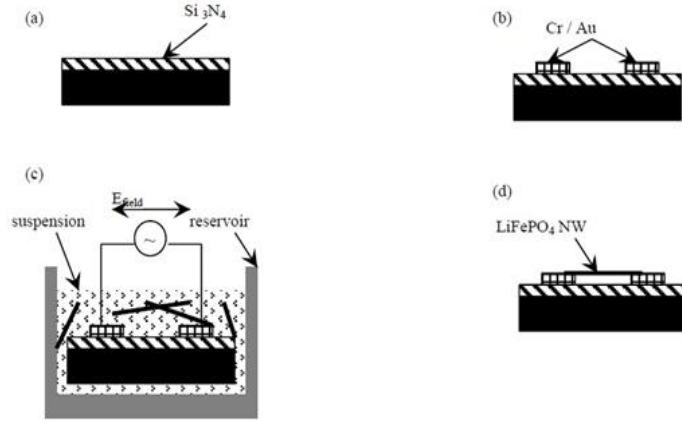
Figure 2.6: Experimental Setup for dielectrophoretic assembly process a) Si$_3$N$_4$ deposited on a silicon substrate. b) Definition of gold Nanoelectrodes. c) Assembly of LiFePO$_4$ NWs using AC Dielectrophoresis. d) NW bridging the gap in the electrode region, image reproduced from ref. [110]

2.5) Sub-crossover Frequency Regime:

The time-averaged DEP force acting on a nanomaterial, given by equation 5 has a complex parameter "K" in it, which gives the relative polarizability of the NW with respect to the medium. This term is also called as the "Clausius-Mossotti" factor, given by this equation:

$$K(\omega) = \frac{\tilde{\varepsilon}_{NW} - \tilde{\varepsilon}_m}{\tilde{\varepsilon}_m} \qquad (7)$$

Where $\tilde{\varepsilon}_{NW}$ represent the complex permittivity of the nanowire, $\tilde{\varepsilon}_m$: the permittivity of the medium.

The complex permittivity is in turn given by this equation, where it is dependent on real dielectric permittivity (ϵ), conductivity (σ) and frequency (ω).

$$\tilde{\varepsilon} = \varepsilon - i\frac{\sigma}{\omega} \qquad\qquad (8)$$

Positive DEP and negative DEP effects can be visualized from an earlier Fig. 2.4, where positive DEP attracts the particle close to the gap region, and negative DEP repels it from the gap. This effect depends on how polarizable a particle is with respect to the medium, and is given by the Clausius-Mossotti factor (K). When the real part of K term in equation 7 is greater than zero, it results in positive DEP and is negative otherwise. To understand the effect of frequency, voltage and time, which are the three major factors that control DEP, several experiments were performed with α-MnO$_2$ nanowire system. A design of experiments was performed to understand the role of these parameters. To start with, a voltage of 1V$_{P-P}$ was applied over a deposition time of 2min. At this condition, the frequency was varied between 10 mHz and 20 MHz to estimate the "fill-factor" for these nanowires. Fill-factor is a term that represents the number of electrode locations (out of a total of 100), where there are one or more nanowires either bridging the gap, cantilevered or overlapping. Figure 2.7 (a) gives the fill factor values for this variable frequency study and it also includes data for "single NW" deposition[109]. "Single NW" condition represents the locations where an individual nanowire is perfectly suspended within the gap region at each condition. As it can be seen from Figure 2.7 (a), the fill-factor was maximum at 100 kHz frequency, and there was no observed deposition after 20 MHz. Hence, 20 MHz was the "crossover frequency" (f$_{CO}$) for this material system. It represents the frequency

below which, the DEP is always positive. The curve in the figure is a plot of the Clausius-Mossotti factor as a function of frequency using equation 7.
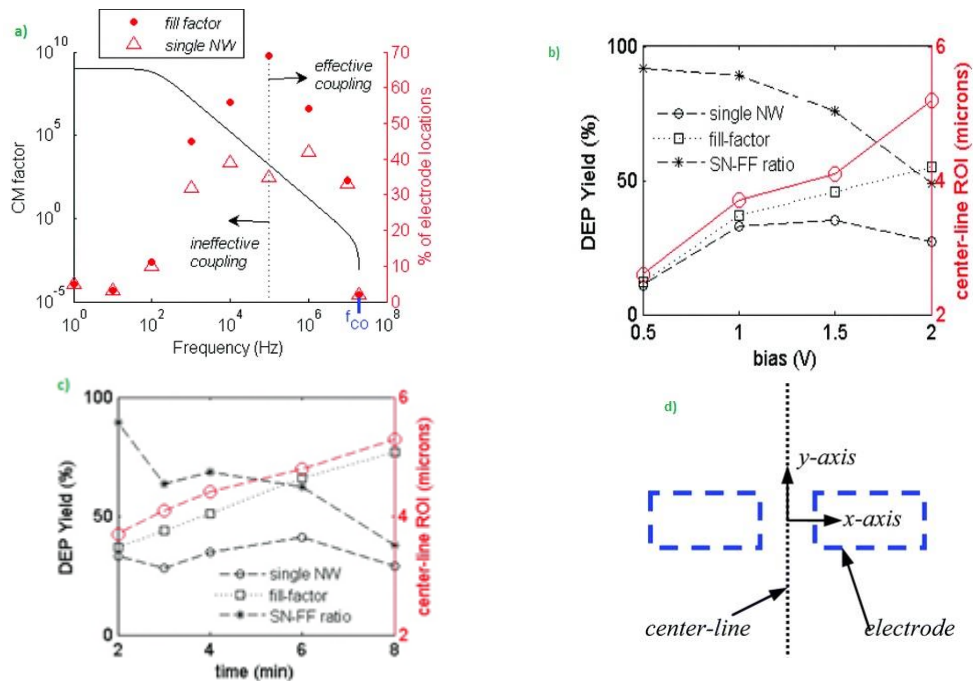
Figure 2.7: a) Clausius-Mossotti factor vs Frequency, f_{CO} – Crossover frequency. b) DEP as a function of applied bias (V). c) DEP as a function of time (min). d) Electrode design showing inter-electrode center line [109]. The computational models in these figures (related to CM factor and ROI calculations) were performed by Dr. Subramanian.

Similarly, the experiment is repeated to estimate the effect of AC bias and deposition time on DEP. A 10 MHz frequency was chosen to perform these experiments as the DEP force (the parameter which moves the nanowire towards the electric field maxima) at this frequency is not too high and enables effective control over the movement of single nanowires in the electrokinetic region of influence. In the next set of experiment, the deposition time remained fixed at 2min, while the voltage is varied between 200mV to 2V. The "fill-factor" and "single NW" results from these experiments are shown in Figure 2.7(b). It can be seen that with increasing voltage, the fill factor increases as the DEP force is larger thereby, attracting more nanowires to

the gap region. Ideally, the field reduction after the first NW deposition should be large enough to prevent the possibility of additional nanowires being attracted. However, this is not always the case if there are other nanowires situated in closer proximity to the electrodes, which exert sufficient fields at high AC voltages to attract them. As a result, there is decrease in the single-nanowire to fill-factor ratio with increasing voltage.

Finally, to estimate the effect of time on DEP, another set of experiments are performed where the frequency and voltage are kept constant, while varying the DEP time between 2min and 8min. These results are shown in figure 2.7 (c) and it can be observed that the fill-factor and single NW depositions increase with time, as the nanowires get sufficient time to get attracted to the electric field maxima at the electrode edges. While the device geometry is three-dimensional, which is difficult to estimate, a two-dimensional approximation has been performed to study the variation of electrokinetic region of influence under these different deposition conditions. While the experimental results presented here are a part of this thesis, the computational models were performed by Dr. Subramanian. Here, the axial region of influence is defined along the inter-electrode center line as shown in figure 2.7 (d). By drawing a hemisphere with a radius equal to R_{ROI} along the electrode center line, the volumetric ROI over which the electric fields exert influence on the nanowires within the suspension can be written in this form:

$$V_{ROI} = \frac{2}{3} \pi R_{ROI}{}^3 \qquad (9)$$

The capture time for a nanowire in a suspension typically ranges from milliseconds to several minutes depending on the configuration. Using the computational model, it was found that the capture time for a nanowire located at a 5μm distance from the center line varied from 11.38 micro seconds to 0.71 micro seconds at low frequencies such as 1 kHz (when the bias changed from 0.5V to 2V) [109]. This deposition time is 8 to 10 orders of magnitude smaller than the sub-crossover regime of 10 MHz under similar conditions. These small capture times at low frequencies in particular will be difficult to control for getting single nanowire depositions. Hence, finding parameters that work within the sub-crossover range for any material system will yield better results.

This work has identified appropriate deposition conditions for successful DEP assembly of multiple nanomaterial systems. These include LiFePO$_4$ NWs (synthesized by Dr. Chunsheng Wang's lab at the University of Maryland), bio-derived sub-micron carbon particles (synthesized by M. Demir at Dr. Ram Gupta's lab at VCU), pristine and acid-leached α-MnO$_2$ particles (synthesized by Dr. Pomerantseva's lab at Drexel University), pristine and acid-leached Na$_{0.44}$MnO$_2$ NWs (synthesized by Dr. Pomerantseva's lab at Drexel University), N$_2$ doped CNTs, and InSb, InSb-Cr, Ni-InSb-Ni tri-layer NWs (synthesized by Dr. Bandyopadhyay's lab at VCU), among others. SEM images showing these deposition results are shown in Figure 2.8.
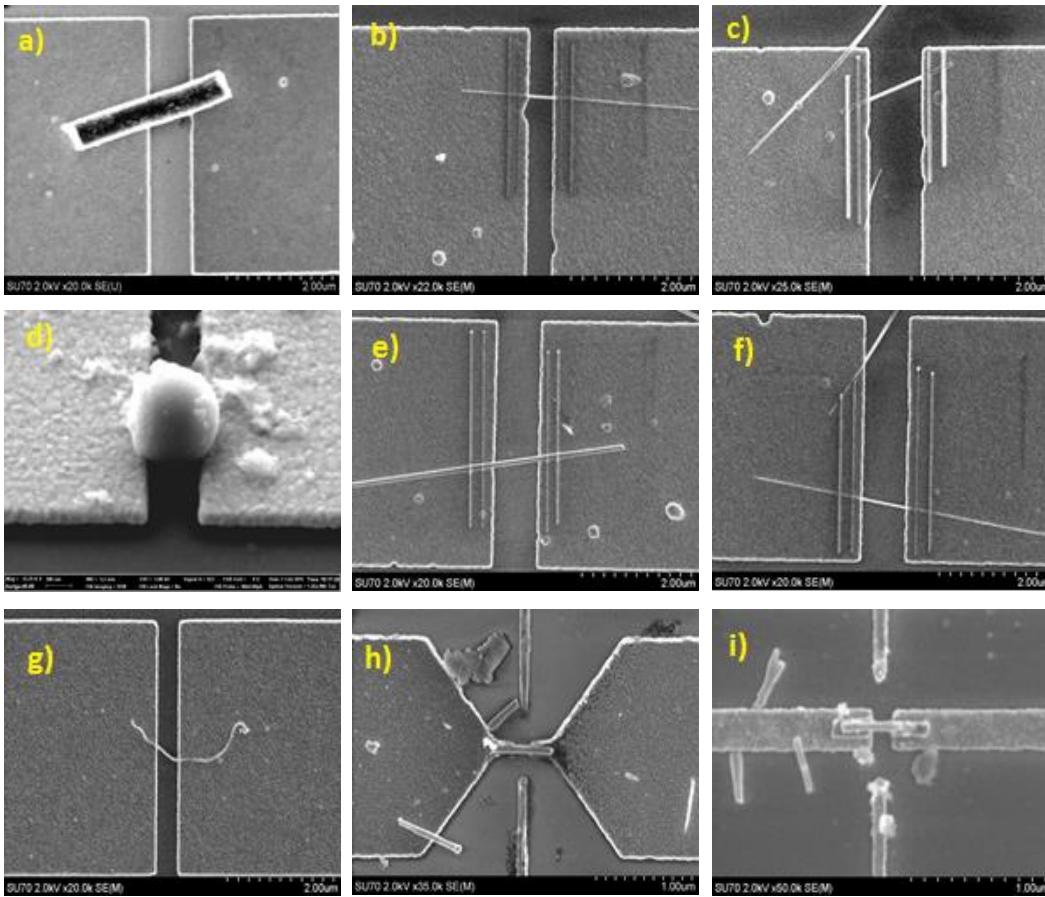
Figure 2.8: SEM images of a) LiFePO$_4$ NW, b) α-MnO$_2$ NW, c) acid-leached α-MnO$_2$ NW, d) GC1000 nanoparticle, e) Na$_{0.44}$MnO$_2$ NW, f) acid-leached Na$_{0.44}$MnO$_2$ NW, g) N$_2$ doped CNT, h) InSb NW, and i) Ni-InSb-Ni tri-layer NW in a 3D electrode configuration.

Chapter 3. Electrochemical Characterization

3.1) Rationale and Background:

During the course of electrochemical reaction, electrodes typically undergo structural and/or phase changes, often accompanied by changes in electrical and mechanical properties. This causes a reduction in storage capacity due to a loss of contact with current collectors or due to the mechanical failure of the electrode particles. As a result, there has been interest in studying the capacity fading mechanism and its causes at a single nanoparticle level[111]. There have been past reports on in-situ lithiation experiments[112–116], with many of these reports focusing on the use of nanostructured anode materials[96,117,118]. In the case of nanostructured materials for cathodes, studies were mostly limited to synthesis techniques[119,120]. Among them, very few have actually focused on understanding the behavior of cathodes at a single nanomaterial level[74,121–123].

Currently, most of the Li-ion batteries use $LiCoO_2$ as the cathode, and there is a need to replace this material system with other materials because cobalt (Co) is not very abundant in the earth's crust, and also high costs are involved in mining cobalt from the ore. MnO_2 is environmentally stable and has high initial capacity[124]. Moreover, it is also non-toxic in nature, and these properties make it the most promising material system for testing its compatibility in use of Li-ion batteries. Based on the way, the structural unit MnO_6 octahedra arrange themselves and get linked, there are different polymorphs of MnO_2[125], mainly α-, β-, γ-, δ-, OMS-6 and todorokite-

MnO_2, where α-, β-, γ-, todorokite types have tunnel crystal structure, δ- have a layered structure and λ- have 3D structures . Recently, a single NW electrochemistry platform has been designed and demonstrated for studying the performance of cathodes. This platform, which was demonstrated at the Center for Integrated Nanotechnologies (Sandia Labs), enables the measurement of the structural, mechanical and electrical properties as a function of lithiation[103]. This thesis has used this platform to study the electrochemical performance of two new material systems: α-MnO_2 and acid-leached α-MnO_2. This chapter presents this experimental set-up and the lithiation-induced changes, which were observed in the two material systems.

3.2) Experimental Procedure:

The setup for lithiation, which can be used with any type of nanowire electrode, is shown in the Figure 3.1. The negative terminal here is connected to a lithium metal (anode). Pure lithium is explosive and hence, the experiment is performed inside a glove box. The post-lithiation AFM experiments were done in air without harm, since the lithium in the material is in an oxidized state. Geometric changes are evaluated using an Atomic force microscope (AFM).
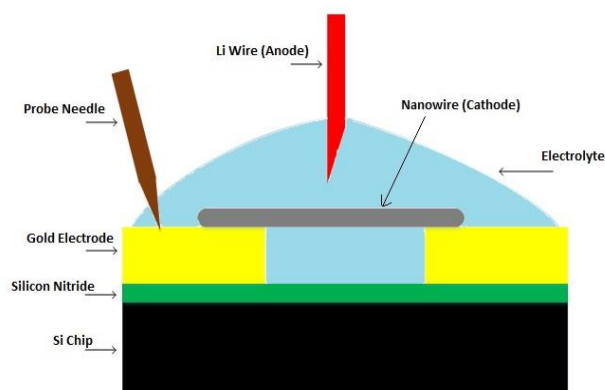
Figure 3.1: Lithiation setup, Electrolyte: EC: DMC (1:1)/LiPF6

The α-MnO$_2$ material system has been used in this study, since it has demonstrated high initial capacity as a battery cathode. However, the cyclability of this material is poor and hence, the goal of this thesis is to understand the changes in this material system, which cause this behavior. The crystal structure of α-MnO$_2$ is shown in Figure 3.2[126]. This illustration does not show the stabilizing potassium ions, which are located in the tunnels, for simplicity. This material is of interest for battery electrodes since it has vacant structural tunnels that can hold lithium ions during intercalation. In the case of the NW material used in this thesis, which has been synthesized by the Pomerantseva group at Drexel University, the tunnels run along the longitudinal axis of the wires.
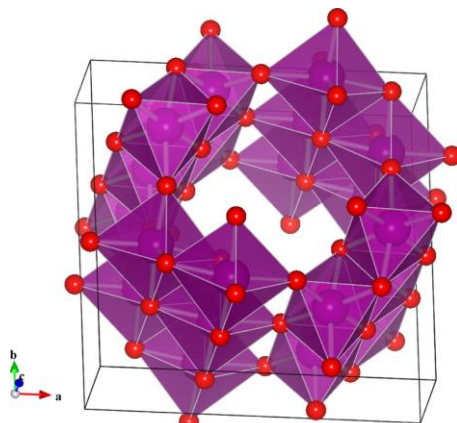
Figure 3.2: Crystal structure of α-MnO$_2$. Small (red) spheres are oxygen and large (purple) manganese lie inside the indicated approximate MnO6 octahedra. Image reproduced from ref. [126]

The α-MnO$_2$ NWs were synthesized by hydrothermal treating a mixture of 2mmol KMnO$_4$ (Acros Organics, 99+%) and 2mmol NH$_4$Cl (Strem Chemicals, 99.5%) dissolved in 100ml of deionized water, according to a procedure reported elsewhere[127]. A 20ml of this solution was sealed in a 23 ml autoclave with a Teflon stainless steel liner and the autoclave was heated at 150°C for 2 days. After cooling down to room temperature, the solid product was washed thoroughly with

deionized water and then dried at 100°C in air overnight. This results in producing high aspect ratio one-dimensional crystals, which are ~15-60 nm in diameter and up to several micron long.
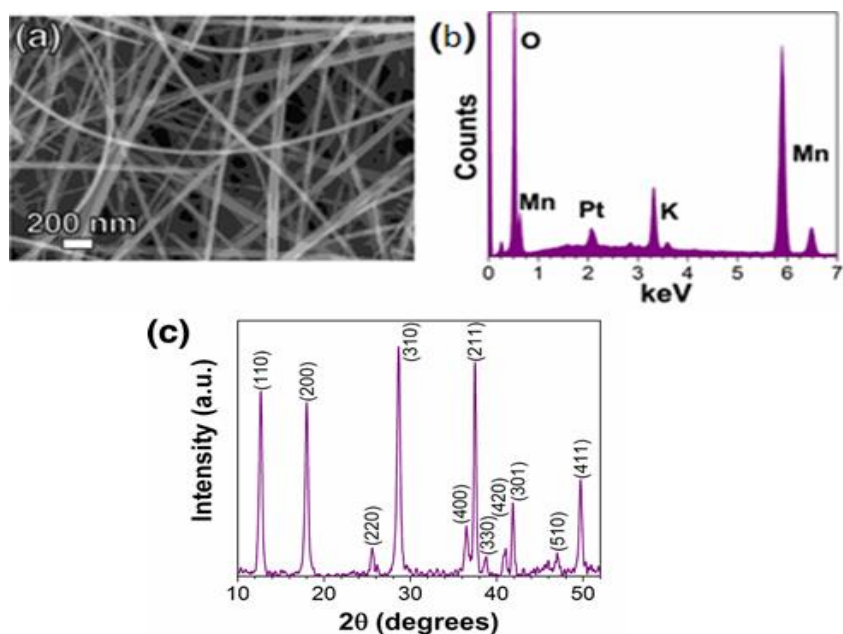
Figure 3.3: (a) SEM image (b) EDS spectra and (c) XRD for α-MnO$_2$ nanowires. Images reproduced from [128]. Experiments performed by Dr. Pomerantseva group, Drexel University.

The morphology of the as-synthesized material is similar to the results reported before[127] (Fig. 3.3 a[128]). Briefly, MO$_x$ units are formed when the chemicals of KMnO$_4$ and NH$_4$Cl are mixed to form layer-structured sheet MnO$_2$. Then under hydrothermal treatment, the mixture rolls up into nanowires, and K$^+$ ions stabilize the final product as α-phase MnO$_2$. The bulk-scale characteristics of these NWs as shown in EDX spectrum (Fig. 3.3 b) indicated that stabilizing potassium ions are present in the NW crystal structure, which corresponds to a stoichiometric composition of K$_{0.11}$MnO$_2$. The XRD pattern of the α-MnO$_2$ NWs, as shown in Fig. 3.3 c, is in good agreement with the standard data (JCPDS No. 44-0141) indicating formation of a pure tetragonal phase with I4/m

symmetry. The composition the NWs, as determined using EDX analysis, was used to estimate the theoretical capacity of the material and was found to be 261 mAh/g at a 1 C-rate.

In addition to pristine α-MnO$_2$ material, acid-leached samples have also been studied. In the acid-leached samples, the stabilizing potassium ions, which are within the α-MnO$_2$ material, are removed using acid treatment. This results in more space within the tunnels for lithium storage and also, increases the electrical conductivity of the electrode (as will be discussed in the next Chapter).

α-MnO$_2$ nanowires are deposited onto the device regions using DEP, as described earlier. Each nanowire is doubly clamped with platinum using the EBID technique[129] in order to avoid slippage, and also to reduce contact resistance. This chip is now placed on a stage inside the glove box, with the positive terminal being connected to the large pad on the left, using a gold-coated probe needle. Lithium wire acts as an anode and is connected to a second micromanipulator probe holder. An EC: DMC 1:1 electrolyte (Ethylene carbonate: Di methyl carbonate) with LiPF$_6$ dissolved in it is dropped on the nanowire arrays to complete the electrochemical circuit. To start the lithiation, a potential of 2.75V vs Li$^+$/Li is applied for the nanowire array and the state-of-charge (SOC) is decreased further by using lithiation potentials of 2.25V and 1.5V for the next steps. With the same setup, the nanowire will be de-lithiated when a higher voltage of 4V is applied. This completes one full electrochemical cycle. At each SOC, the properties of the electrode material, such as its size, electronic conductivity and Young's modulus are measured. This chapter presents evidence for electrochemical lithiation of the nanowires and also, presents

insights into the size changes in the nanowires. The conductivity and nanomechanical measurements of α-MnO$_2$ will be presented in the later chapters.

3.3) Results and Discussion:
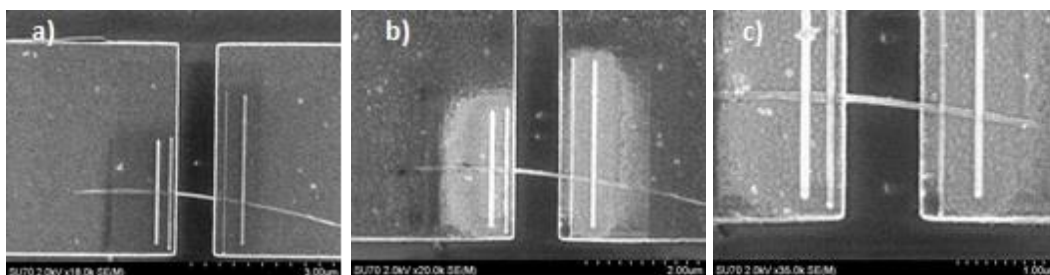
Figure 3.4: SEM images at different stages of lithiation a) 2.75V, b) 2.25V, and c) 1.5V.

The SEM images of an α-MnO$_2$ NW device taken at different stages of lithiation, are shown in Figure 3.4. It can be seen that this NW remains intact without mechanical fracture. In order to measure the size changes caused by lithiation, AFM imaging was performed on these nanowires. An example device is shown in Figure 3.5.
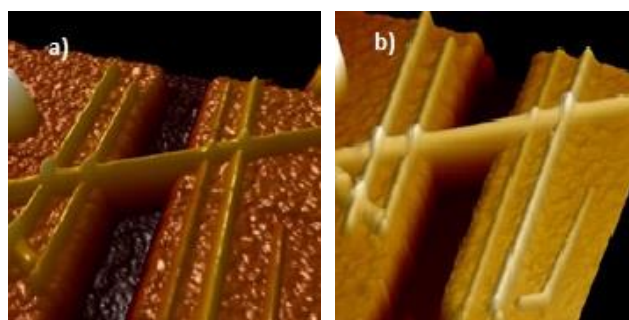
Figure 3.5: 3D AFM image of pristine α-MnO$_2$
a) Before lithiation, and b) After 1.5V lithiation

At every stage of lithiation, the diameter of several α-MnO$_2$ nanowires was measured using the height plot from an atomic force microscopy scan using Bruker Nanoscope analysis software. The

change in diameter (y-axis) at unlithiated and 1.5V state of charge is shown in the data presented

in Figure 3.6.
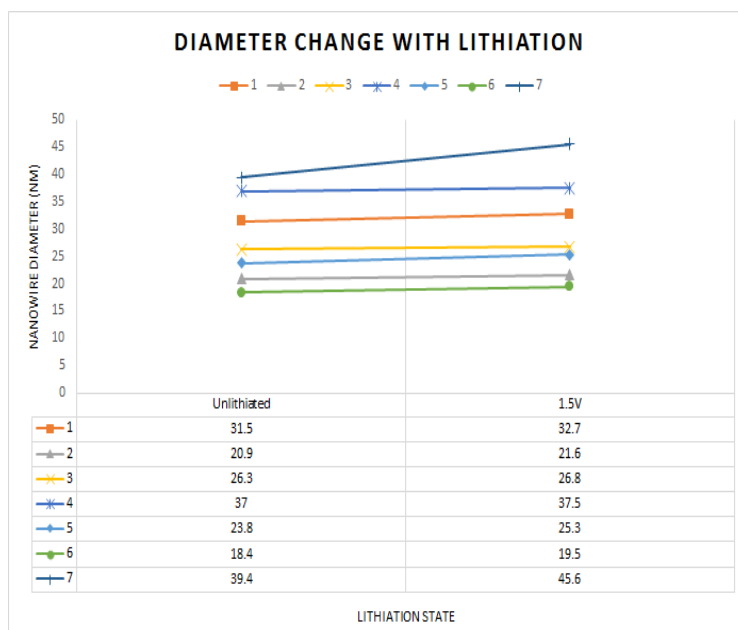
Figure 3.6: Diameter calculation for α-MnO$_2$ NWs

From the graphs, it can be seen that the size of the NW increases with lithiation. This is due to

the increase in tunnel size after the lithium ions are intercalated into the material. This conclusion

is supported by past simulations, which have shown an increase in the 'a' lattice parameter

(which corresponds to the NW diameter) due to lithiation[130]. On the other hand, past models

have predicted no change in the 'b' lattice parameter and this is expected to result in no changes

in the NW length, as is observed in our experimental results.

To confirm that the size changes are caused by electrochemical activity and not by any chemical

reaction of the electrolyte, an electrolyte dip test was performed on a chip sample for about 40

seconds, which is on the order of the lithiation times used in earlier experiments. SEM images of

two different NWs are shown in Figure 3.7. The measured diameter of the NWs, before and after

the electrolyte dip, did not show any difference. This confirms that size changes occurred due to

lithiation.
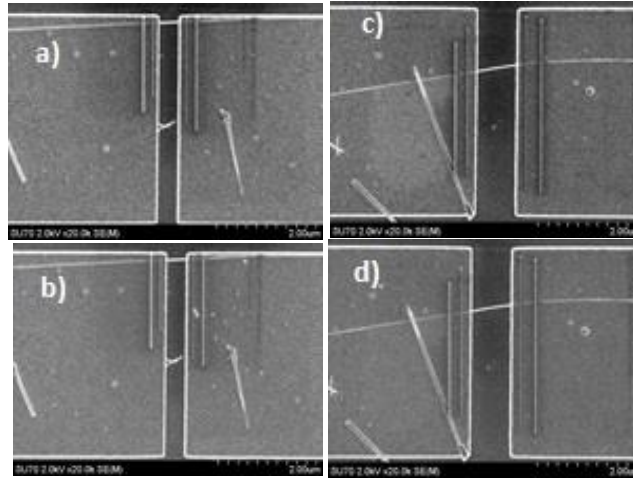
Figure 3.7: SEM images of Electrolyte dip test for
40 secs, no change in diameter from a – b, c – d
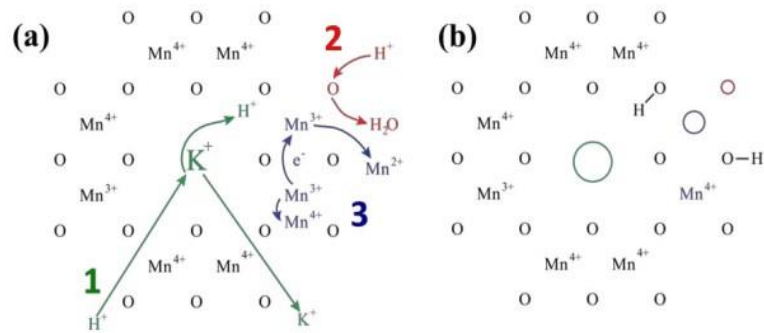
Figure 3.8: a) 1 – Extraction of potassium ions and possible exchange with protons; 2 – Formation of oxygen defects; 3 – Disproportionation of Mn^{3+} into Mn^{4+} remaining in solid material and Mn^{2+} dissolving in acidic solution. (b) Empty circles show formation of vacancies in potassium (green), manganese (blue) and oxygen (red) sites due to the acid-leaching of the material, image reproduced from ref. [131]

In addition to α-MnO_2 NWs, lithiation experiments have also been performed on acid-leached

nanowires, which were synthesized and provided by the Dr. Pomerantseva's lab at Drexel

University. Acid-leaching is a technique in which the material is acid treated to partially remove the potassium ions and then, replace them with protons. In this step, nitric acid is used and the acid reaction results in three types of vacancies, as shown in the Figure 3.8[131].

Figure 3.8 shows AFM images of the un-lithiated and lithiated acid-leached nanowires.
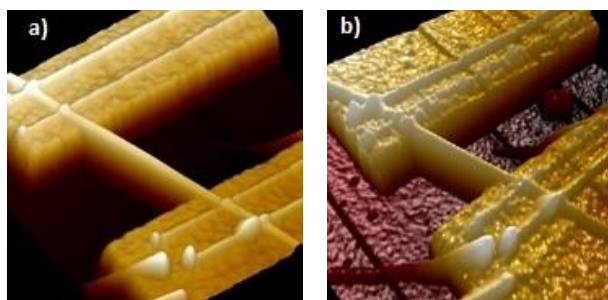
Figure 3.9: 3D AFM image of acid-leached α-MnO$_2$
a) Before lithiation, and b) After lithiation

Following figure 3.9 gives the AFM section plot of the diameter change in a) acid-leached and b) pristine α-MnO$_2$ nanowire before and after lithiation.
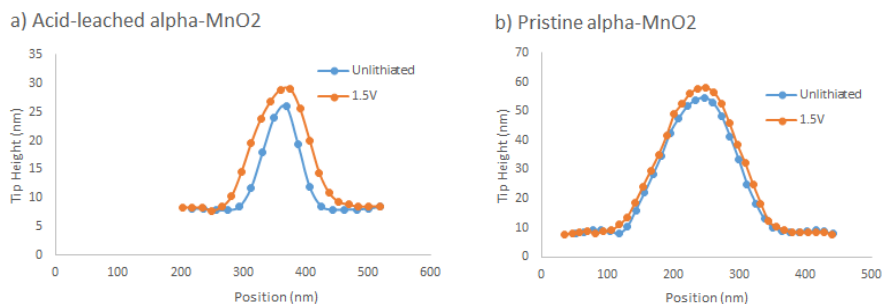
Figure 3.10: AFM section plot - Diameter change comparison

Chapter 4: Electrical Characterization

4.1) Rationale and Background:

As indicated in earlier parts of the text, nanomaterials are proposed for use in battery electrodes to improve energy and power density[132]. Electrodes based on nanomaterials help in reducing the mass of the inactive material. Another positive attribute is the short diffusion path offered, thereby increasing the rate capability of the cell[133]. Electronic and ionic conductivity of the electrode has a direct impact on the performance of the battery and its characterization is essential in both, the un-lithiated as well as the lithiated states of the material. A higher conductivity enables the movement of electrons and ions from/into the electrode material and results in higher charge/discharge at a given rate.

The crystal structure of a battery electrode has a direct impact on its electronic conductivity. For instance, the conductivity of representative battery cathodes, which are shown in Figure 4.1, is dependent on their crystal structures[134]. The crystal structure of these materials determines different diffusion pathways for the movement of ions and electrons. The first material type is in the form of layered compounds, having a 2D framework and have a chemical form $LiMO_2$ (M=Co, Ni, Mn etc.). Metal and Lithium cations occupy the octahedral sites of alternative layers as shown in figure 4.1 (a). They undergo severe structural changes when more than half of Li ions were removed during a discharge cycle. Studies are being conducted by mixing metals such as Ni, Mn, Co to form an oxide compound like $LiNi_yMn_yCo_{1-2y}O_2$ (NMC), which can reduce the drawbacks

associated with $LiCoO_2$ and $LiNiO_2$. The second type of cathode material has a 3D framework

spinel structure with metal cations occupying the octahedral position, but having 1/4 of them in

the Li layer. This allows for some lithium ions to occupy the vacant octahedral sites in the

transition metal layer, thereby offering high energy density. These are of the chemical form Li

$[M]_2O_4$ with M = Mn, $(Mn_{1-y/2}Li_{y/2})$ or $(Mn_{3/4}Ni_{1/4})$ and were found to undergo capacity fading due

to Jahn-Teller (JT) distortion associated with Mn^{3+} unstable ions. Doping with Cr, Fe and Ti was

also found to reduce this disorder. The third type of compound is the Olivine shape, which offers

1D framework for movement of Li ions. They are of the chemical form Li $[M]PO_4$ with M = Fe, Mn,

Ni, Co or (Fe_yMn_{1-y}) and have metal and Li cations in half of the octahedral locations and

phosphorus in one-eighth of tetrahedral sites. These compounds offer excellent properties such

as low cost and non-toxicity, but have a major disadvantage of lower cell potentials. Substituting

Fe with transition metal ions like Mn, Co, Ni was found to increase the voltage

substantially[57,134,135].
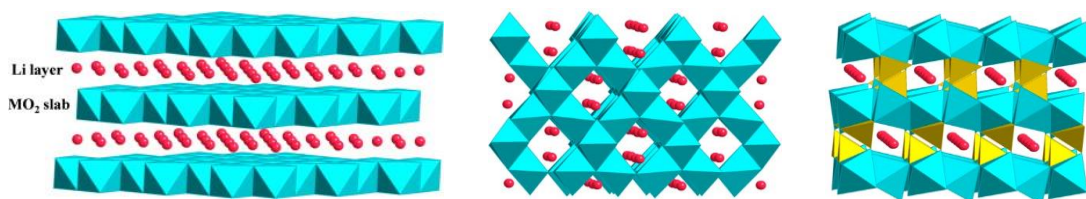
Figure 4.1: Crystal structure of a) Layered $LiMO_2$, b) Spinel LiM_2O_4 (Blue: M ions, Red: Li ions), and c) Olivine $LiFePO_4$ (Blue: Fe, Yellow: P ions, Red: Li ions), image reproduced from ref. [134]

Although conductivity of nanostructured electrodes is considerably higher than that of bulk

materials, conductive fillers or additives are still essential to improve their rate capability[136,137].

There are additional techniques that have been found to increase conductivity, such as doping with metal or non-metal ions[132,138] and developing new synthesis methods[139], and using new electrolyte compositions[140]. Because of the high surface area offered by nanomaterials, the rate of reactions with the electrolyte increases at the electrode surface resulting in high self-discharge and reduced cycle life. Electrolytic oxidation is one such phenomenon that happens at the cathode surface, which is non-reversible, and results in releasing electrons. These in turn react with the cathode material forming compounds that affect their electron transport performance[141]. Also, the structure of electrodes affects electron conduction[142]. In a recent study, it was found that 2D crystallized materials offer better characteristics owing to their scattering property[143].

To summarize, for any battery nanomaterial, controlling and measuring its conductivity will be crucial for efficiently implementing its functionality. There are several additional factors that can affect this value at the nanoscale as compared to their bulk counterparts. A few of these factors are listed below[144–148]:

- ❖ Presence of Crystallographic defects
- ❖ Impurity during NW growth
- ❖ Oxidation of the surface
- ❖ Increase in surface scattering
- ❖ Carrier Concentration
- ❖ Band gap
- ❖ Temperature

But, the techniques developed so far for battery diagnostics give an average estimation on the total properties, and are not correlated with the material performance at a single particle level. For a better understanding of these changes, new characterization methods are needed to evaluate the performance of single battery nanomaterials at different stages of lithiation. This chapter presents two-terminal electrical property measurements from single nanowire battery electrodes sourced from multiple material systems[149,150]. There are two types of measurements presented in this chapter: (1) electrical characterization of as-synthesized materials; this has been performed for multiple material systems such as pristine and acid-leached α-MnO$_2$, todorokite – MnO$_2$, bio-derived graphitic carbon particles and n-doped CNTs, (2) electrical characterization measurements as a function of lithiation; this has been performed on pristine and acid-leached α-MnO$_2$. A comparison of electronic and ionic conductivity of α-MnO$_2$ and todorokite – MnO$_2$ is also presented at the end of the chapter.

4.2) Experimental Procedure:

Two-probe and four-probe methods are two popular techniques that have been used earlier to perform conductivity measurements on single nanowires[151–154]. Two-probe method does not have a capability to resolve the contact resistance between the NW and the metal contact. This method needs additional experimental steps to take into account the contact resistance of the NW with the metal surface. On the other hand, the four-point method eliminates the contact resistance by adding two more probes to the circuit. In a current controlled circuit, the voltage is measured between the same probes in a two-point method, whereas the remaining two probes

are used for measuring the voltage in a four-point method. A setup for simultaneous two and four point measurements is shown in the Figure 4.2 [155]. In our case, we use a Keithley 2636B source-meter to supply the voltage and measure the current in a two-terminal configuration, thereby generating an I-V (Current- Voltage) plot.
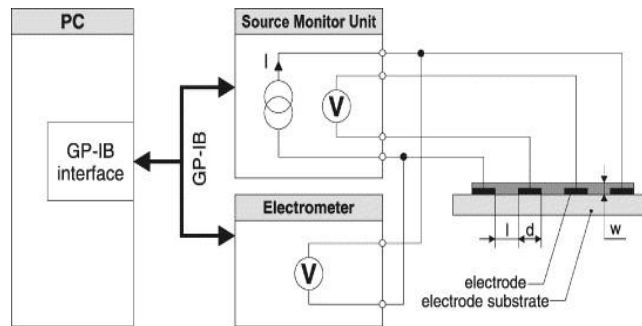
Figure 4.2: Simultaneous set up for two and four-point measurement.
Image reproduced from ref. [155]
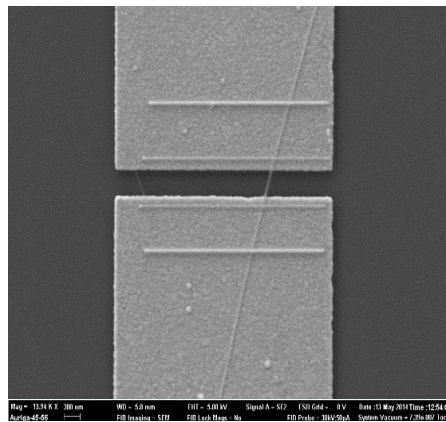
Figure 4.3: SEM image of α-MnO$_2$ NW, double clamped with Pt EBID

A typical NW device is shown in Figure 4.3, with the NW being deposited at a capacitively coupled location using DEP. Double top side platinum metallization clamps are done on both sides of the nanowire, made using Electron beam induced deposition (EBID). The function of these clamps is to reduce the contact resistance between the nanowire and the gold surface[109].

Each pad on the right side of the chip is wired to an individual device, while the one on the left is common to all devices on that chip. To perform the I-V measurements, one probe (positive) is brought in contact with the right side, individual pad and the second probe (negative) is brought in contact with the left-side common pad (Figure 4.4). The goal of the IV measurements is to characterize the electrical properties of one suspended nanowire at any given location. The resulting data is used to either quantify the electronic conductivity of the material or to gain insights into the changes in electron transport performance as a function of lithiation.
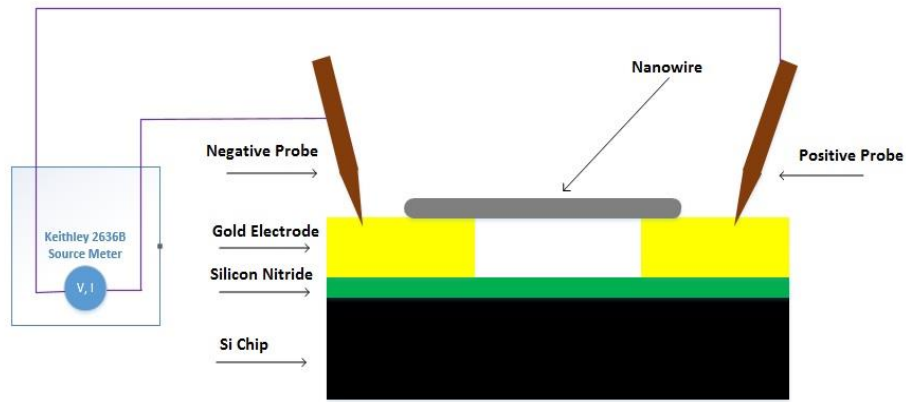
Figure 4.4: I-V Setup using Keithley 2636B source meter

In measurements involving the α-MNO$_2$ material system, the contact resistance term is quantified using a technique where the two-probe measurements are performed on two separate device locations, each with a different probe separation[156,157]. In such a two-probe setup, the total device resistance is given by this formula[109,158]:

$$R = \frac{V}{I} = R_c + \frac{l}{\sigma_{NW}\,A} \qquad (10)$$

Where

V = Voltage in the circuit

I = Current in the circuit

R_c = Total contact resistance in the circuit = $2 * r_c$

r_c = Contact resistance between NW and gold surface on each end

σ_c = Conductivity of the NW

l = Suspended length of the NW

A = Cross sectional area of the NW

The above equation is valid only if the nanoelectrode is perfectly cylindrical in shape i.e., in the form of a nanowire (as is the case with most materials in this thesis). However, if the particle has a cross-sectional area which changes along the length (for example, a spherical particle), then the total resistance can be calculated as a function of length L given by the following equation[144]:

$$R = R_c + \int_{-L/2}^{L/2} \frac{\rho}{A(L)} \, dL \qquad (11)$$

4.3) Results and Discussion:

The results from I-V measurements, which were performed on two α-MnO$_2$ NW samples, are shown in Figure 4.5.
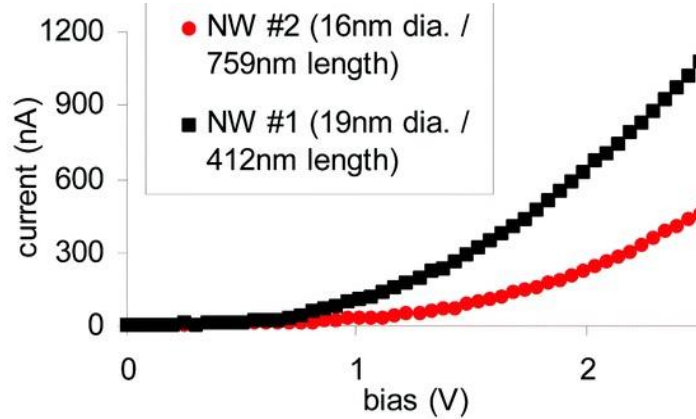
Figure 4.5: I-V plots of two α-MnO$_2$ NWs, image reproduced from ref. [109]

The first nanowire was 412nm long and measured 19nm in diameter. The second nanowire measured 759nm long and 16nm in diameter. These measurements were calculated using AFM data and from NIH ImageJ software[159]. The inverse slope of the graph for each NW will give its terminal resistance (R). Using the two terminal resistance formula (equation 10) and solving for the two unknowns using the two resulting equations, the material conductivity and NW-metal contact resistance is calculated for this system. Using this method, the contact resistance between NW and gold surface (r_c) is calculated to be 145.7 kΩ and the conductivity of α-MnO$_2$ NW (σ_{NW}) to be 182.2 S/m.

The changes in electronic conductivity of the NWs have also been studied as a function of lithiation. In this experiment, the NWs were lithiated (using the set-up shown previously in Figure 3.1). The lithiation potentials were fixed at 2.75V, 2.25V and 1.5V, and the NW resistance is measured at the end of each stage (Fig 4.6). When lithiated, lithium ions from the anode intercalate into the single NW working cathode and increase the impedance in the NW. This

reduces the conductivity because of an increase in lithium capacity at the end of each stage of lithiation. It was observed that the conductivity of the NW drops by half when lithiated to 1.5V from an unlithiated state. The conductivity doesn't change much from the unlithiated to the 2.75V state, where the lithium insertion is just starting to take place. On the other hand, much of the lithium is inserted during 2.25V stage and there is minimal change that happens after 2.25V. At 1.5V, maximum insertion of lithium occurs. These conductivity changes were found to be consistent with previous results[94,103].
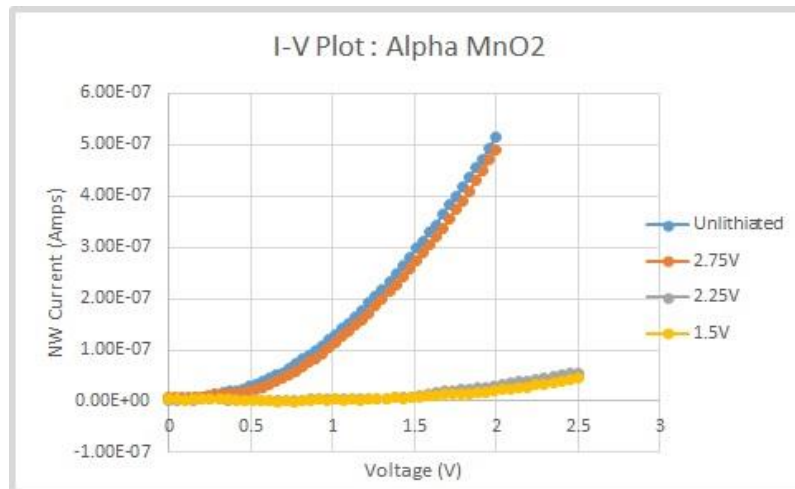
Figure 4.6: I-V curves of NW at different stages of lithiation

Because an electrolyte is also involved in the lithiation process, it is important to test that the conductivity changes are caused by pure lithiation and not due to the electrolyte. In every lithiation experiment, the NW was lithiated for about 30 secs in each stage. So a dip test was performed in pure electrolyte for about 40 secs to measure the effect of a pure chemical dip in the electrolyte. The conductivity and diameter were found to remain almost the same both, before and after this dip test. Figure 4.7 gives the I-V data for one NW on the chip before and

after electrolyte dip. These tests prove that the changes in conductivity, which were observed in

Figure 4.6, are caused by electrochemical lithiation.
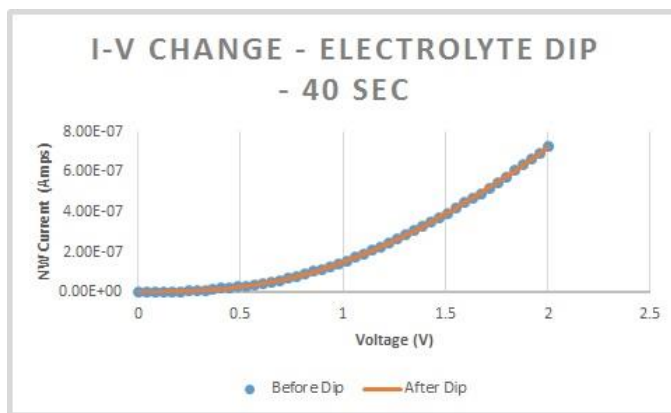
Figure 4.7: I-V before and after electrolyte dip test for 40 sec

In a similar fashion, electronic conductivity measurements were also performed on the acid-leached α-MnO$_2$ material system as a function of lithiation. Figure 4.8 gives the I-V plots for acid-leached α-MnO$_2$ NWs.
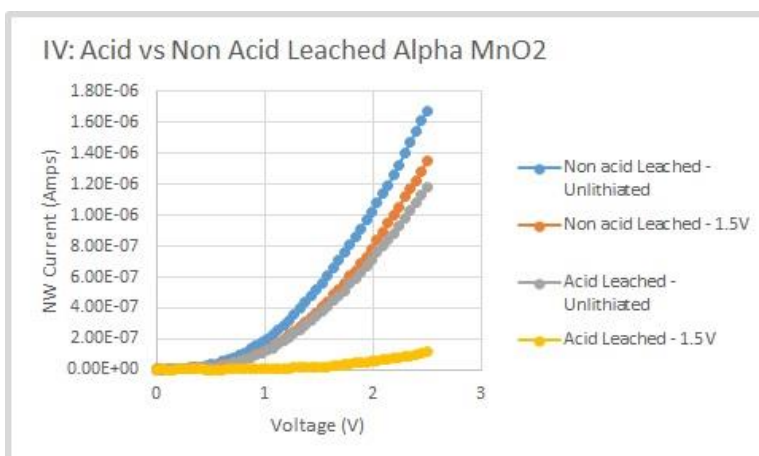
Figure 4.8: I-V for acid and nonacid-leached α-MnO$_2$ NW

From the graph, it can be understood that conductivity of the acid-leached NW is reduced by a factor of 12. This is higher than that observed with the nonacid-leached material. This behavior

is explained by a higher lithium intercalation in the acid-leached NW, which provides additional pathways for ionic and electronic intercalation owing to the differences in its crystal structure. This hypothesis needs further verification in terms of storage capacity comparisons for these two materials. These measurements, while being outside the scope of this thesis, are currently being performed by our collaborators at Drexel University.

Another material system, which was tested for its electronic transport properties, is bio-derived graphitic carbon particles (material sourced from Dr. Gupta's Lab at VCU). The Li-ion batteries of today use carbon or graphitic anodes. Due to the rapid growth in the use of these batteries, there is an increase in efforts to have battery electrode materials made from "green" sources[94]. Lignin bio-mass is one such source, which is a byproduct from the paper and pulp industry. Only 2% of this material is reused for heating, while the rest is burned to generate energy. Graphite, a naturally occurring material, helps in improving the electronic conductivity and energy density of batteries. It has gained popularity due to its ability to be synthesized from byproducts of naturally occurring products such as lignin[160], flake, cellulose, etc. There are previously reported techniques that produced graphite from bio-mass using a catalyst at high temperatures. The particles used in this project have been synthesized at Dr. Gupta's Lab using a combination of hydrothermal and high-temperature processing steps involving suitable catalysts[161]. Synthesis parameters were found to have an impact on the extent of graphitization within the carbon particles, and using this principle, three bio-derived Li-ion battery electrodes GC1100, NiGC1100 and NiGC1000 were developed from commercially available lignin. Here, GC stands for graphitic

carbon, Ni was used as a catalyst in NiGC formation and 1000, 1100 are the temperatures in the

process. Figure 4.9 gives the SEM images for these three particles after DEP assembly.
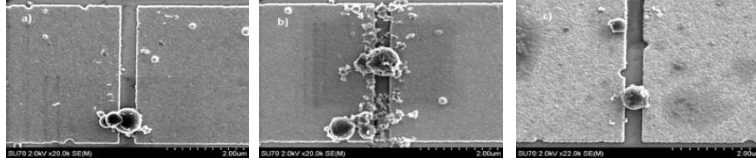
Figure 4.9: SEM images of a) GC1100, b) NiGC1000, and
c) NiGC1100 nanoparticles with radius between 300-500nm

Since the particles are spherical and not cylindrical in shape, the resistance equation is modified

as:

$$R_p = \frac{\rho}{2\pi R}\left\{ln\left(\frac{R+L_1}{R-L_1}\right) + ln\left(\frac{R+L_2}{R-L_2}\right)\right\} \qquad (12)$$

where R_p, ρ and R denote the particle resistance, resistivity and radius, respectively. L_1 and L_2

indicate the radial length of the inter-electrode regions of the left and right-halves of the particle,

respectively.

From experimental values of particle geometry, resistance using the equation 12, resistivity from

the slope of I-V plot (Figure 4.10), conductivity is extracted for the three materials. These values

are listed in Table 1.
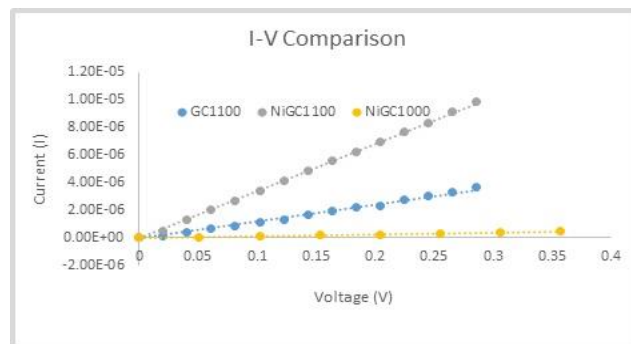
Figure 4.10: I-V Comparison of GC1100, NiGC1100 and NiGC1000

56

Table 1. Conductivity Comparison

Particle type	Radius (R, nm)	L_1 (nm)	L_2 (nm)	Resistance (R_p, kohm)	Resistivity (ohm-m)	Conductivity ($S \cdot m^{-1}$)
GC1100	357	149	177	64.18	0.072	13.83
NiGC1100	315.5	86	156	14.34	0.017	57.80
NiGC1000	451	252	272	602.75	0.643	1.55

It can be seen that NiGC1100 exhibits higher conductivity among the three particle types. This increase in electronic conductivity is attributed to an increase in graphitic content, which was confirmed by X-ray diffraction data obtained by Dr. Gupta's Lab[162,163]. This method to increase electronic conductivity in lignin-based carbon is critical to their potential application as environmentally-friendly Li-ion battery anodes.

Additionally, the electronic conductivity of both α-MnO_2 and todorokite – MnO_2 are measured in a similar fashion to bring the relationship between electrochemical performance, electronic and ionic conductivities of these tunnel structured manganese oxides in order to compare their rate performance[128]. This study was needed to determine the factors contributing to the rate performance, and thereby fine tune the properties and structure of the material in order to achieve higher current and power density. The ionic conductivity of the electrode material is often represented by the Li^+ diffusion coefficient ($D_{Li}+$) and the reported values in literature are used as a reference for comparison. Both these materials have similar square tunnel configurations and are built by edge and corner sharing MnO_6 octahedra building blocks. Both

these materials are stabilized by the presence of cations within its tunnels. α-MnO_2 has K^+ and todorokite has Mg^{2+} ions, but they only partially occupy the space inside these structural tunnels, thereby leaving enough room for the Li^+ ions to intercalate within the material.

The todorokite-MnO_2 has the largest tunnel structure among all polymorphs of MnO_2 and forms a 3 × 3 tunnel structure[164,165], whereas α-MnO_2 forms a 2 × 2 tunnel structure having a lattice side length of 4.6 angstroms[128]. Both these polymorphs are synthesized using hydrothermal method but with different startup solutions. The synthesis procedure for α-MnO_2 was discussed in detail in Chapter 3, section 2, whereas todorokite nanowires are synthesized using a previously published technique[166]. Briefly, 50 ml solution of 1M NaOH and 50 ml solution of 2M H_2O_2 was added to a 50 ml solution of 0.3M $Mn(NO_3)_2$. The solution is left to react for 30 min, after which the precipitate product Na-birnessite was filtered and washed with deionized water. This filtered powder when placed in 1M $MgCl_2$ for 3 days at a constant stirring rate performs an ion exchange and replaces Na^+ ions with Mg^{2+} ions. This final Mg-buserite product is also filtered and washed with deionized water, dried at 100 °C for 12 hours under vacuum. Todorokite nanowires are then obtained by dispersing 100 mg of dried Mg-buserite in 17 ml of 1M $MgCl_2$ solution. This mixture was hydrothermally treated for 96h at 220°C, and products were filtered, washed and dried at 100°C for 12h under vacuum.

Using Equation 10, the electronic conductivity and contact resistance for α-MnO_2 are calculated (average of 4 samples) to be 2.259 S/cm and 395.7 kΩ respectively. Similarly, for todorokite, we obtained the electronic conductivity and contact resistance to be 4.9×10^{-2} S/cm and 21.7 MΩ,

respectively. Thus, we find that the electronic conductivity of α-MnO$_2$ is higher than that of todorokite phase by a factor of ~46. The representative I-V plots and 2-terminal resistance plots are shown in Figure 4.11[128]. Past works in literature have reported that the lithium diffusion coefficient (D$_{Li}$+) values of α-MnO$_2$ range from 1×10^{-10} cm^2/s for the fully charged state to 2×10^{-11} cm^2/s for the fully discharged state[167]. For todorokite, the values reported ranged between 1×10^{-7} cm^2/s for the fully charged state to 2×10^{-10} cm^2/s for the fully discharged state.
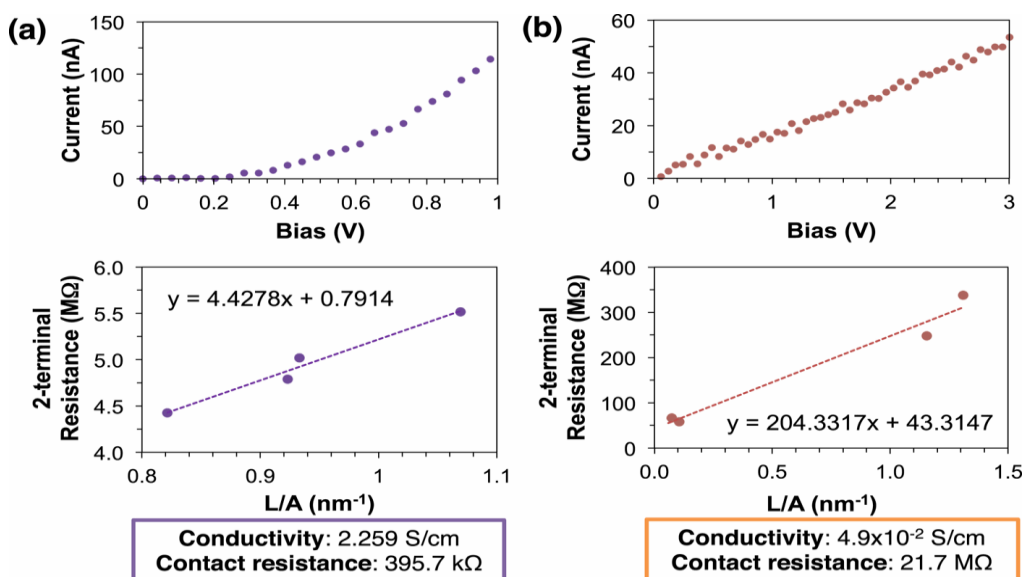
Figure 4.11: (a) Two-terminal I-V measurement data (top) from a representative α-MnO$_2$ nanowire device. The bottom panel shows a plot of the two-terminal resistance as a function of the nanowire length-to-area (cross section) ratio for four different devices. (b) The I-V plots of a todorokite nanowire device (top) and the two-terminal resistance as a function of nanowire length-to-area ratio for four nanowire devices. Image reproduced from ref. [128].

The rate performance of both material systems has been determined by conducting electrochemical cycling at different current rates and then compared[128]. These bulk-scale measurements, which were performed at the Dr. Pomerantseva Lab in Drexel University, showed

that todorokite had better electrochemical performance at higher current rates, and ionic conductivity played a significant role than electronic conductivity (Fig. 4.12).
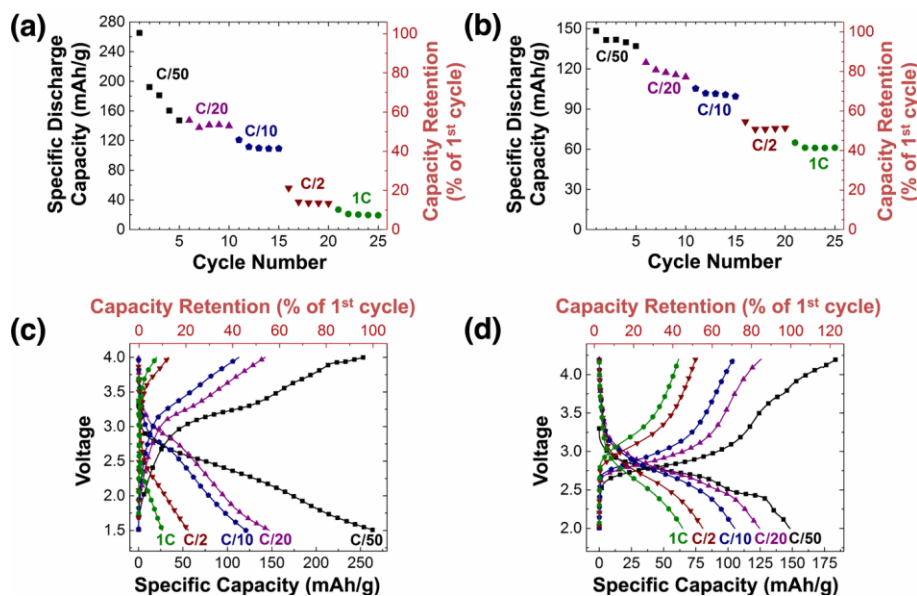
Figure 4.12: Electrochemical performance of α-MnO2 and todorokite nanowires in a Li-ion battery at current rates of C/50, C/20, C/10, C/2, and 1C. (a) and (b) show the capacity of α-MnO2 and todorokite nanowires, respectively, versus the cycle number as a function of applied current density. The galvanostatic discharge/charge curves are shown for the first cycle at each current rate for α-MnO2 (c) and todorokite (d). Image reproduced from ref. [128].

Hence, it is evident that lithium diffusion coefficient is the limiting factor in determining performance of tunnel structured materials, and by tuning the tunnel size and stabilizing cation, the electrochemical performance of intercalation based energy storage materials can be improved. The measurement of electrical performance of multiple battery electrode material systems, the data for which is not available in the current literature, is an important contribution of this thesis.

Chapter 5: Nanomechanical Characterization

5.1) Rationale and Background:

As newer materials with varying structures and shapes are being studied for use in batteries, it will be crucial to perform mechanical testing on these materials in order to understand their failure modes and to overcome them for building better batteries. Fracture and disintegration of the electrode material is one such critical failure caused by buildup of stress, either by volume expansion or by phase transition, in a typical electrochemical cycle. Fracture causes electrode break-up resulting in electrode dissolution in the electrolyte or reduction in electronic conductivity, and thereby, leads to a reduction in the capacity of the system. The insertion and removal of ions during charging/discharging cycles result in high volume changes in the material, thereby restricting the use of some high energy capacity materials such as Si[18,71,75,168], sulphur[169,170], Sn, Al, Ge and Bi[171–173] in present batteries. Also, it was found that stress will be high when both phase transition and the intercalation mechanism act in a coupled fashion inside the material system.

There were previous studies on testing the properties of a material at the nanoscale using different principle techniques such as mechanical resonance[174], three-point bending method[175,176], and nanoindentation method[177,178]. For experiments involving indentation or mechanical pushing of the material using an AFM, different models have been established and the model is chosen based on the shape and structure of the materials[179]. Some models actually

studied the effect of stress and strain inside the electrode material during intercalation/deintercalation mechanisms, but these results are based on assumptions of a constant Young's Modulus value[180]. However, this assumption is incorrect and electrode materials have different elastic moduli during lithiation. This is consistent with some recently reported studies, which have found that the Young's modulus is continuously changing at every state of charge (SOC)[181,182]. This is caused by re-ordering of chemical bonds during the relaxation and reconstruction processes that accommodate elastic strain. At small lengths, the mechanical properties of the surface layer are also found to dominate the elastic response of the material[183]. Depending on the type of stress acting on the material, the electrode materials show either elastic stiffening or softening[184].

AFM has been used quite extensively in determining the mechanical properties of materials[185,186] and it works on the principle of scanning the surface using an ultra-sharp probe (tip), which is attached to a cantilever. The cantilever is tuned near its resonance frequency and its amplitude of vibrations is detected using a photo detector. This data is analyzed to construct an image of the structure with a resolution reaching the sub atomic scale features. Young's modulus of a material gives an understanding of the elastic properties of a material, while other properties such as surface tension, adhesion force[187] and conductivity can also be obtained using an AFM. The most commonly used method for mechanical testing of nanomaterials is contact mode AFM. In this mode, a known force is exerted on the material by pushing on it using a calibrated tip. This results in a deformation or a change in shape of the material. This deformation is measured using the movement of the stage with respect to the tip. From an analysis of this data, a force versus

deflection plot of the nanostructure is obtained. A slope of this plot gives the Young's modulus of the material. Figure 5.1 shows this AFM three point bending technique for YM measurement in nanowires[177].
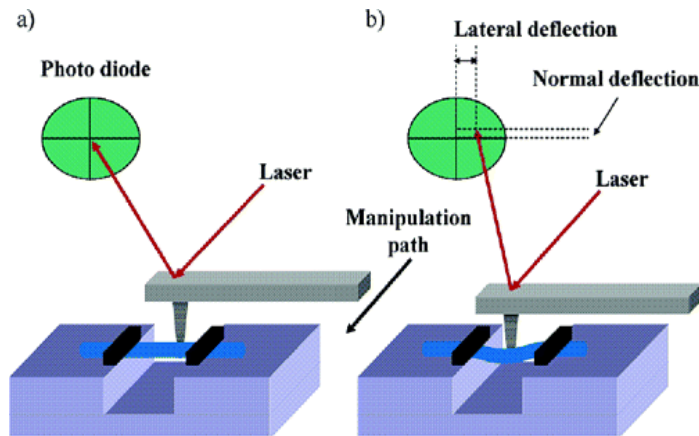
Figure 5.1: Experimental setup for three point bending a) Before Manipulation, and b) During Manipulation. Image reproduced from ref. [177]

5.2) Experiments:

A chip with the nanowire beam is placed under a Veeco Icon AFM to perform force spectroscopy measurements. Figure 5.2 shows an AFM image of a doubly clamped α-MnO$_2$ NW, which is suspended between the electrode pads[109].

The three-point bending method was then used to perform force spectroscopy on this sample. In this technique, the nanostructure is suspended in air as a bridge and the nanowire is anchored at the edge of the electrodes on both sides. The AFM tip is used to push on the NW at its mid-

lengths. The clamps on both sides help in reducing slippage of the nanostructure during this bending test.
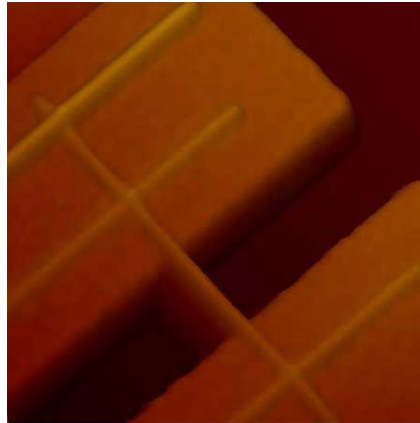
Figure 5.2: AFM image of α-MnO$_2$ NW

First step in the experimental procedure is to calculate the stiffness of the tip (k_{tip}). The tip is tuned to the resonance frequency and based on its quality factor / dimensions, its stiffness is estimated using Sader's method[188]. This tip is now calibrated by making contact with a hard surface on the chip (gold pad region) and the cantilever deflection (z_{cant}) versus the stage movement (z_{peizo}), which is controlled by a piezo motor, is measured. When calibrated, the slope of the cantilever deflection versus stage movement plot will be unity (as shown in Figure 5.3). In the plot, the blue line is termed as the "approach curve" (where the stage is moving up towards the tip) and the red line is termed as the "retract curve" (where the stage is moving down away from the tip).
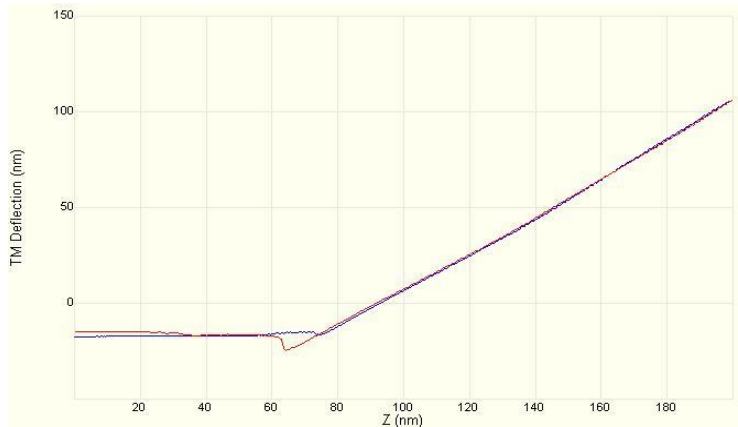
Figure 5.3: AFM plot of tip indentation on the gold electrode surface

Now, the AFM tip is moved to the mid portion of the nanowire and a force is exerted on it. As the tip is brought closer to the substrate, there are Vander walls forces acting on the tip, which makes it attract to the NW surface. This is also called the adhesion force and can be seen in Figure 5.4 at piezo distance (z_{peizo}) of 59.4 nm on the X-axis.
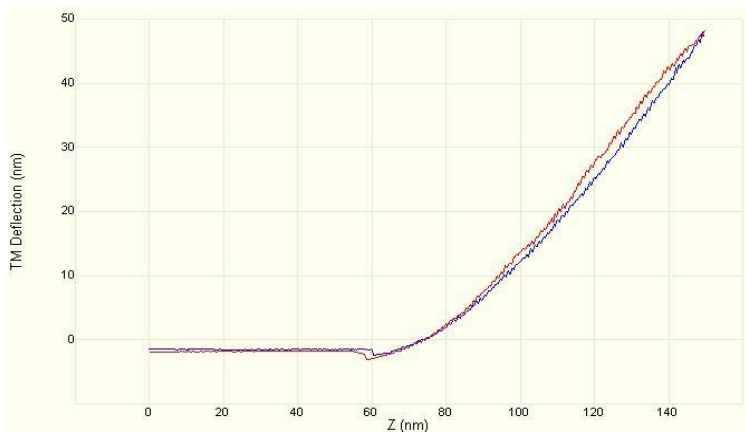
Figure 5.4: AFM plot of tip indentation on an α-MnO$_2$ NW

65

The red and blue lines corresponding to the position of -1.57 nm on Y-axis will be a reference line and at this line, the force on the cantilever (F_{cant}) and the force on the NW (F_{NW}) is zero. This is because, the cantilever deflection is zero along this horizontal segment.

$$F_{cant} = F_{NW} = 0 \qquad (13)$$

The movement of the stage from this reference line to the right will result in the deformation of the nanowire and the force acting on the NW can be calculated using these formula:

$$F_{NW} = F_{tip} = k_{tip} * Z_{NW} \qquad (14)$$

$$\delta_{cant} = Z_{cant} - Z_{cant(Reference\ line)}$$

where

F_{tip} = Force exerted by the tip, K_{tip} = Stiffness of the tip

Z_{cant} = Deflection of the cantilever,

$Z_{cant(Reference\ Line)}$ = Deflection of the cantilever at the reference line (-1.57 nm on Y-axis)

The deflection of the NW (Z_{NW}) can be calculated as:

$$Z_{NW} = \delta_{peizo} - \delta_{cant} \qquad (15)$$

The slope of the plot of F_{NW} vs Z_{NW} will give the stiffness of the nanowire (k_{NW}). Finally, the

Young's modulus of the material can be calculated using the formula[18]:

$$E = \frac{L^3 * k_{NW}}{192 * I} \qquad (16)$$

where

L = Suspended length between the electrodes in the gap region

I = Moment of Inertia of the NW

$= (\pi*r^4)/4$

r = Radius of the NW, obtained accurately using AFM section plot

In a similar fashion, the ultimate strength of the material can also be measured using an AFM by extending the tip indentation on the NW to the point of maximum force that can cause fracture. The original AFM loading and unloading data on one NW sample is shown in Figure 5.5 (a) and the extracted data in Figure 5.5 (b). From the Figure 5.5 (b), it can be seen that this 34 nm diameter NW undergoes fracture at a maximum force of 602.2 nN and at a deflection of 52.7 nm. Using these values, the ultimate strength of the material can be computed using equation 17[189,190] and was found to be 5.8531 GPa for this NW:

$$\sigma_{ult} = \frac{F_{cr}L_{NW}}{2\pi R_{NW}^3}g(\alpha) \qquad (17)$$

Where

$$g(\alpha) = \frac{4}{\sqrt{\alpha}} \tanh\left(\frac{\sqrt{\alpha}}{4}\right) + \sqrt{\left(\frac{2 + \cosh\left(\frac{\sqrt{\alpha}}{2}\right) - \frac{6\sinh\left(\frac{\sqrt{\alpha}}{2}\right)}{\sqrt{\alpha}}}{a\left(\cosh\left(\frac{\sqrt{\alpha}}{4}\right)\right)^2}\right)} \qquad (18)$$
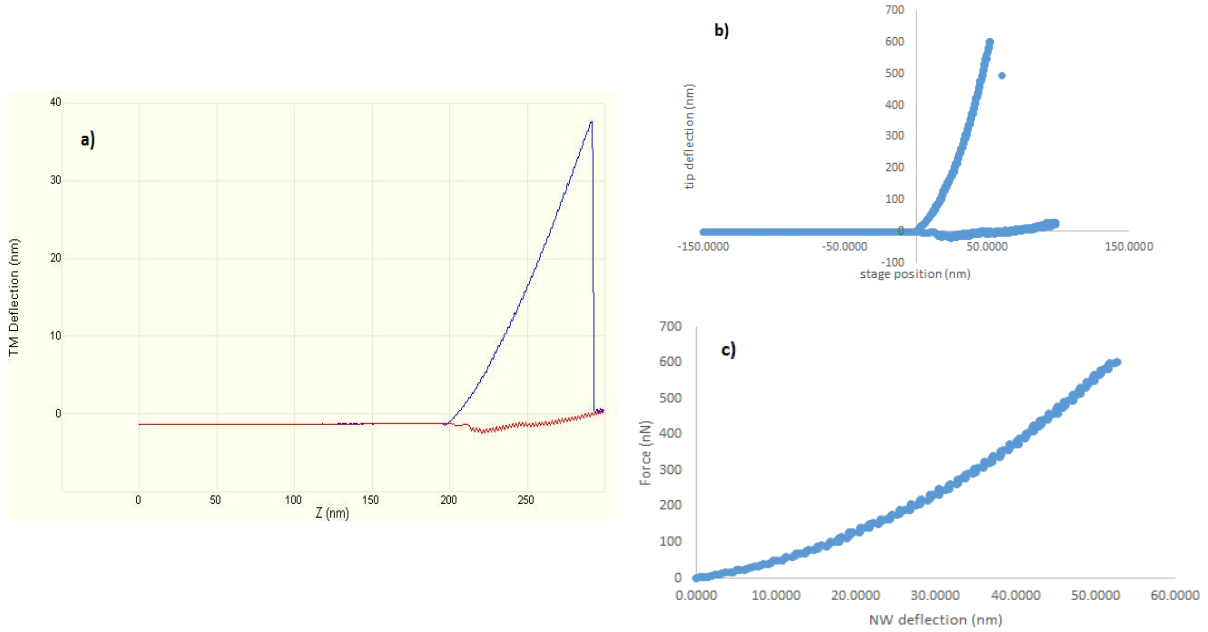
Figure 5.5: a) Original loading-unloading curve, b) Extracted AFM loading-unloading curve showing fracture, and c) Extracted force vs deflection plot on an α-MnO$_2$ NW – Nonlinearity

At deformations larger than the thickness of the nanowire, the F_{NW} vs Z_{NW} has a nonlinear behavior as shown in Fig 5.5 (c). This indicates that the material is undergoing both bending and tension loading. For these large deformations, the above mentioned approach using linear elastic beam bending theory would be insufficient. To account for tension and bending, an analytical model presented by Heidelberg et al. for Si nanowires may be used, and is given by this equation[177,186]:

$$F_{center} = \frac{192\,E\,I}{L^3}\,f(\alpha)Z_{NW} \qquad (19)$$

Where

$$f(\alpha) = \frac{\alpha}{48 - \dfrac{192\,\tanh(\sqrt{\frac{\alpha}{4}})}{\sqrt{\alpha}}} \qquad (20)$$

α represents the maximum deflection on the NW by the following equation, $\varepsilon = (2{*}Z_{NW}/R)^2$

$$\alpha = \frac{6\epsilon(140 + \epsilon)}{350 + 3\epsilon} \qquad (21)$$

In our experiments, as discussed earlier, the suspended NW length is obtained from the SEM image using ImageJ software and the NW radius from tapping-mode AFM scans of the NW. If a nonlinear behavior was found to be the case for any NW, the observed experimental data was curve-fitted to this analytical model using Matlab and the NW Young's modulus was estimated. Figure 5.6 (a) gives the curve-fit for the extracted data of Figure 5.5, and it can be seen that the fit accurately describes the force-deflection behavior and a YM of 74 GPa was extracted.

Moreover, when the curve fit is extended up to the point of maximum deflection, as seen in Figure 5.6(b), the predicted fit deviates from the extracted data starting from 35 nm (the diameter of the NW is 34 nm). At the point of maximum deflection (~ 52 nm), the NW deviates about 5-6 nm, before it eventually breaks down. This confirms a plastic deformation behavior, where the nanowire is permanently deformed, and it will not return to its original state.
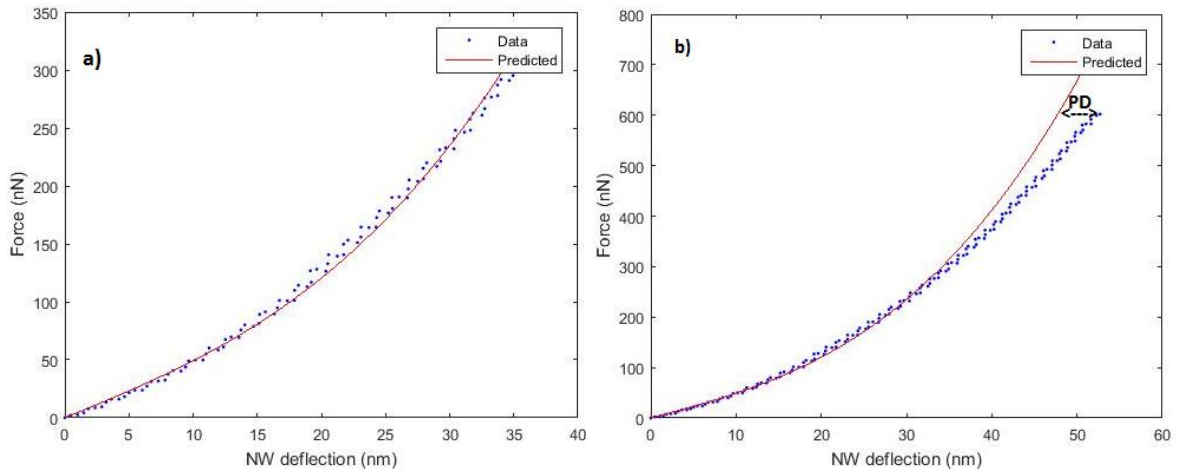
Figure 5.6: a) YM of 73.9 GPa was extracted from Matlab curve and b) Matlab Curve fit extended up to the fracture point, undergoes plastic deformation around 5-6 nm.

5.3) Results and Discussion:

Nanomechanical measurements of pristine and fully lithiated α-MnO$_2$ nanowires were studied using the AFM[187]. To test the impact of the state-of-charge (SOC) on the Young's modulus of a material, contact mode AFM was used to perform indentation at the end of each lithiation step, and the YM was calculated from these force-displacement plots. When lithiated, Li ions intercalate into the material, causing structural changes. These lithiation induced changes are discussed in detail in Chapter 6.

Using models presented in equations 17 and 19, the Young's modulus and ultimate strength for unlithiated α-MnO$_2$ are calculated. For the three NW samples that were measured in these experiments, the average value for the YM was found to be 46.5 GPa (with 95% confidence limits of $\pm$4.5 GPa). The reported Young's modulus values for bulk-scale lithium manganese oxide

spinels lie within the range of 10 GPa to 240 GPa[191,192] and has shown no clear dependence on particle size[193]. Figures 5.7-5.9 give the detailed information for three unlithiated α-MnO$_2$ nanowire samples, followed by a summary of measured values of Young's modulus, ultimate strength and theoretical-to-experimental strength ratio for these nanowires.
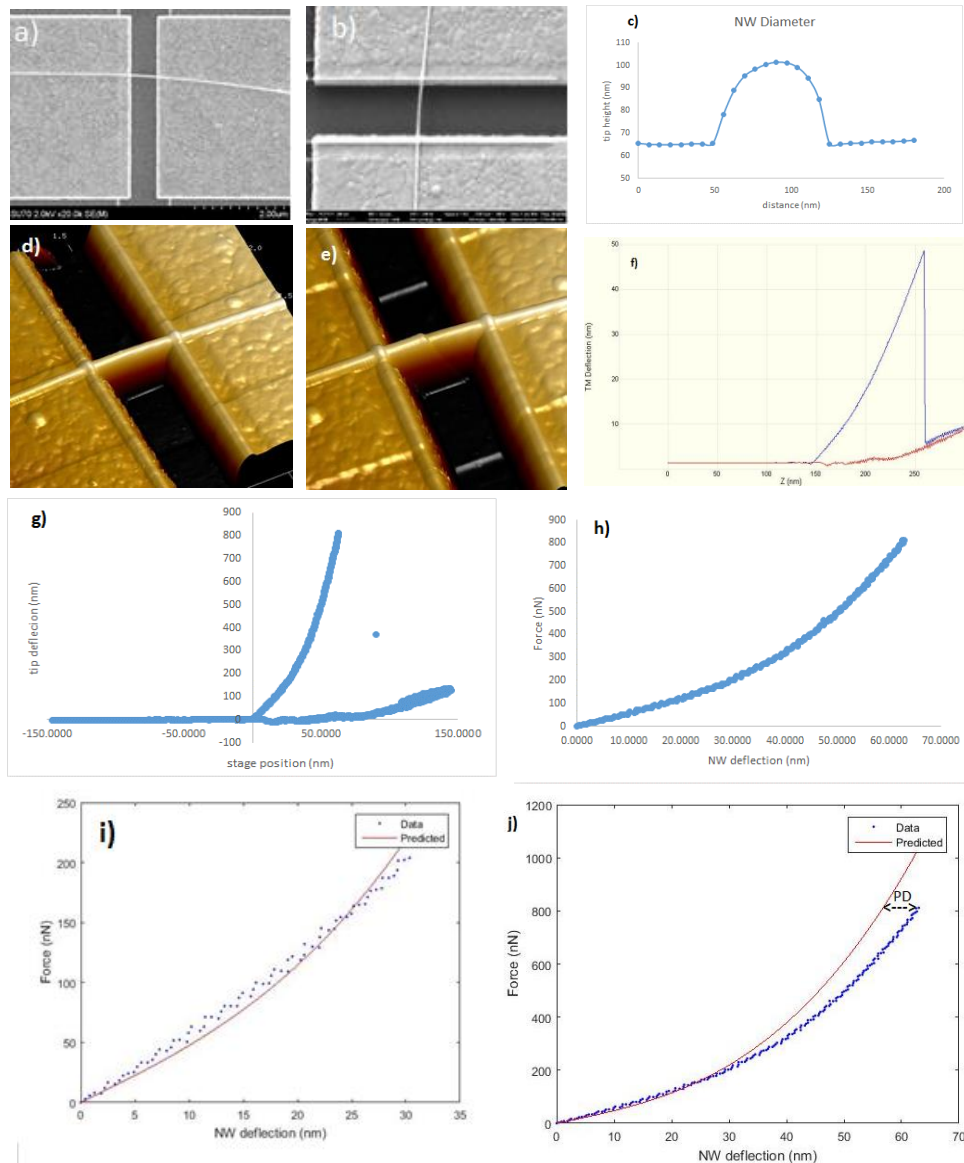
Figure 5.7: DEP Sample 1 a) SEM micrograph of NW, b) SEM micrograph of NW with EBID clamps, c) Height trace, d) 3D AFM scan of NW, e) 3D AFM scan of NW after fracture, f) Original loading-unloading curve, g) Extracted AFM loading-unloading curve showing fracture, h) Extracted force vs displacement plot, i) YM of 49.4 GPa was extracted from Matlab curve fit, and j) Matlab Curve fit extended up to the fracture point, undergoes plastic deformation of ~7-8 nm.
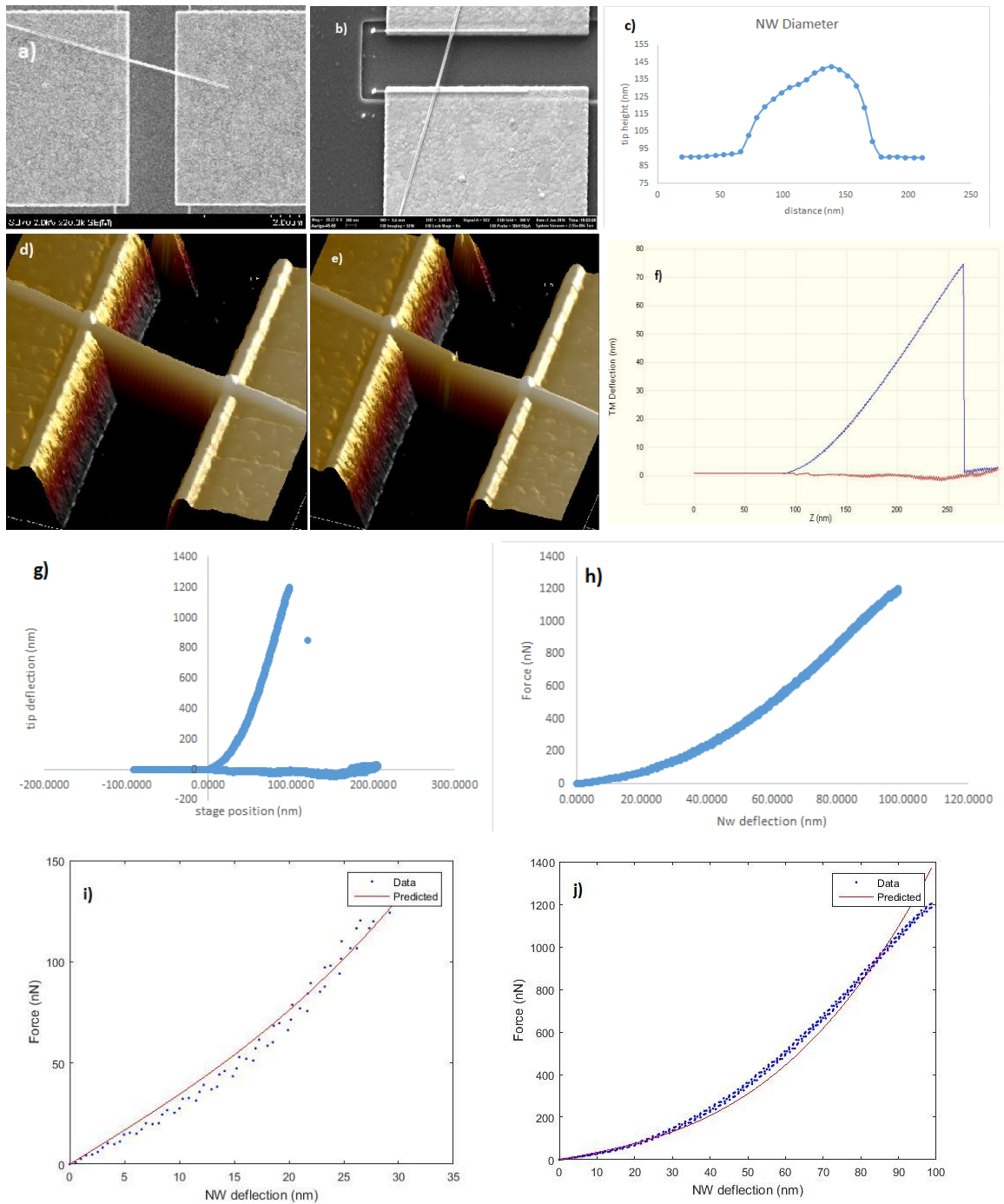
Figure 5.8: DEP Sample 2 a) SEM micrograph of NW, b) SEM micrograph of NW with EBID clamps, c) Height trace, d) 3D AFM scan of NW, e) 3D AFM scan of NW after fracture, f) Original loading-unloading curve, g) Extracted AFM loading-unloading curve showing fracture, h) Extracted force vs displacement plot, and i) YM of 48.2 GPa was extracted from Matlab curve fit, and j) Matlab Curve fit extended up to the fracture point.
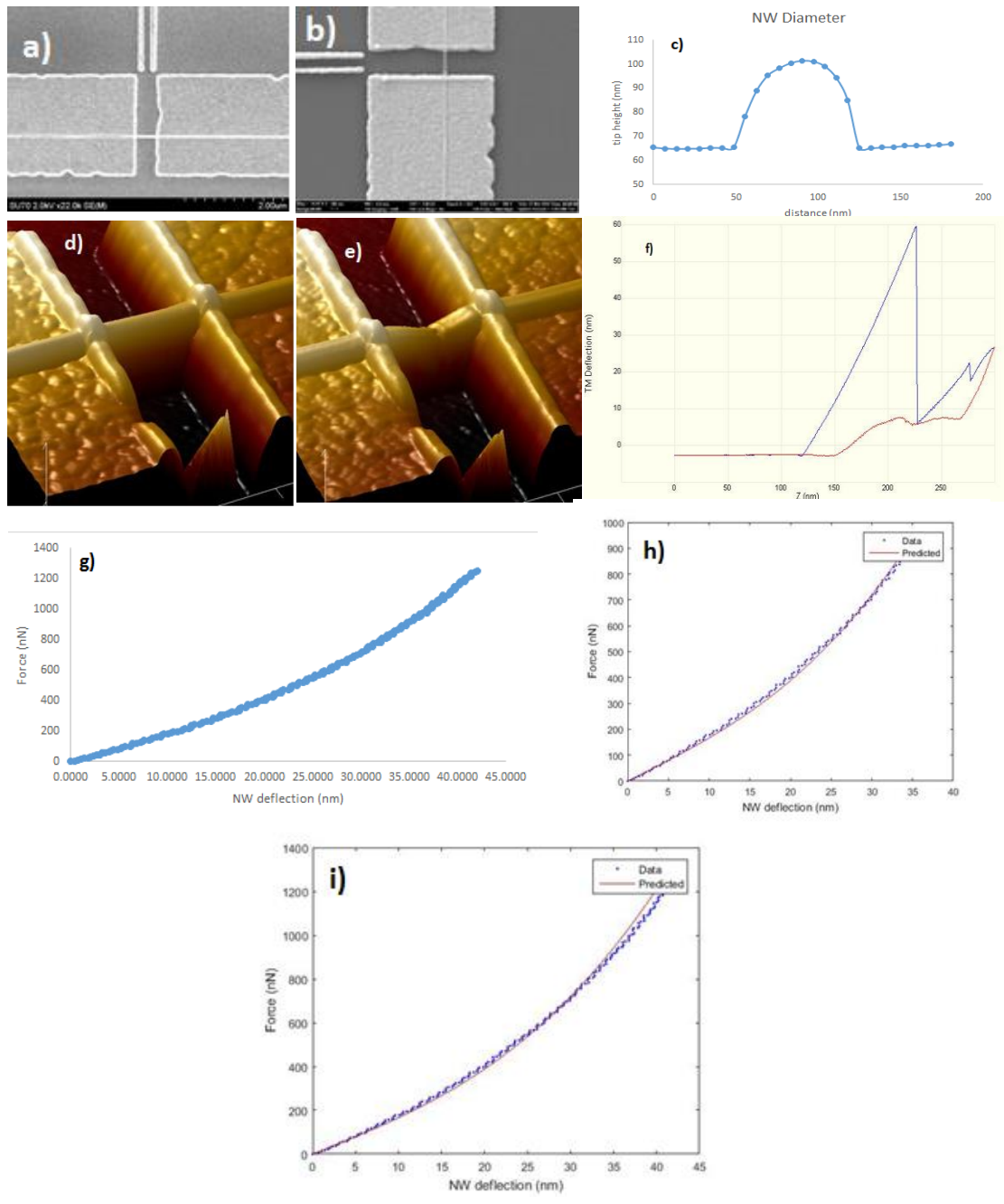
Figure 5.9: DEP Sample 3 a) SEM micrograph of NW, b) SEM micrograph of NW with EBID clamps, c) Height trace, d) 3D AFM scan of NW, e) 3D AFM scan of NW after fracture, f) Original loading-unloading curve, g) Extracted force vs displacement plot, h) YM of 41.8 GPa was extracted from Matlab curve fit, and i) Matlab Curve fit extended up to the fracture point.

Table 5.1: Summary of parameters for DEP step

Sample	DEP diameter	Young's Modulus (GPa)	Ultimate Strength (GPa)	Plastic Deformation	Theoretical Strength (Gpa)	Experimental-to-Theoretical ratio
1	36.1	49.4	5.8	Yes, 7-8 nm	7.8	73.73%
2	52.1	48.2	4.7	Yes	8.3	61.4%
3	40.2	42	6.7	Yes, 2 nm	6.7	99.63%
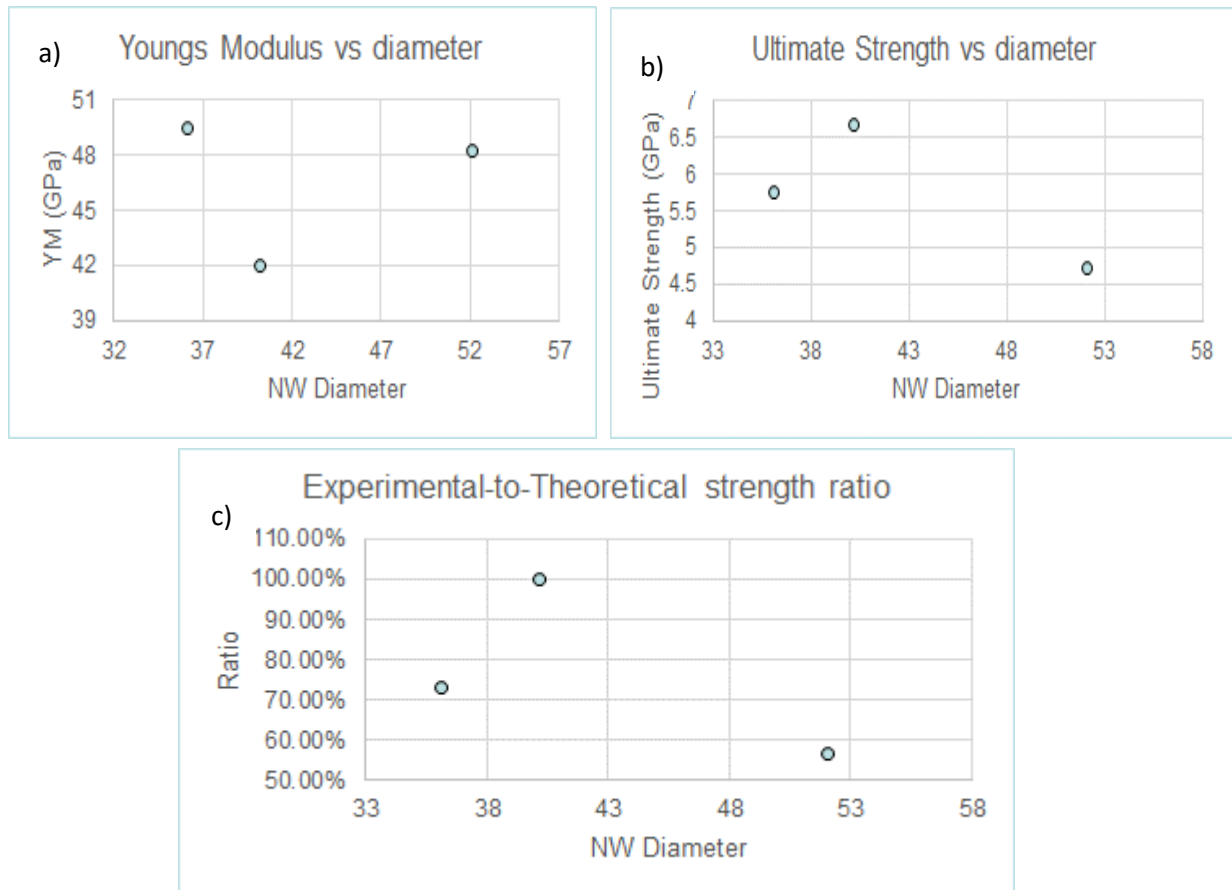
Figure 5.10: Plots for DEP samples a) Young's modulus vs % increase in diameter, b) Ultimate strength vs % increase in diameter, and c) Experimental-to-theoretical strength ratio vs % increase in diameter.

The theoretical strength of the nanowire can be calculated as $E/2\pi$.[194] The ratio of the experimental to theoretical values for the fracture strength of these nanowires was observed to be an average of 78% of the predicted theoretical strength for this NW material. This high ratio indicates that these NW crystals are relatively defect-free[195].

Next, the results from nanomechanical measurements involving one other battery nanomaterial system (lithium iron phosphate nanowires) are presented. Lithium iron phosphate has been commercially used in real-time applications for its advantages of low self-discharge rate, safe rapid recharge, nontoxicity, low cost and higher cycling capacity. A measurement of its YM will be useful to model the stress fields and fracture in this material system during its lithiation. In order to meet this need, contact mode AFM force spectroscopy was performed on these nanowires and Young's modulus values were extracted from F-d plots. Figure 5.11 (a-c) gives the SEM images of these nanowires, which are deposited in device regions similar to other material systems using DEP. The DEP parameters used in this experiment were $6V_{P-P}$, 1 kHz frequency and 2min of deposition time. It can be observed that the diameters of these materials are extremely high with a range of 150-300 nm in radius. Three-point bending technique, as described earlier, is suitable for use in small diameter (<100 nm) NWs. Nano-indentation mode was commonly used in such cases where the nanowires have low-aspect ratio and large diameters. However, in regular indentation based experiments, there exists two region of contacts: contact of the tip with the top surface of the NW and the NW being attached to a substrate. In this technique, the contact between NW and substrate is eliminated with the NW being suspended in the air. This

can be clearly seen from AFM 3D plots, as shown in Figure 5.11 (d). Also, AFM section plots can

be used to measure the diameter of the nanowire as shown in Figure 5.11 (f).
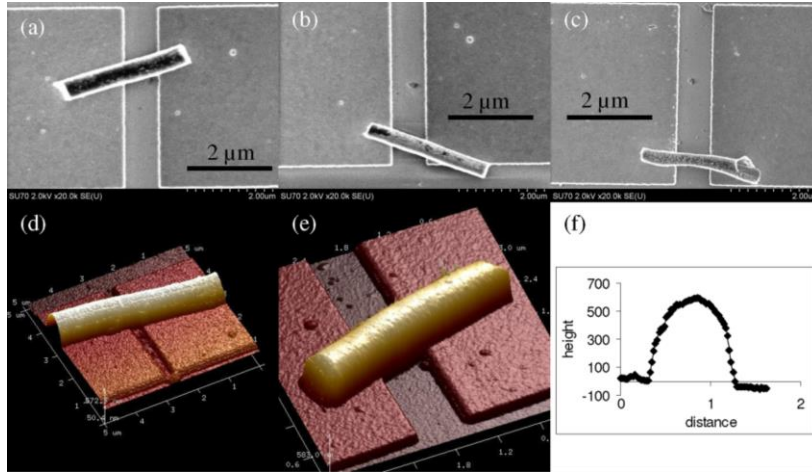
Figure 5.11: a-c) SEM images of assembled NWs. d-e) AFM 3-D images of NWs. f) AFM Section plot of one NW, diameter is 571 nm, image reproduced from ref. [110]

Indentation based atomic force spectroscopy measurements were performed at the center of

each NW and the F-d data plots were obtained. This data was processed in the same procedure

that was described earlier in the chapter. One such plot is shown in Figure 5.12 (a). However, it

is important to understand that, since the diameter of the NW is large, it undergoes both bending

(beam like bending in the suspended region) and indentation-induced localized deformation (at

the contact point of the AFM probe on the surface). Thus, to exactly estimate the contribution of

each mode on the Young's modulus, ANSYS FEM software simulations were performed[110].

A NW having a radius of 168nm and a suspended length of 400nm is shown in Fig. 5.12 (a - c). Its

Young's modulus value is estimated to be 113 MPa. Also, the Young's modulus was found to vary

with diameter, as seen in Fig 5.12 (d). For radii ranging between 168 to 182 nm, the Young's

modulus was in the range of 100 to 120 MPa and for radius ranging between 228 to 255 nm, it

was in the range of 220 to 255 MPa, twice that of the smaller diameters.
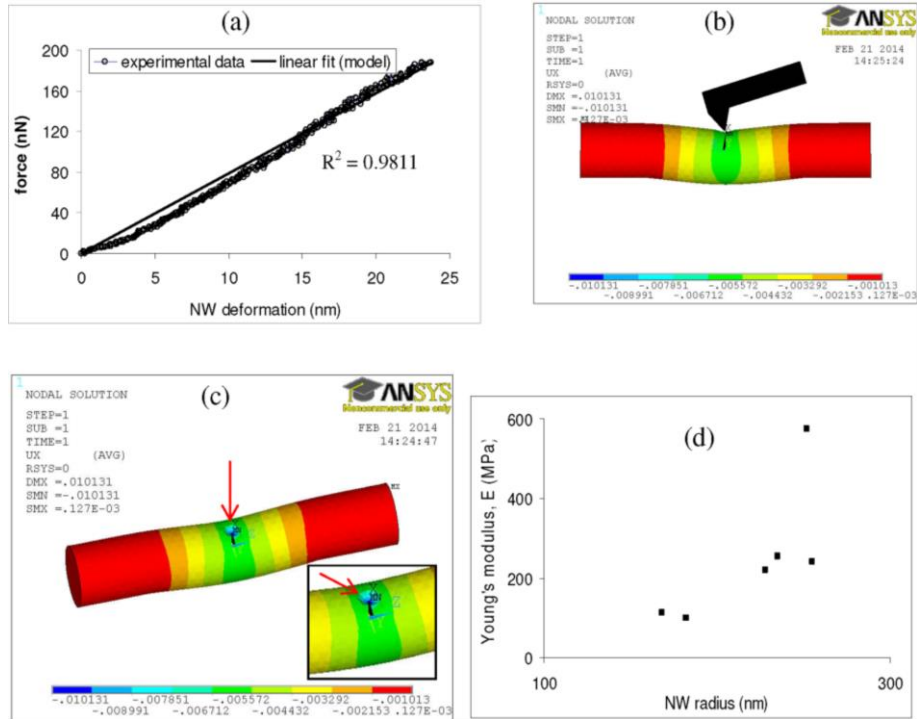
Figure 5.12: a) F-d plot of one LiFePO$_4$ NW, b) Ansys FEM model – Side View showing bending of NW, c) ANSYS FEM modeling, which was performed by Dr. Subramanian – 3D View showing point of contact of AFM tip and induced deformation, and d) Young's modulus variation with diameter, image reproduced from ref. [110]

Chapter 6: Degradation Study

6.1) Introduction:

Past measurements of charge capacity as a function of cycling have shown that there is a large drop in electrode performance at the end of the first charge/discharge cycle. The first part of this dissertation has studied the material changes during this first cycle that result in a drop in capacity. However, after the first cycle, there is a continuous but, slower drop in capacity over the lifetime of the battery electrode. The reasons for this slow degradation of the battery electrode have not been fully understood so far and current chapter will focus on this need. Specifically, the material properties of a battery nanowire electrode will be tested at the end of 20 cycles of lithiation.
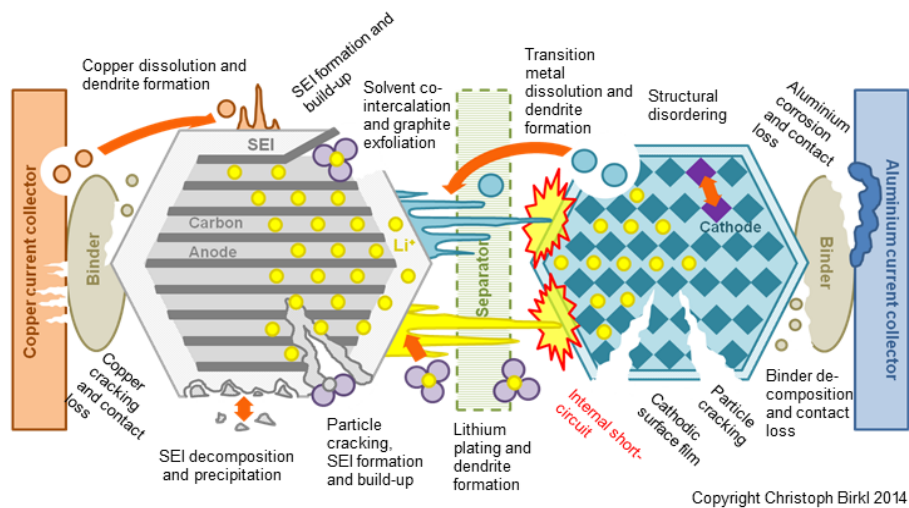
Figure 6.1: Degradation mechanisms in Li-ion batteries

A rechargeable battery needs to have the capability to survive several hundreds of charge/discharge cycles and so this study is especially important to understand, and improve the lifetime of a battery electrode. This is also known as a degradation study. Some of the many physical and chemical processes that contribute to battery degradation are shown in Figure 6.1 and the remaining steps are expected to provide new knowledge on some of these aspects related to the degradation in a battery system.

Battery electrode materials offer different characteristics at the nanoscale, and a fundamental understanding of the mechanism of battery degradation for each material helps in identifying the failure modes of the material, and thereby enable pathways to improve electrochemical behavior. This chapter extends the single nanowire electrochemical study presented in Chapter 3 with necessary modifications, and thereby develop the capability to test the mechanical behavior of nanomaterial for 20 cycles of lithiation.

6.2) Experiments:

The electrochemical lithiation experimental setup is same as Figure 3.1, and degradation study on α-MnO_2 was conducted at unlithiated, first discharge, first full cycle lithiation and 20 cycles of lithiation steps. The electrical output from function generator is set as a square wave with 4V as higher voltage limit that represents charging (lithium ions move from nanowire back into electrolyte and lithium wire anode), and 1.5V is set as a lower limit for discharging (lithium ions move from lithium wire anode through electrolyte into the nanowire). The time period was fixed

at 1 min each for charging and discharging cycle, and the square wave is set at 50% duty cycle. This setup completes a full electrochemical cycle.

For every stage, following steps were performed according to the study:

1) Firstly, α-MnO_2 nanowires are deposited onto desired locations on the chip using dielectrophoresis, the process is discussed in Chapter 2. AFM scans are performed on single nanowire locations to determine the diameter of the nanowire. This step is done in order to achieve a better height plot of the nanowire, considering the minimal roughness of the gold electrode pad surface during this process.

2) Based on the lithiation test cycle in study, the lithiation experiment is performed inside a glove box according to the procedure described above. For example, in the 20 cycle lithiation step, the nanowires are dipped in electrolyte inside the glove box for a total of 40 minutes.

3) After lithiation is complete, AFM scans are again performed to determine the post lithiation diameter. These values can be used to calculate the % increase in diameter for every stage of lithiation.

4) EBID clamps are then placed on both sides of the nanowire to provide good surface contact and thereby reduce contact resistance. This particular step is different from the earlier study presented in Chapter 3, as we found that lithiating the nanowires after placing EBID clamps leaves a carbon coating near the clamp regions, and effects the AFM height plots for accurate diameter measurements.

5) Finally contact-mode AFM is used to fracture the nanowires, and Young's modulus and ultimate strength of the material are determined according to the procedure described in Chapter 5.

The results for the unlithiated stage were discussed in chapter 5. The Young's modulus and ultimate strength of those nanowires were found to lie in the range of 40 to 50 GPa and 4.7 to 6.6 GPa, respectively. The nanowires exhibited relatively defect-free single-crystalline behavior with an experimental-to-theoretical strength ratio of 78%. In this chapter, nanomechanical measurements are presented at the following SOCs: first discharge, first full cycle of lithiation and 20 cycles of lithiation.

It is important to note that an extension of this capability for longer duration lithium cycling is limited by the stability of the electrolyte suspension for durations longer than ~1 hour. In an open cell configuration, as is needed for these single NW tests, the electrolyte tends to solidify over periods lasting more than an hour. As a result, these measurements have been limited to the first 20 cycles in this thesis. However, it is important to note that this represents an important advance from past efforts due to the following key considerations: (1) the biggest change in charge capacity reduction for a battery electrode occurs during the first few cycles and the degradation of the electrode at this important step has already been captured in these experiments, (2) capacity loss beyond the first few cycles typically exhibits a slow and gradual fade (see Fig. 4.12) and a study of up to 20 cycles is representative of the smaller changes that occur within the material during this extended cycling period, and (3) past efforts involving single particle battery

diagnostics have only tested the material either at the end of the first lithiation step or at the end of the first charge-discharge cycle. This limitation with past efforts has been due to constraints in building lithium cells using robotic nanomanipulations within an electron microscope. However, this thesis has adopted a new approach to build lithium cells on silicon chips and presented a transformative diagnostic methodology, which is able to test the material system over comparatively longer cycling durations.

6.3) First discharge step

The results from the first discharge step are summarized in this section. The table below lists the pre- vs. post-lithiation nanowire diameter (to indicate size changes), Young's modulus of the lithiated NW, fracture strength of the lithiated NW, the occurrence of plastic deformation (if any), and experimental-to-theoretical fracture strength ratio for five different NW samples. These results are also summarized in Figure 6.2.

Figures 6.3 to 6.5 provide detailed information from the measurements involving three representative NW samples. This includes: (i) SEM images of the NWs, before and after EBID clamping at the anchor points, (ii) tapping mode AFM scans of the NWs, before and after fracture measurements, (iii) AFM height traces used for diameter measurements, (iv) raw force spectroscopy data, and (v) processed NW force-vs deflection plots and their curve fit using MATLAB to extract Young's modulus and fracture strength.

Table 6.1. Summary of parameters for Discharge step

Sample	DEP diameter	Discharge 1min diameter	% Increase in diameter	Young's Modulus (GPa)	Ultimate Strength (GPa)	Plastic Deformation	Theoretical Strength (GPa)	Experimental-to-theoretical strength
1	21.4	24.1	0.13	108.3	6.0	No	17.2	34.57%
2	38.5	44.5	0.16	46.3	5.4	Yes, 7-10 nm	7.4	72.71%
3	30	32.6	0.09	112.2	7.0	Yes, >10nm	17.9	39.08%
4	N/A	27.9	N/A	71.5	5.4	No	11.4	47.01%
5	N/A	23.4	N/A	117.3	8.1	No	18.7	43.43%

From the results, it was observed that the average value for the Young's modulus of the material was 91 $\pm$ 27 GPa (based on measurements from 5 different NW samples). This value is higher than that of the unlithiated state at low concentrations of lithium loading (as represented by smaller increase in NW diameter), and can be attributed to the formation of new Li-O bonds in the tunnel structure when lithium is inserted. At the same time, the experimental-to-theoretical ratio drops to a lower level and indicates the increase in defect density within the material system. However, at higher levels of lithium loading we observe the YM of the material to drop thereby, indicating a softening of the material due to crystal distortions at large volume expansions.

Figure 6.2: Plots for first discharge step samples a) % Increase in diameter vs DEP diameter, b) Young's modulus vs % increase in diameter, c) Ultimate strength vs % increase in diameter, and d) Experimental-to-theoretical strength ratio vs % increase in diameter.

Figure 6.3: Discharge 1 min Sample 1 a) SEM micrograph of NW, b) SEM micrograph of NW with EBID clamps, c) Height trace, d) 3D AFM scan of NW, e) 3D AFM scan of NW after fracture, f) Original loading-unloading curve, g) Extracted AFM loading-unloading curve showing fracture, h) Extracted force vs displacement plot, and i) YM of 108.3 GPa was extracted from Matlab curve fit.
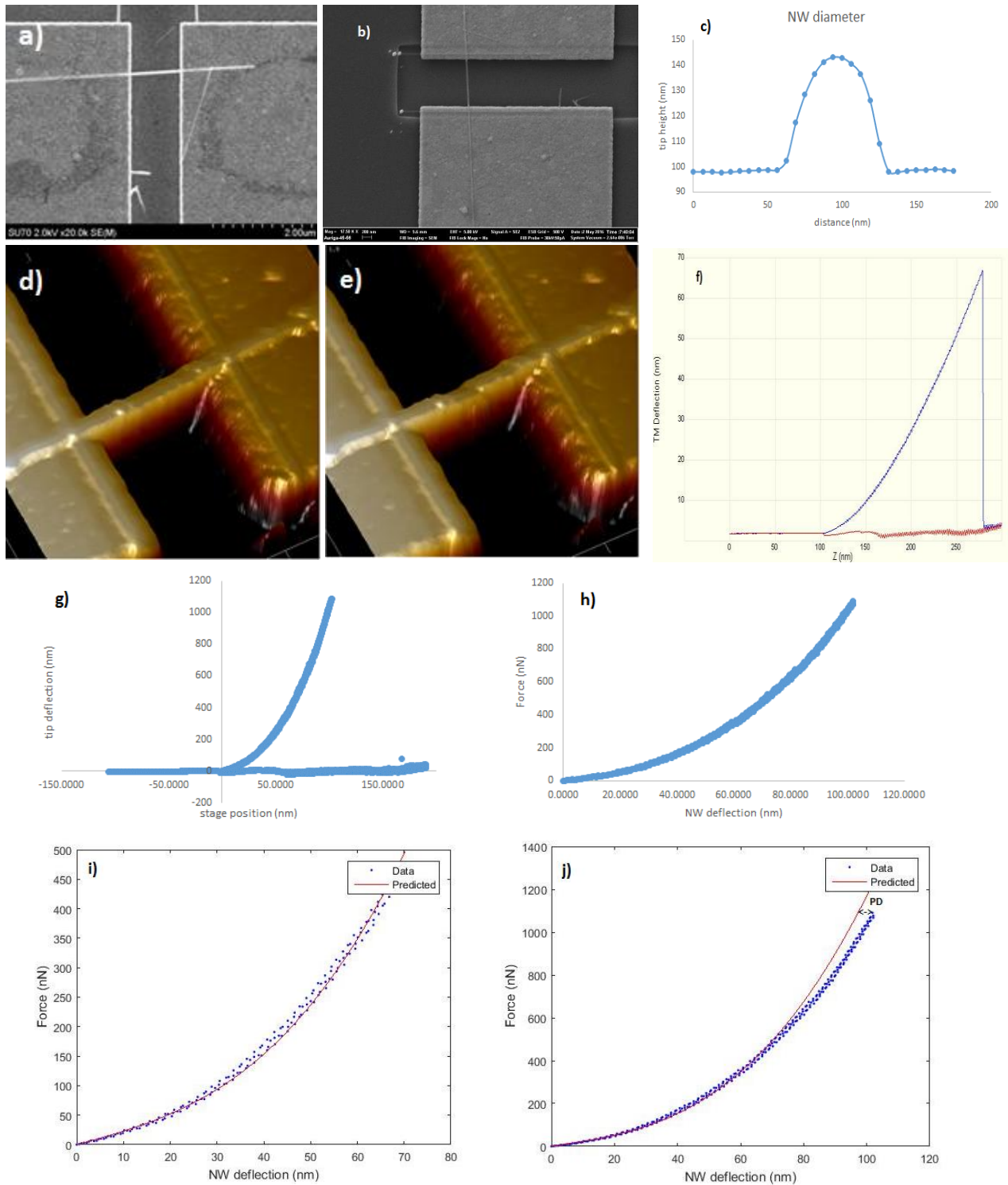
Figure 6.4: Discharge 1 min Sample 2 a) SEM micrograph of NW, b) SEM micrograph of NW with EBID clamps, c) Height trace, d) 3D AFM scan of NW, e) 3D AFM scan of NW after fracture, f) Original loading-unloading curve, g) Extracted AFM loading-unloading curve showing fracture, h) Extracted force vs displacement plot, i) YM of 46.3 GPa was extracted from Matlab curve fit, and j) Matlab Curve fit extended up to the fracture point, undergoes plastic deformation around 7-8 nm.

Figure 6.5: Discharge 1 min Sample 3 a) SEM micrograph of NW, b) SEM micrograph of NW with EBID clamps, c) Height trace, d) 2D AFM scan of NW, e) 2D AFM scan of NW after fracture, f) Original loading-unloading curve, g) Extracted AFM loading-unloading curve showing fracture, h) Extracted force vs displacement plot, i) YM of 112.2 GPa was extracted from Matlab curve fit, and j) Matlab Curve fit extended up to the fracture point, undergoes plastic deformation around 25 nm.

6.4) First cycle of lithiation

The results from the first discharge-charge cycle are summarized in this section. The table below lists the pre- vs. post-cycling nanowire diameter (to indicate size changes), Young's modulus of the lithiated NW, fracture strength of the lithiated NW, the occurrence of plastic deformation (if any), and experimental-to-theoretical fracture strength ratio for five different NW samples. These results are also summarized in Figure 6.6. Figures 6.7 and 6.8 provide detailed information from the measurements involving two representative NW samples. This includes: (i) SEM images of the NWs, before and after EBID clamping at the anchor points, (ii) tapping mode AFM scans of the NWs, before and after fracture measurements, (iii) AFM height traces used for diameter measurements, (iv) raw force spectroscopy data, and (v) processed NW force-vs deflection plots and their curve fit using MATLAB to extract Young's modulus and fracture strength.

Table 6.2. Summary of parameters for 1 cycle of lithiation

Sample	DEP diameter	1 Cycle Lithiation	% Increase in diameter	Young's Modulus (GPa)	Ultimate Strength (GPa)	Plastic Deformation	Theoretical Strength (GPa)	Exp-to-Theoretical ratio
1	37.9	42.1	0.11	40.2	4.0	No	6.4	61.76%
2	35	40.6	0.16	42.4	2.9	No	6.8	42.98%
3	32.5	34	0.05	49	3.1	Yes, 7 nm	7.8	39.71%
4	N/A	47.7	N/A	24	1.9	No	3.8	49.74%
5	28.5	30.3	0.06	50.9	2.2	No	8.1	27.51%

From the presented data, it can be observed that the Young's modulus of the NWs drops an average value of 41.4 $\pm$ 9.3 GPa (based on 5 NW samples). This is near the value observed for the un-lithiated material. This points to the fact that the de-lithiated material, after the loss of Li-O bonds that were established during lithiation or NW discharge, softens and exhibits a modulus that is similar to that of the as-synthesized NWs. However, the material after one lithiation cycle, presents a much smaller experimental-to-theoretical ratio for the fracture strength. This points to the increase in defect density within the NW material to the first discharge-charge cycle.
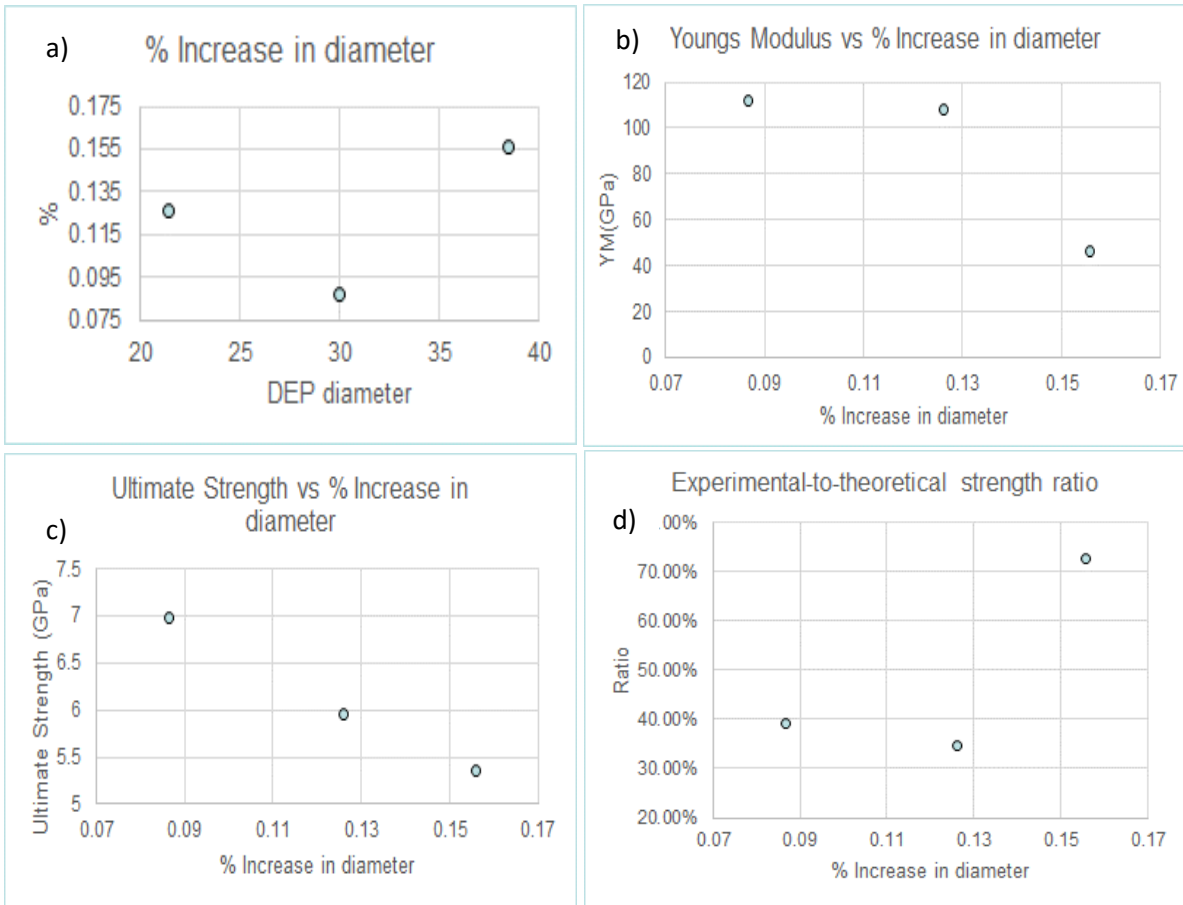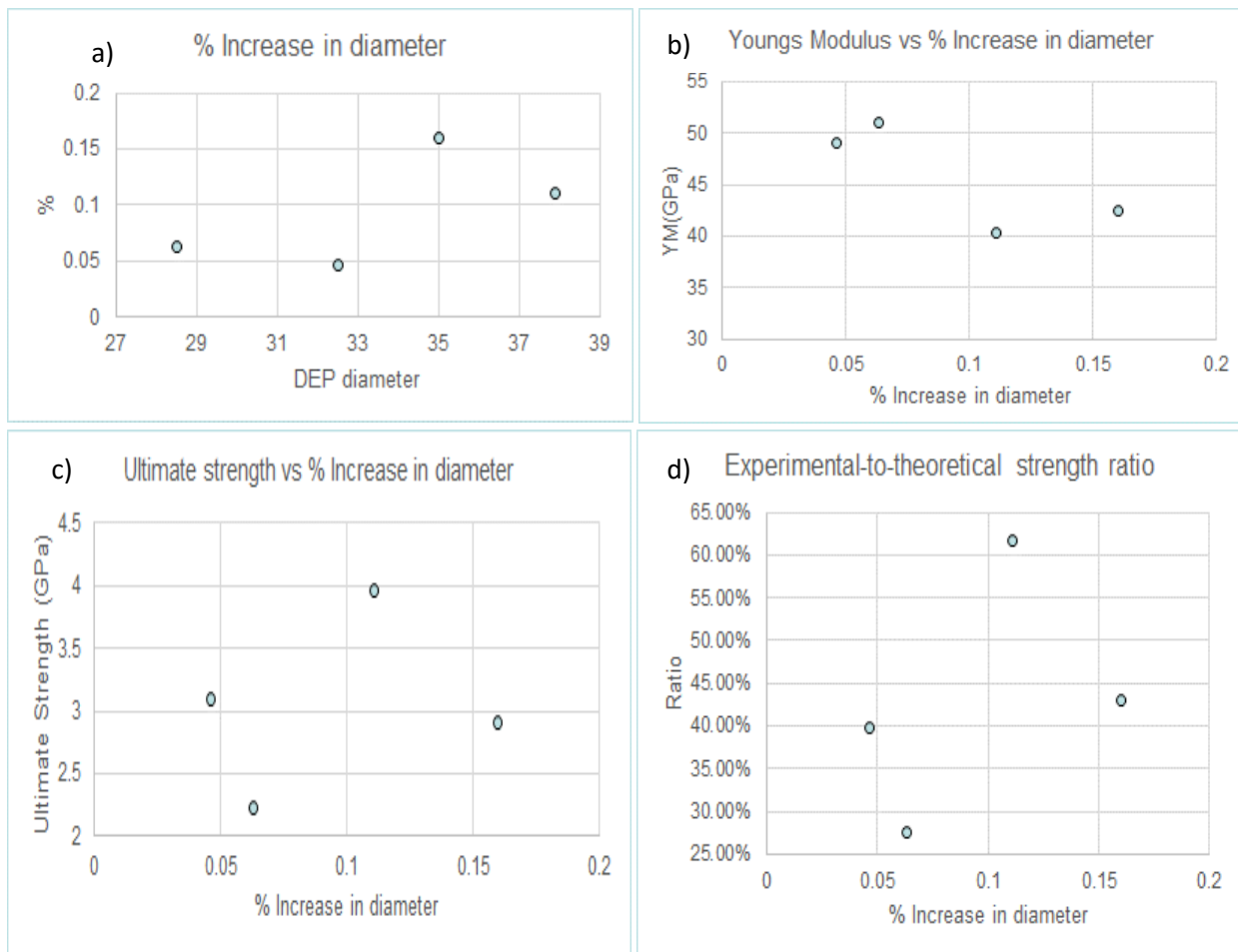
Figure 6.6: Plots for 1ˢᵗ cycle lithiation samples a) % Increase in diameter vs DEP diameter, b) Young's modulus vs % increase in diameter, c) Ultimate strength vs % increase in diameter, and d) Experimental-to-theoretical strength ratio vs % increase in diameter.

Figure 6.7: 1 Cycle Sample 1 a) SEM micrograph of NW, b) SEM micrograph of NW with EBID clamps, c) Height trace, d) 3D AFM scan of NW, e) 3D AFM scan of NW after fracture, f) Original loading-unloading curve, g) Extracted AFM loading-unloading curve showing fracture, h) Extracted force vs displacement plot, i) YM of 40.2 GPa was extracted from Matlab curve fit, and j) Matlab Curve fit extended up to the fracture point, undergoes plastic deformation around 25 nm.
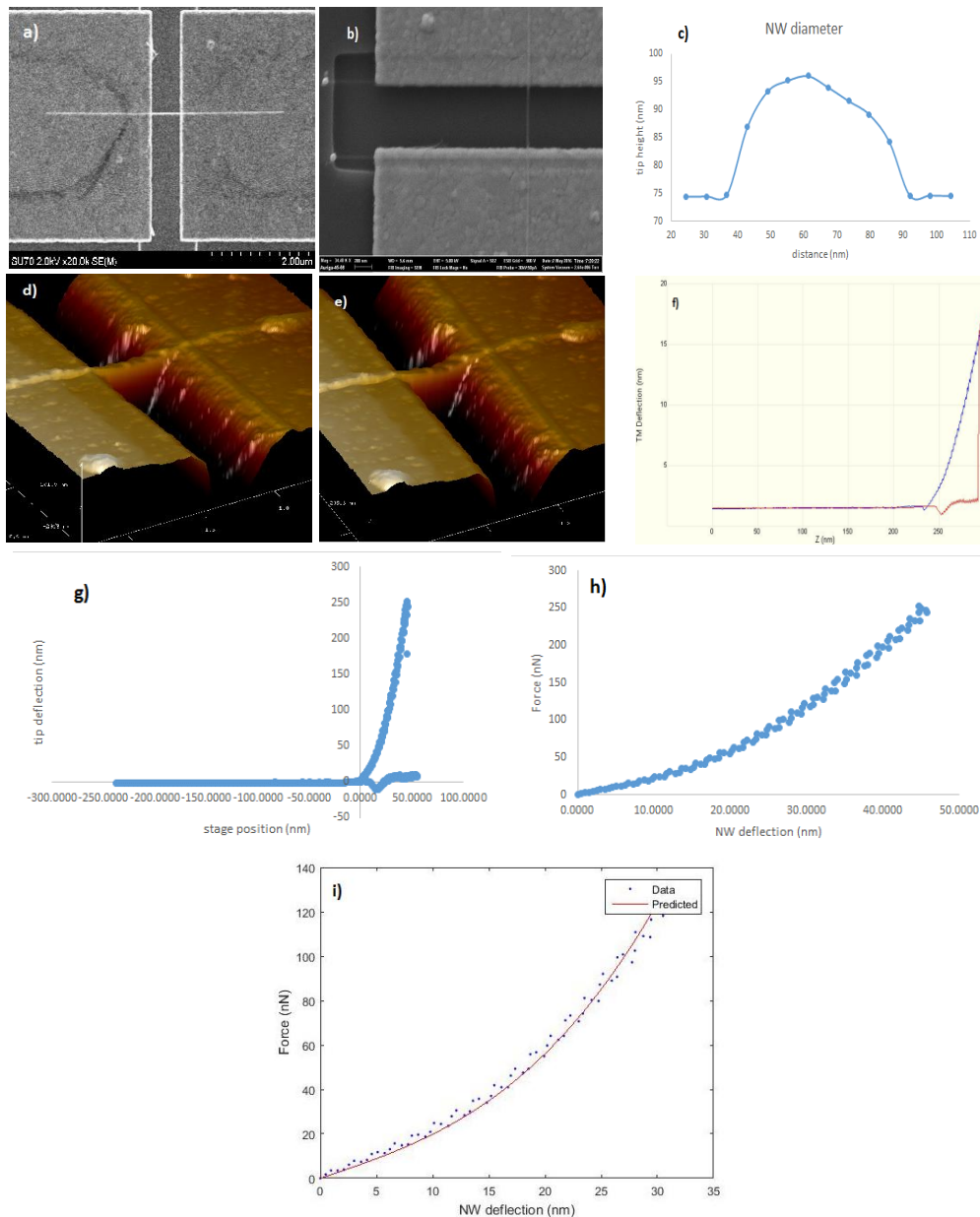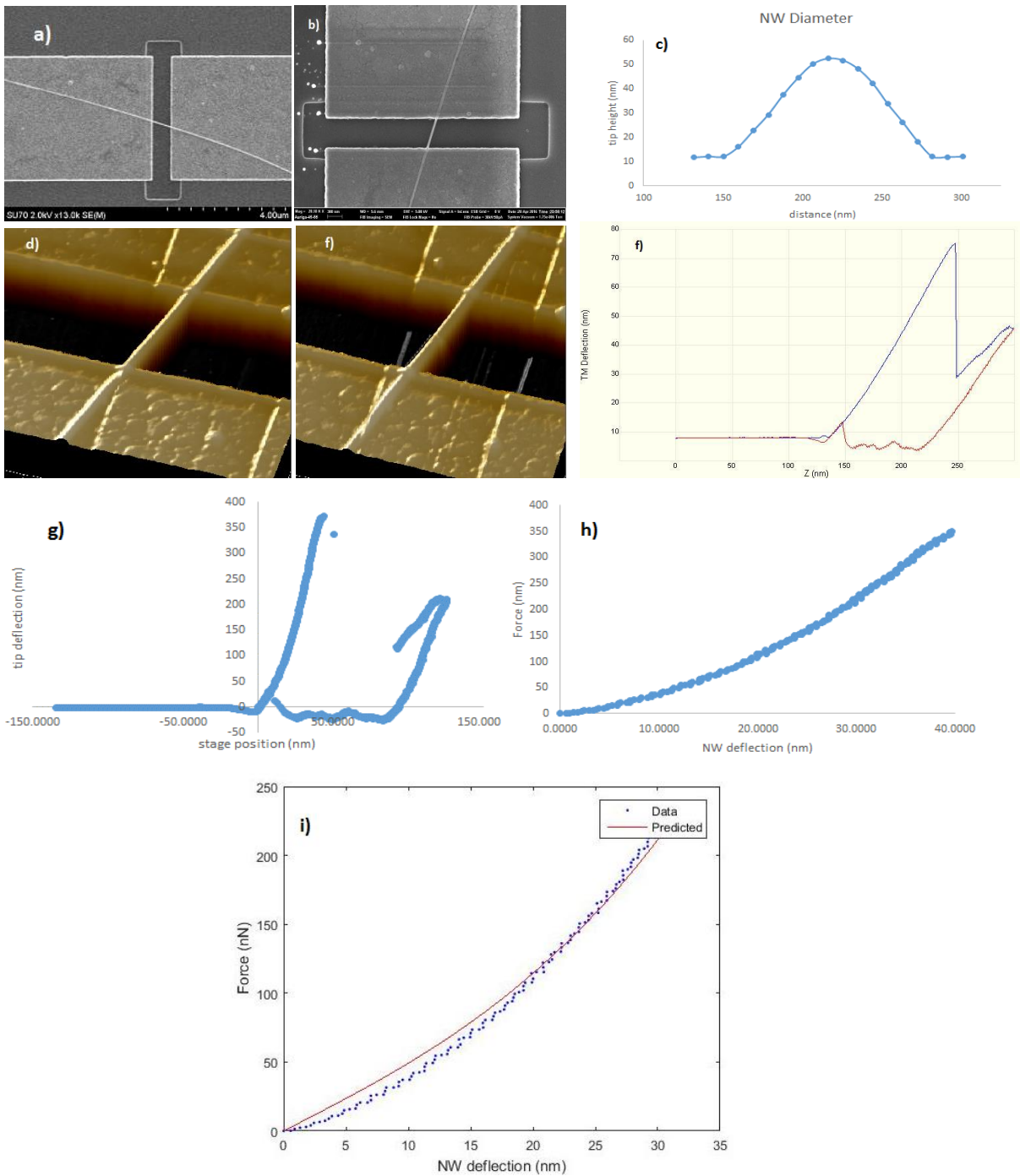
Figure 6.8: 1 Cycle Sample 2 a) SEM micrograph of NW, b) SEM micrograph of NW with EBID clamps, c) Height trace, d) 3D AFM scan of NW, e) 3D AFM scan of NW after fracture, f) Original loading-unloading curve, g) Extracted AFM loading-unloading curve showing fracture, h) Extracted force vs displacement plot, and i) YM of 42.4 GPa was extracted from Matlab curve.
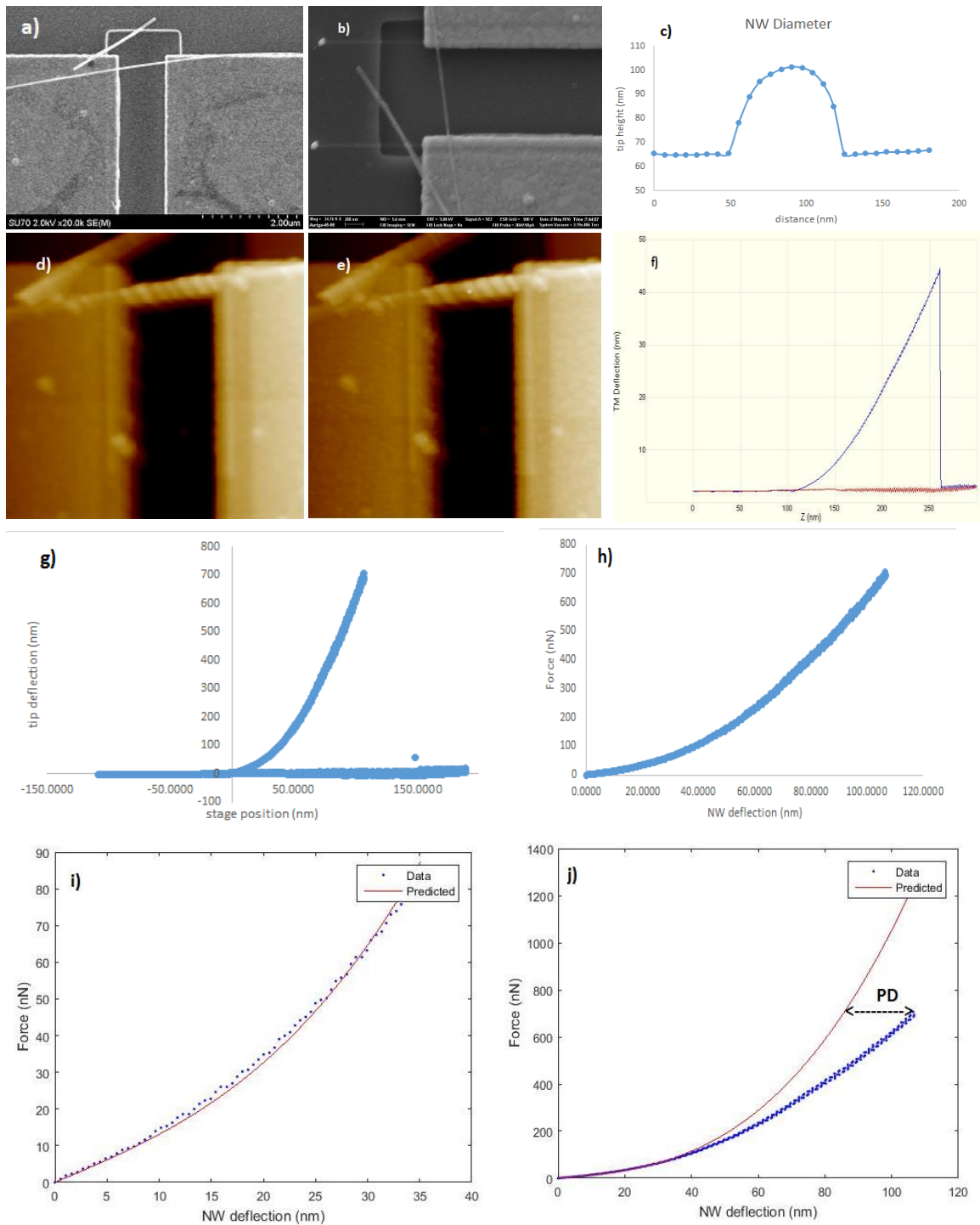
6.5) 20 cycles of lithiation

The measurement results from the 20-cycle lithiation experiments are summarized in this section. The table below lists the pre- vs. post-cycling nanowire diameter (to indicate size changes), Young's modulus of the lithiated NW, fracture strength of the lithiated NW, the occurrence of plastic deformation (if any), and experimental-to-theoretical fracture strength ratio for five different NW samples. These results are also summarized in Figure 6.9. Figures 6.10 to 6.13 provide detailed information from the measurements involving representative NW samples. This includes: (i) SEM images of the NWs, before and after EBID clamping at the anchor points, (ii) tapping mode AFM scans of the NWs, before and after fracture measurements, (iii) AFM height traces used for diameter measurements, (iv) raw force spectroscopy data, and (v) processed NW force-vs deflection plots and their curve fit using MATLAB to extract Young's modulus and fracture strength.

Table 6.3. Summary of parameters for 20 cycles of lithiation

Sample	DEP diameter	Lithiation 20 Cycles diameter	% Increase in diameter	Young's Modulus (GPa)	Ultimate Strength (GPa)	Plastic Deformation	Theoretical Strength (GPa)	Exp-to-theoretical ratio
1	26.4	33	0.25	94.7	4.1	No	15.1	27.03%
2	20.2	23.6	0.17	60.3	2.5	No	9.6	26.34%
3	28.7	34.2	0.19	73.9	5.9	Yes, 4-5 nm	11.8	49.73%
4	29.1	38.6	0.33	48.3	4.6	Yes, 3.5-4nm	7.7	59.28%
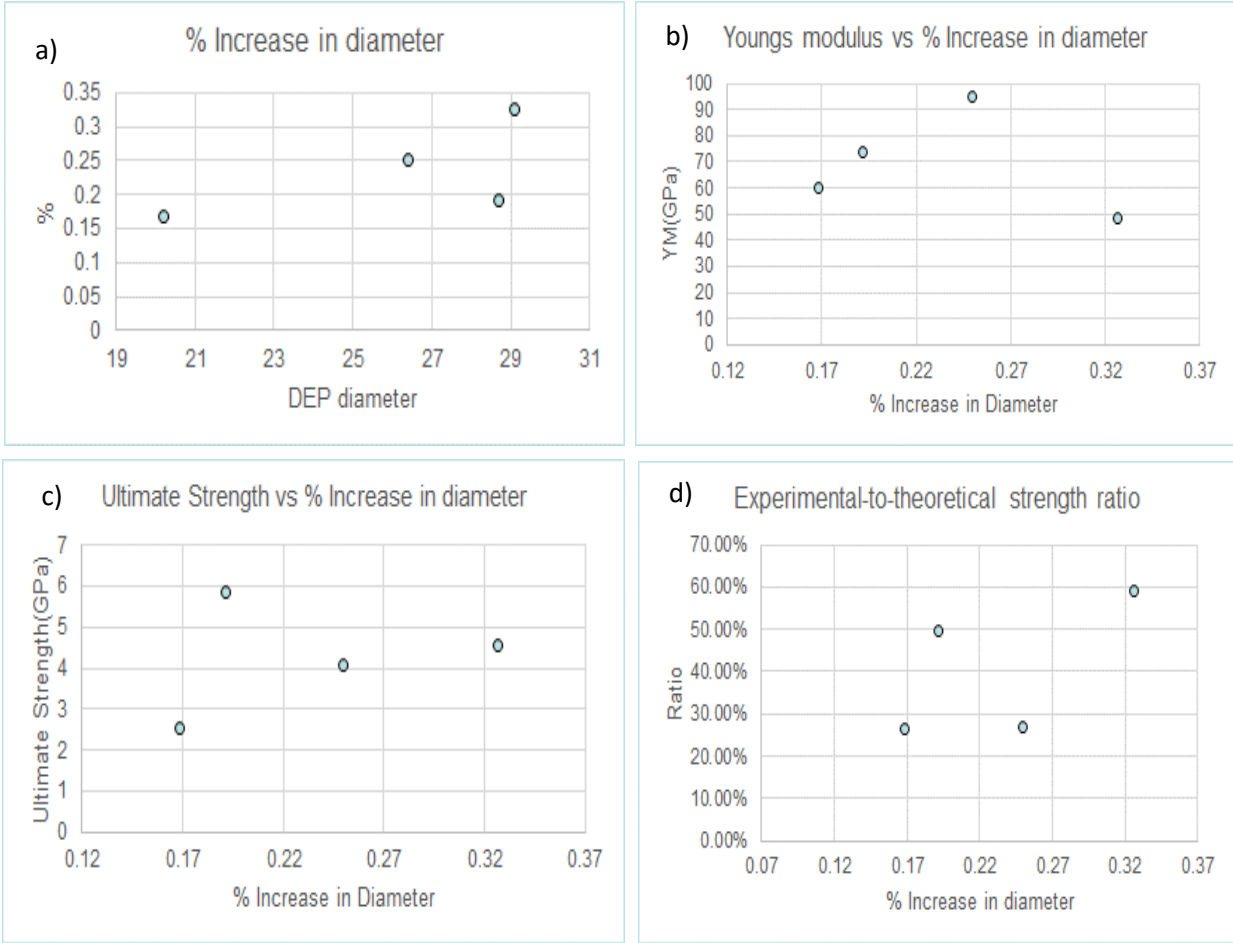
Figure 6.9: Plots for 20 cycles lithiation samples a) % Increase in diameter vs DEP diameter, b) Young's modulus vs % increase in diameter, c) Ultimate strength vs % increase in diameter, and d) Experimental-to-theoretical strength ratio vs % increase in diameter.

From the results, it can be observed that the Young's modulus of the material assumes an average value of 69.3 ± 19.5 GPa. This is higher than that of the unlithiated state. At the same time, the experimental-to-theoretical strength of the material is very low. This can be attributed to the fact that cycling causes the material to constantly undergo structural changes and eventually disintegrate. This phenomenon can be explained better using Figure 6.15[126].
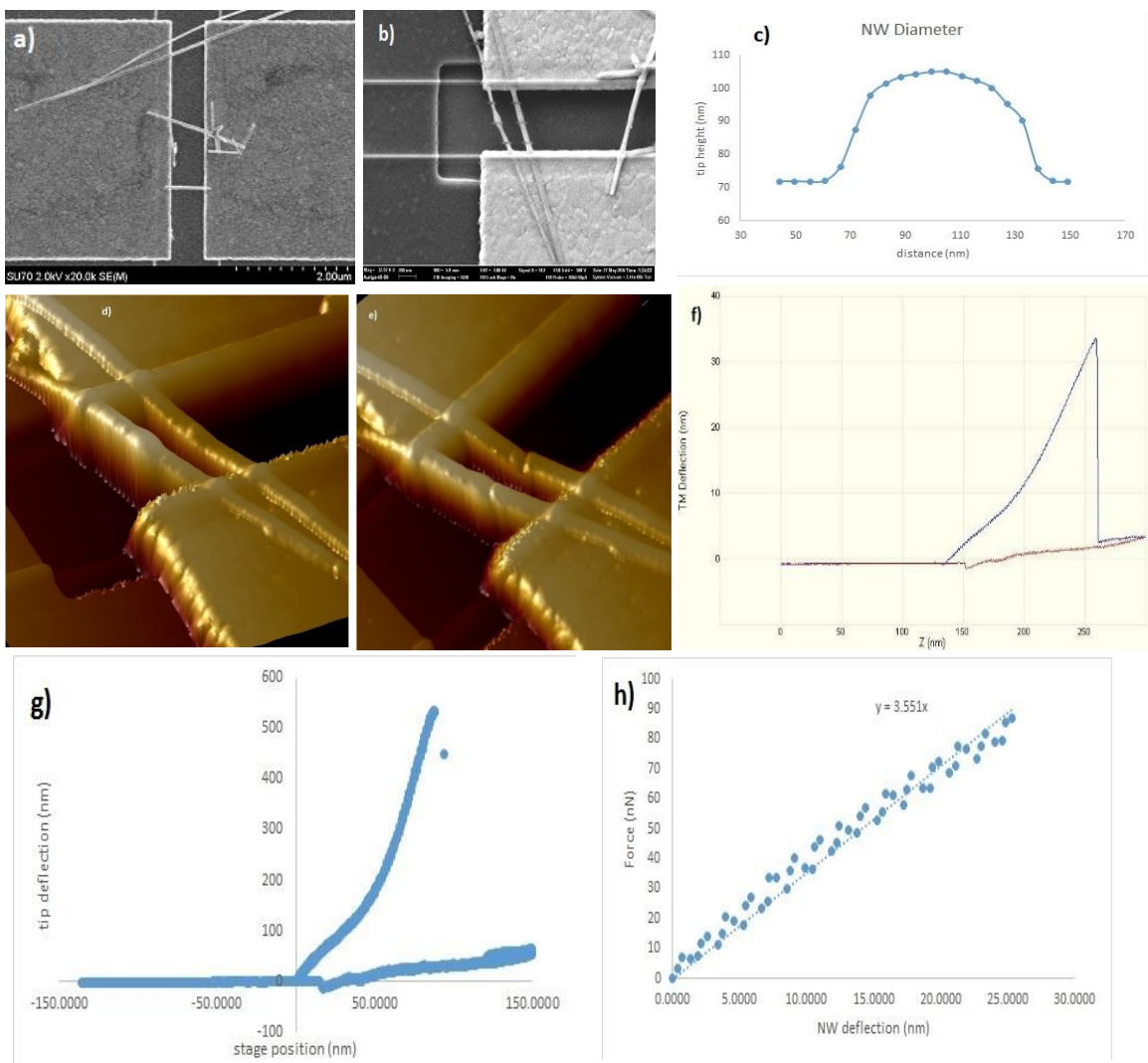
Figure 6.10: 20 Cycles Sample 1 a) SEM micrograph of NW, b) SEM micrograph of NW with EBID clamps, c) Height trace, d) 3D AFM scan of NW, e) 3D AFM scan of NW after fracture, f) Original loading-unloading curve, g) Extracted AFM loading-unloading curve showing fracture, and h) Extracted force vs displacement plot, YM of 94.7 GPa was extracted.
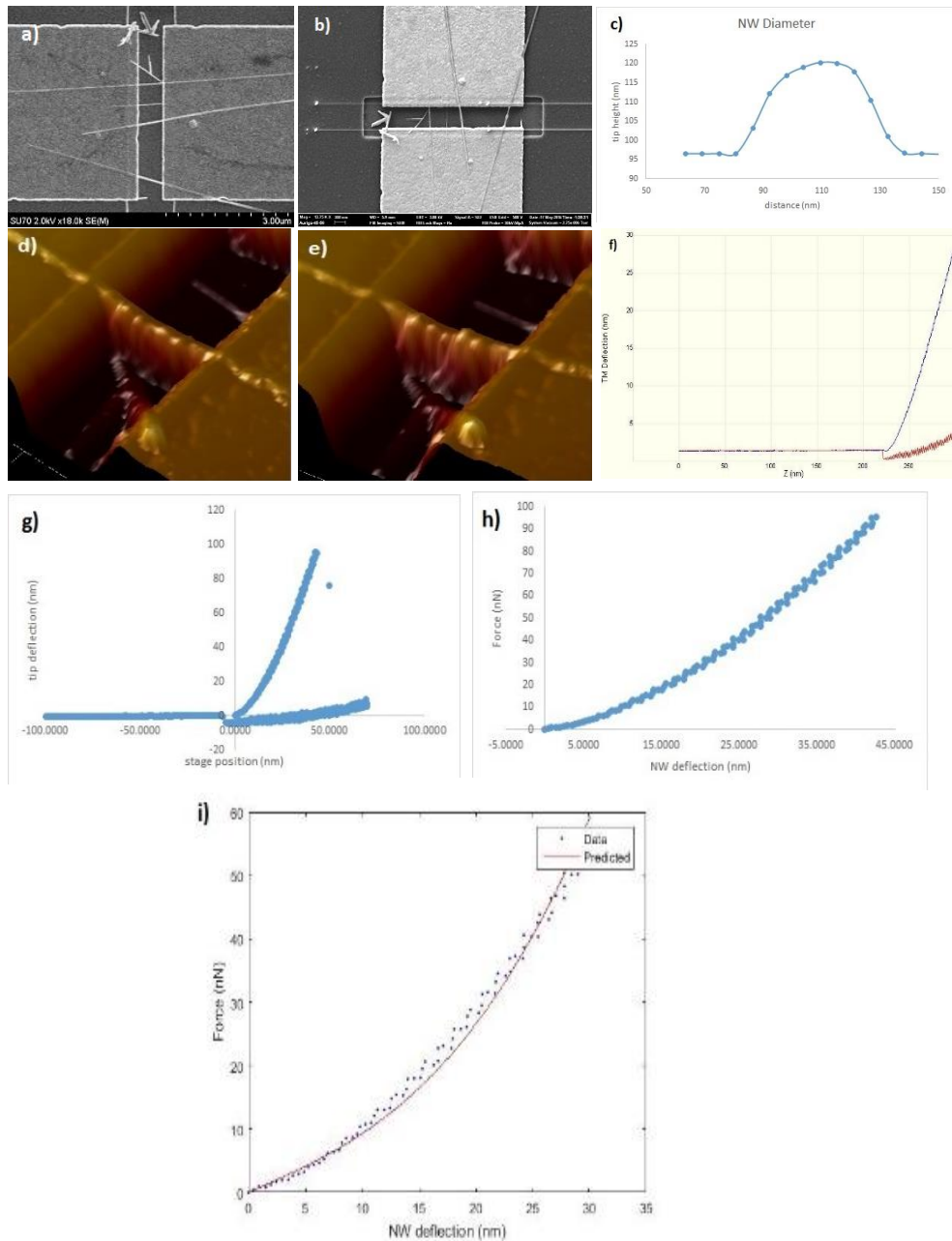
Figure 6.11: 20 Cycles Sample 2 a) SEM micrograph of NW, b) SEM micrograph of NW with EBID clamps, c) Height trace, d) 3D AFM scan of NW, e) 3D AFM scan of NW after fracture, f) Original loading-unloading curve, g) Extracted AFM loading-unloading curve showing fracture, and h) Extracted force vs displacement plot, and i) YM of 60.3 GPa was extracted from Matlab curve.
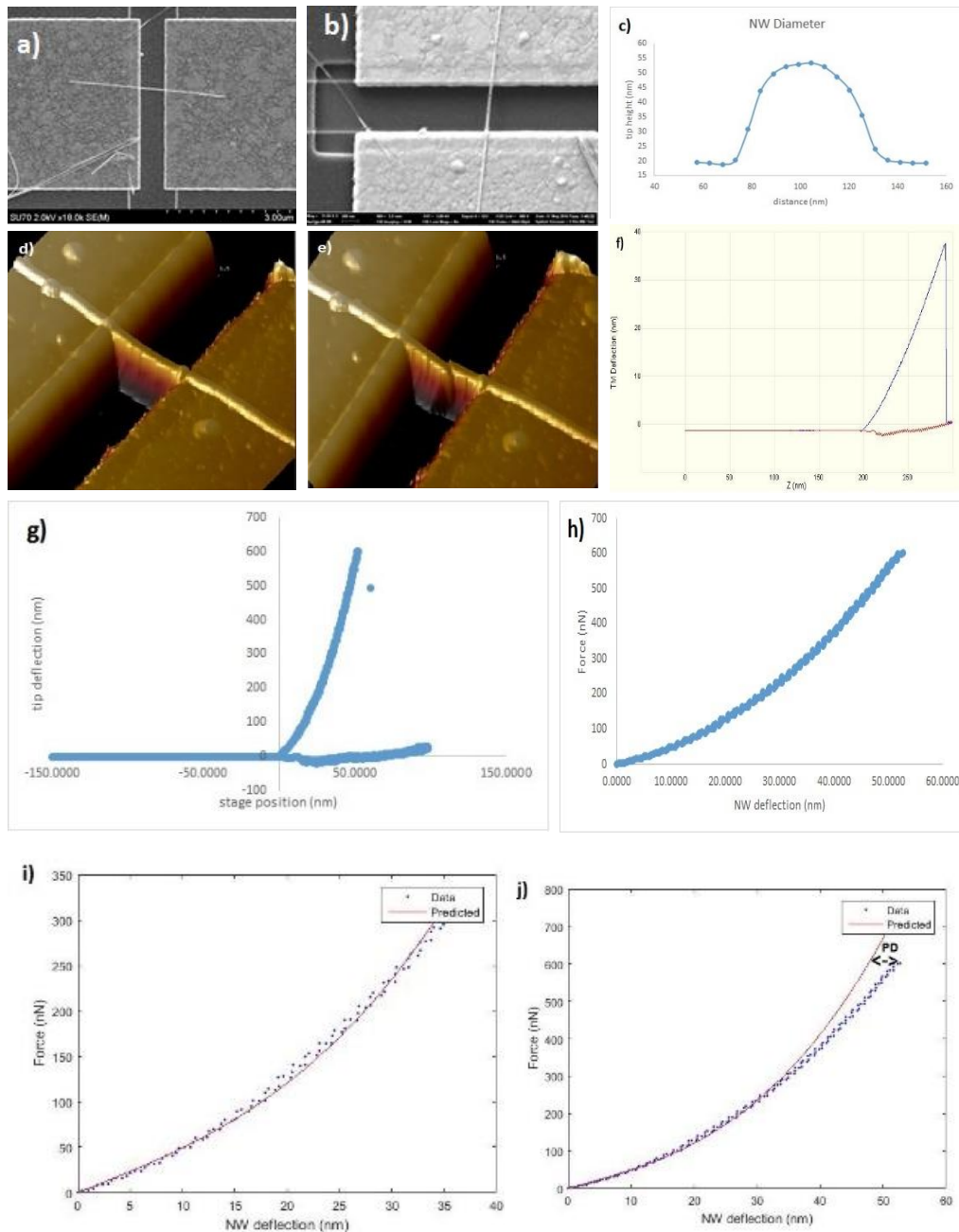
Figure 6.12: 20 Cycles Sample 3 a) SEM micrograph of NW, b) SEM micrograph of NW with EBID clamps, c) Height trace, d) 3D AFM scan of NW, e) 3D AFM scan of NW after fracture, f) Original loading-unloading curve, g) Extracted AFM loading-unloading curve showing fracture, and h) Extracted force vs displacement plot, i) YM of 73.9 GPa was extracted from Matlab curve and j) Matlab Curve fit extended up to the fracture point, undergoes plastic deformation around 4-5 nm.
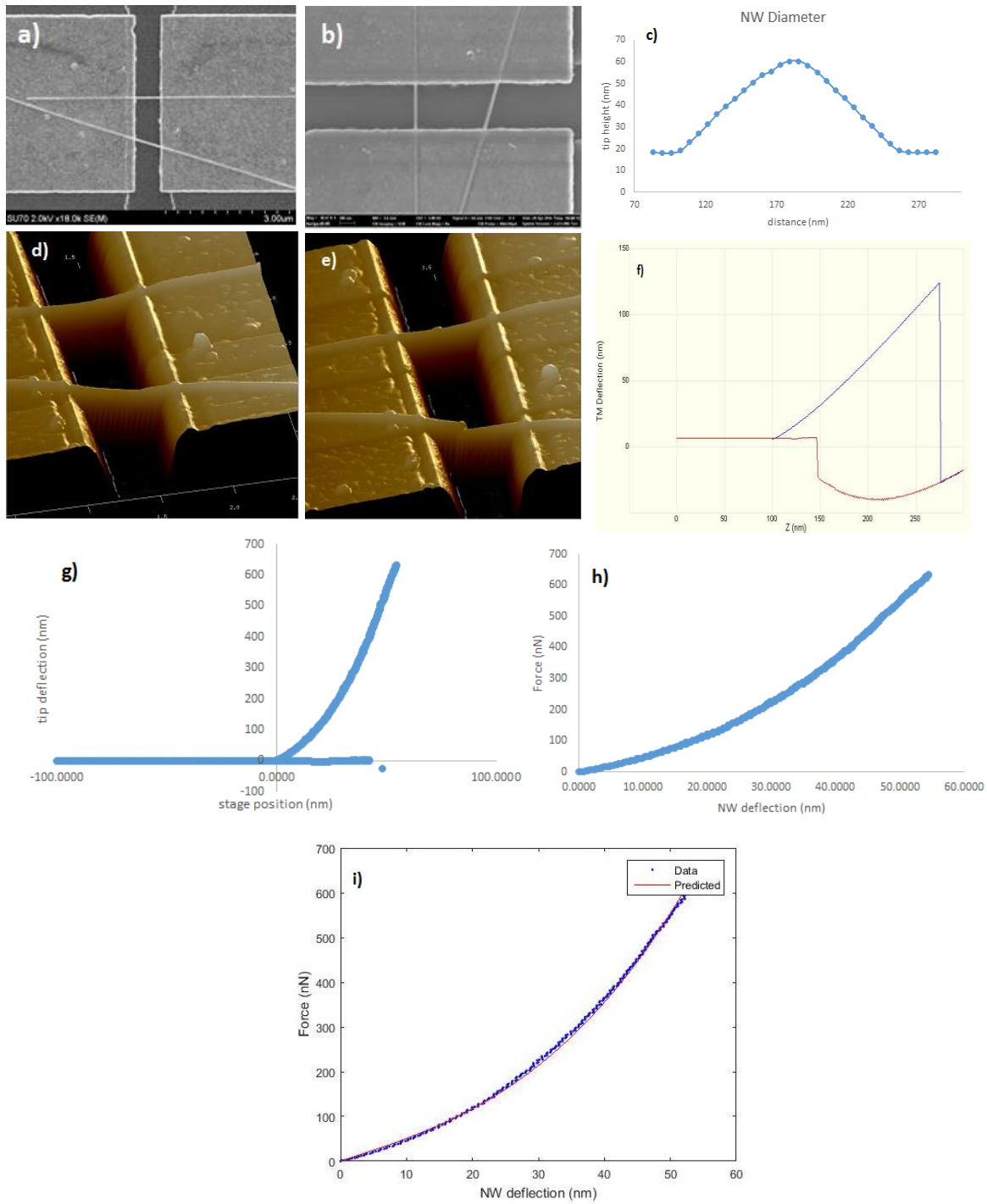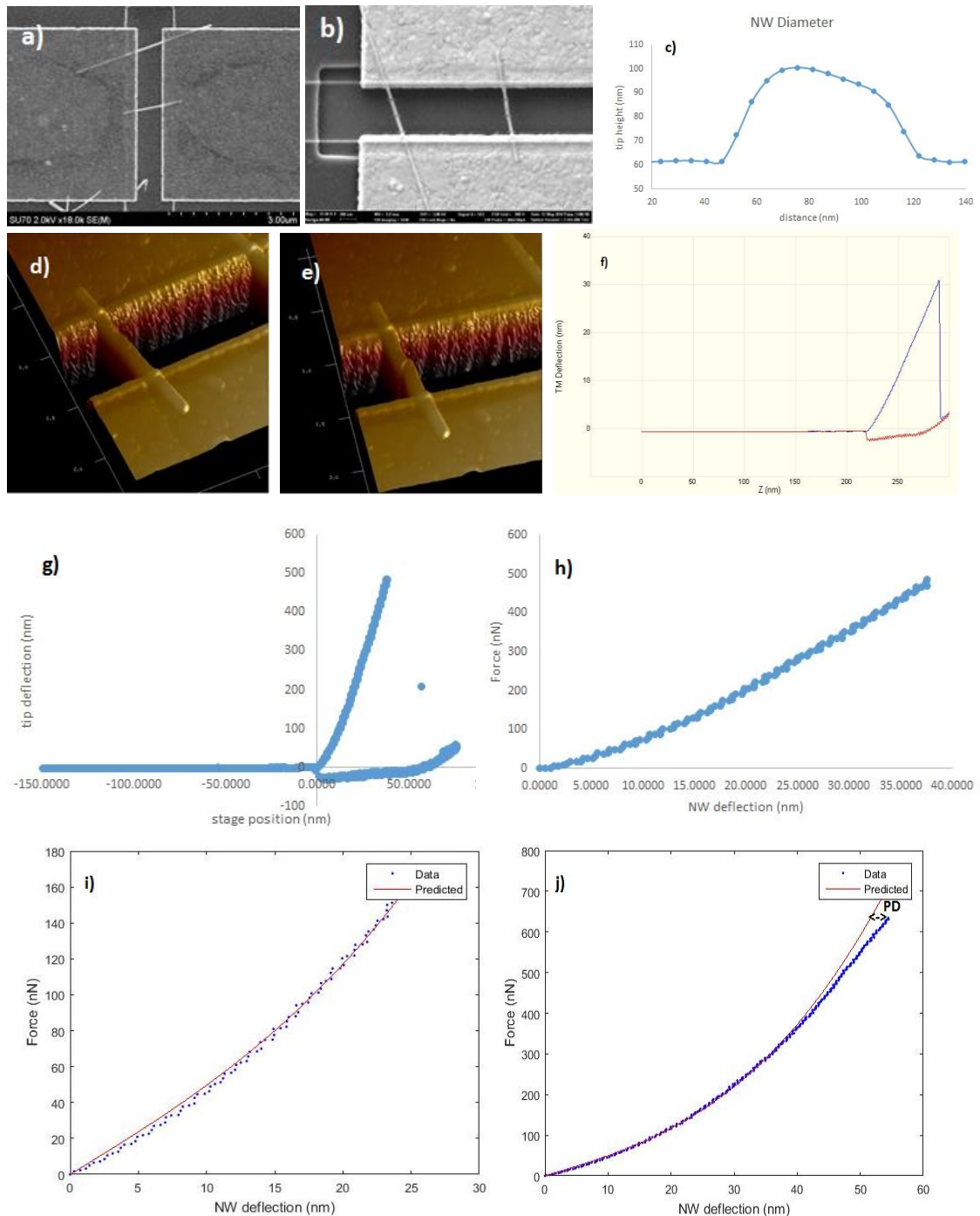
Figure 6.13: 20 Cycles Sample 4 a) SEM micrograph of NW, b) SEM micrograph of NW with EBID clamps, c) Height trace, d) 3D AFM scan of NW, e) 3D AFM scan of NW after fracture, f) Original loading-unloading curve, g) Extracted AFM loading-unloading curve showing fracture, and h) Extracted force vs displacement plot, i) YM of 48.3 GPa was extracted from Matlab curve and j) Matlab Curve fit extended up to the fracture point, undergoes plastic deformation around 3-4 nm.

6.6) Results and Discussion:
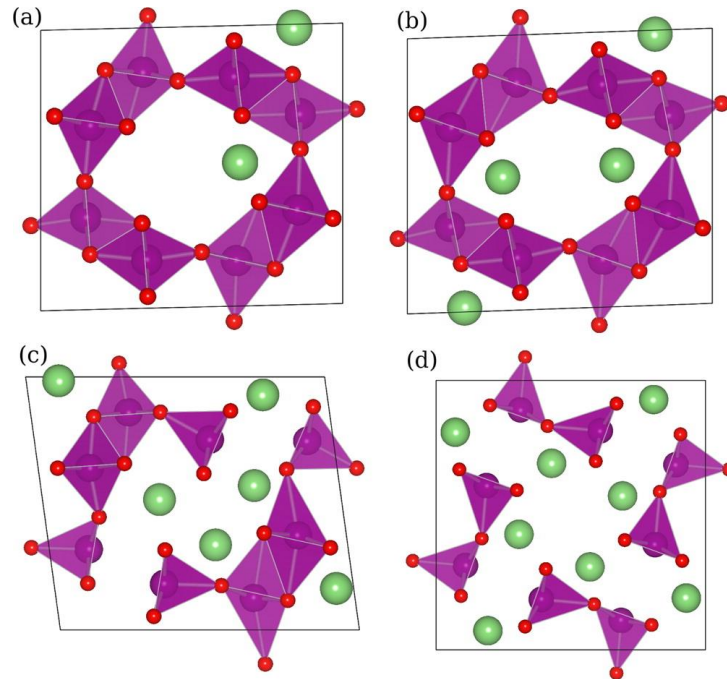
Figure 6.14: Lowest energy structures obtained for the unit cell of (a) α-$Li_{0.25}MnO_2$, (b) α-$Li_{0.5}MnO_2$, (c) α-$Li_{0.75}MnO_2$, and (d) α-Li_1MnO_2. The polyhedra are connected by Mn–O bonds of length 2.7 Å. Red spheres are oxygen, purple is manganese, and green spheres are lithium. Image reproduced from ref. [126].

During lithiation of alpha phase manganese dioxide NWs, the lithium ions prefer the low energy sites of tunnel walls and distribute uniformly to the maximum extent themselves, so as to minimize the Li-Li Coulomb repulsion energy. Lithiated α-MnO_2 is written in empirical form as α-Li_xMnO_2, and as seen in Figure 6.15, as the extent of lithiation increases, more number of lithium ions try to occupy the 2 x 2 tunnel structure along the c-axis. The resulting crystal structure changes were computationally modeled by Tompsett et. al. in ref. [126] and this is pictorially represented in Figure 6.14. At the same time, the summary of data from our nanomechanical measurements is provided in Table 6.4 below.

Table 6.4. Evolution of nanomechanical parameters as a function of NW SOC

SOC	Average Young's Modulus (GPa)	Average experimental-to-theoretical fracture strength ratio
As-synthesized	47.8 ± 6.1	76.6 ± 24.9
After first discharge	91.1 ± 27.1	47.37 ± 11.7
After first cycle	41.4 ± 9.3	44.34 ± 11.1
After 20 cycles	69.3 ± 19.5	40.6 ± 16.2

As-synthesized   *First discharge*

After 20-cycles   *After first cycle*
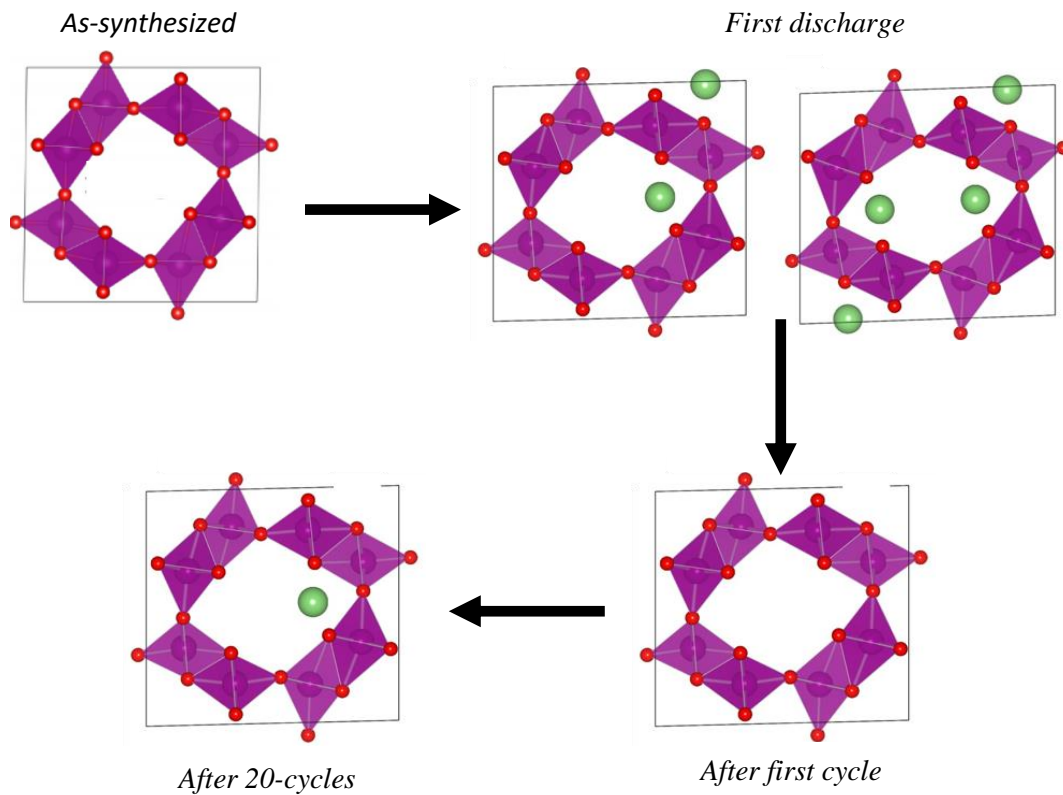
Figure 6.15: Schematic illustration of the crystal structure evolution at different SOCs. Cartoons adapted from ref. [126].

The nanomechanical changes in the electrode material, which explain the data summarized in Table 6.4, are illustrated schematically in Figure 6.15. The as-synthesized material provides a baseline for the degradation measurements and exhibits a Young's modulus (YM) and experimental-to-theoretical fracture strength ratio (ET ratio) of 47.8 GPa and 76.6%, respectively. At the end of the first discharge step, the YM increases to 91.2 GPa due to the addition of Li-O bonds that adds to the stiffness of the electrode material. However, the ET ratio drops to 47.4% due to the increase in defect density of the crystal.

On the other hand, when this intercalated lithium is extract out of the NW electrode at the end of the first cycle, the NW material relaxes to its initial YM value; however, a key difference from the as-synthesized material is the substantially lower ET ratio associated with the NWs at the end of the first cycle (44.3% vs. 76.6%). This indicates that even though the Li is extracted from the NW crystal, this insertion and de-insertion process introduces more defects as compared to the starting material. Also, the NW electrodes at the end of 20 cycles of repeated discharging and charging exhibit a YM that is higher than that of the as-synthesized material. But, at the same time the increase in YM is not as high as that observed in the NWs at the end of the first discharge step. This points to the irreversible trapping of some intercalated lithium during extended cycling of the NWs. This lithium, while it leads to an increased material stiffness, it also is a likely cause for the loss in capacity of the material with cycling. Another interesting attribute here is that this increase in stiffness of the material is not accompanied by gains in the fracture strength of the material. As observed in the data, the ET ratio remains low at 40.6% and points to the degradation

in the NW material. Electrochemical induced mechanical changes at a single nanowire level was

performed for the first time, and this is an important contribution of this dissertation.

Chapter 7. Conclusions and Recommendations

This thesis has demonstrated capabilities for integrating and characterizing single nanowire battery electrochemical cells using an on-chip platform. This platform has enabled an electrochemically correlated study on the mechanical, size and electronic conductivity changes that occur within battery electrodes during repeated and reversible lithium cycling. Degradation studies in battery electrode materials is currently an important topic in battery research, with the goal of understanding the fundamental behavior of each component over its life-cycle. These capabilities, which have been demonstrated in this thesis, are critical to determine the failure mechanisms associated with the material system, and to come up with modifications/changes to crystal structure, composition etc. that minimize such degradation mechanisms. With an increase in the usage of nanomaterials to achieve these improvements, the single nanowire degradation work presented in this study is an important contribution of my thesis to the research community. Primarily, the ET ratio calculations presented at the end of this work should be considered as a key parameter in the study of lithiated behavior of the material system by the battery research community to develop future batteries using nanotechnology.

Specifically, this dissertation has made the following key contributions: (a) integration of single nanomaterials into functional lithium cells, (b) a capability to measure the electronic conductivity of a battery electrode at a single nanoparticle level; this has been used to study the impact of electronic conductivity on the rate capability of a battery electrode, (c) a capability to measure the SOC-dependent size changes in a battery electrode, and (d) measurement of mechanical

degradation with lithium cycling in a single battery nanowire electrode for the first time. These contributions have resulted in seven co-authored journal articles and three co-authored conference contributions.

In summary, advances in energy storage technology holds the key in enabling next generation applications such as electric vehicles and integration of renewable energy sources within the electric grid system. The search for such storage devices having higher energy density, faster charge-discharge rates, low cost and long cycle-life are vital to achieve this progress. Nanotechnology has the potential to play a pivotal role in realizing these improvements in each of the battery components[199,200], an helps building a better battery by increasing the size and surface of battery electrodes[95] and moving from conventional 2D structures to 3D[201,202].

This thesis has presented some new avenues for testing and optimizing these next-generation, nano-enabled battery materials. The solutions that emerge from these capabilities, together with solutions to other challenges associated with the use of nanomaterials in batteries (such as agglomeration[203], understanding inter-particle effects[59], manufacturing difficulties[60] etc.), have the potential to play a transformative role in the insertion of batteries for future transport and electric-grid applications.

References

1.   Goodenough, J. B. & Park, K. S. The Li-ion rechargeable battery: A perspective. *J. Am. Chem. Soc.* **135,** 1167–1176 (2013).

2.   Winter, M. & Brodd, R. J. What are batteries, fuel cells, and supercapacitors? *Chem. Rev.* **104,** 4245–4269 (2004).

3.   Armand, M. & Tarascon, J.-M. Building better batteries. *Nature* **451,** 652–657 (2008).

4.   Jansen, a. . *et al.* Development of a high-power lithium-ion battery. *J. Power Sources* **81-82,** 902–905 (1999).

5.   Noorden, R. Van. The rechargeable revolution: A better battery. *Nature* **507,** 26–28 (2014).

6.   Bernardes, a. M., Espinosa, D. C. R. & Tenório, J. a S. Recycling of batteries: A review of current processes and technologies. *J. Power Sources* **130,** 291–298 (2004).

7.   Kurzweil, P. Gaston Plante' and his invention of the lead-acid battery-The genesis of the first practical rechargeable battery. *J. Power Sources* **195,** 4424–4434 (2010).

8.   Shukla, A. K., Venugopalan, S. & Hariprakash, B. Nickel-based rechargeable batteries. **100,** 125–148 (2001).

9.   Palacín, M. R. Recent advances in rechargeable battery materials: a chemist's perspective. *Chem. Soc. Rev.* **38,** 2565–2575 (2009).

10.   Spectrum-, C. A. B. Y. Xx1v.-on chemical analysis by spectrum- observations. ry. **vi,** 270–289

11.   Lisbona, D. & Snee, T. A review of hazards associated with primary lithium and lithium-ion batteries. *Process Saf. Environ. Prot.* **89,** 434–442 (2011).

12.   Balakrishnan, P. G., Ramesh, R. & Prem Kumar, T. Safety mechanisms in lithium-ion batteries. *J. Power Sources* **155,** 401–414 (2006).

13.   Xu, K. Nonaqueous liquid electrolytes for lithium-based rechargeable batteries. *Chem. Rev.* **104,** 4303–4417 (2004).

14.   Yoo, H. D., Markevich, E., Salitra, G., Sharon, D. & Aurbach, D. On the challenge of developing advanced technologies for electrochemical energy storage and conversion. *Mater. Today* **17,** 110–121 (2014).

15.   Chouhan, N. and R.-S. L. *Electrochemical technologies for energy storage and conversion.* (2010).

16.   Glaize, C. and S. G. Lithium Batteries and other Electrochemical Storage Systems. 2013–2016 (2015).

17.   Aurbach, D., Zinigrad, E., Teller, H. & Dan, P. Factors Which Limit the Cycle Life of Rechargeable Lithium (Metal) Batteries. *J. Electrochem. Soc.* **147,** 1274 (2000).

18.   Chan, C. K. *et al.* High-performance lithium battery anodes using silicon nanowires. *Nat.*

Nanotechnol. **3,** 31–35 (2008).

19. Armstrong, a. R., Armstrong, G., Canales, J., García, R. & Bruce, P. G. Lithium-ion intercalation into TiO2-B nanowires. *Adv. Mater.* **17,** 862–865 (2005).

20. Tung, S.-O., Ho, S., Yang, M., Zhang, R. & Kotov, N. a. A dendrite-suppressing composite ion conductor from aramid nanofibres. *Nat. Commun.* **6,** 6152 (2015).

21. Armand, M and J-M, T. Issues and challenges facing rechargeable lithium batteries. **414,** 359–367 (2001).

22. Winter, M., Besenhard, J. O., Spahr, M. E. & Novák, P. Insertion Electrode Materials for Rechargeable Lithium Batteries. *Adv. Mater.* **10,** 725–763 (1998).

23. Jeong, G., Kim, Y.-U., Kim, H., Kim, Y.-J. & Sohn, H.-J. Prospective materials and applications for Li secondary batteries. *Energy Environ. Sci.* **4,** 1986 (2011).

24. Hu, M., Pang, X. & Zhou, Z. Recent progress in high-voltage lithium ion batteries. *J. Power Sources* **237,** 229–242 (2013).

25. Whittingham, M. S. Lithium batteries and cathode materials. *Chem. Rev.* **104,** 4271–4301 (2004).

26. Flandrois, S. & Simon, B. Carbon materials for lithium-ion rechargeable batteries. *Carbon N. Y.* **37,** 165–180 (1999).

27. Liang, M. & Zhi, L. Graphene-based electrode materials for rechargeable lithium batteries. *J. Mater. Chem.* **19,** 5871 (2009).

28. Bouchet, R. Batteries: A stable lithium metal interface. *Nat. Nanotechnol.* **9,** 1 – 2 (2014).

29. Chen, J. Recent progress in advanced materials for lithium ion batteries. *Materials (Basel).* **6,** 156–183 (2013).

30. Besenhard, J. O., Yang, J. & Winter, M. Will advanced lithium-alloy anodes have a chance in lithium-ion batteries? *J. Power Sources* **68,** 87–90 (1997).

31. Iwamura, S. *et al.* Li-Rich Li-Si Alloy As A Lithium-Containing Negative Electrode Material Towards High Energy Lithium-Ion Batteries. *Sci. Rep.* **5,** 8085 (2015).

32. Landi, B. J., Ganter, M. J., Cress, C. D., DiLeo, R. a. & Raffaelle, R. P. Carbon nanotubes for lithium ion batteries. *Energy Environ. Sci.* **2,** 638 (2009).

33. K, M. et al. A new cathode material for batteries of high energy density. **4,** 171–174 (1981).

34. Yabuuchi, N. *et al.* Structural and Electrochemical Characterizations on Li2MnO3-LiCoO2-LiCrO2 System as Positive Electrode Materials for Rechargeable Lithium Batteries. *J. Electrochem. Soc.* **160,** A39–A45 (2012).

35. Slane, Steven M., E. J. P. Rechargeable lithium battery system. 2–5 (1990).

36. Swallow, J. G. *et al.* Chemomechanics of ionically conductive ceramics for electrical energy conversion and storage. *J. Electroceramics* **32,** 3–27 (2014).

37. Li, Z., Zhang, D. & Yang, F. Developments of lithium-ion batteries and challenges of

LiFePO4 as one promising cathode material. *J. Mater. Sci.* **44,** 2435–2443 (2009).

38. Hosono, E., Kudo, T., Honma, I., Matsuda, H. & Zhou, H. Synthesis of single crystalline spinel LiMn2O4 nanowires for a lithium ion battery with high power density. *Nano Lett.* **9,** 1045–51 (2009).

39. US Department of Commerce, N. World's Smallest Reference Material is Big Plus for Nanotechnology.

40. Plichta, E. J. & Behl, W. K. A low-temperature electrolyte for lithium and lithium-ion batteries. 192–196 (2000).

41. Johnson, L. *et al.* The role of LiO2 solubility in O2 reduction in aprotic solvents and its consequences for Li–O2 batteries. *Nat. Chem.* **6,** 1091–1099 (2014).

42. Gallagher, K. G. *et al.* Quantifying the promise of lithium–air batteries for electric vehicles. *Energy Environ. Sci.* **7,** 1555 (2014).

43. Girishkumar, G., McCloskey, B., Luntz, a. C., Swanson, S. & Wilcke, W. Lithium-air battery: Promise and challenges. *J. Phys. Chem. Lett.* **1,** 2193–2203 (2010).

44. Abraham, K. M. & Jiang, Z. A Polymer Electrolyte − Based Rechargeable Lithium / Oxygen Battery TECHNICAL PAPERS ELECTROCHEMICAL SCIENCE AND TECHNOLOGY A Polymer Electrolyte-Based Rechargeable lithium / Oxygen Battery. *J. Electrochem. Soc.* **143,** 1–5 (1996).

45. Bruce, P. G., Freunberger, S. a., Hardwick, L. J. & Tarascon, J.-M. Li–O2 and Li–S batteries with high energy storage. *Nat. Mater.* **11,** 172–172 (2011).

46. Chen, L. & Shaw, L. L. Recent advances in lithium-sulfur batteries. *J. Power Sources* **267,** 770–783 (2014).

47. Zhang, S. S. Liquid electrolyte lithium/sulfur battery: Fundamental chemistry, problems, and solutions. *J. Power Sources* **231,** 153–162 (2013).

48. Zhou, W., Xiao, X., Cai, M. & Yang, L. Polydopamine-Coated, Nitrogen-Doped, Hollow Carbon − Sulfur Double-Layered Core − Shell Structure for Improving Lithium − Sulfur Batteries. *Nano Lett.* 5250–5256 (2014). doi:dx.doi.org/10.1021/nl502238b

49. Datta, M. K. *et al.* Tin and graphite based nanocomposites: Potential anode for sodium ion batteries. *J. Power Sources* **225,** 316–322 (2013).

50. Ellis, B. L. & Nazar, L. F. Sodium and sodium-ion energy storage batteries. *Curr. Opin. Solid State Mater. Sci.* **16,** 168–177 (2012).

51. Regulatory, F. E. Energy Storage. (2013). doi:10.1002/9781118557808

52. Zu, C.-X. & Li, H. Thermodynamic analysis on energy densities of batteries. *Energy Environ. Sci.* **4,** 2614 (2011).

53. Guozhong, C. Synthesis, Properties and Applications. 1–448 (2004). doi:10.1142/p305

54. Maier, J. Nanoionics: ion transport and electrochemical storage in confined systems. *Nat. Mater.* **4,** 805–815 (2005).

55.   Lin, Y., Fang, S., Su, D., Brinkman, K. S. & Chen, F. Enhancing grain boundary ionic conductivity in mixed ionic-electronic conductors. *Nat. Commun.* **6,** 6824 (2015).

56.   Bruce, P. G., Scrosati, B. & Tarascon, J.-M. Nanomaterials for rechargeable lithium batteries. *Angew. Chem. Int. Ed. Engl.* **47,** 2930–2946 (2008).

57.   Park, M., Zhang, X., Chung, M., Less, G. B. & Sastry, A. M. A review of conduction phenomena in Li-ion batteries. *J. Power Sources* **195,** 7904–7929 (2010).

58.   Aricò, A. S., Bruce, P., Scrosati, B., Tarascon, J.-M. & van Schalkwijk, W. Nanostructured materials for advanced energy conversion and storage devices. *Nat. Mater.* **4,** 366–377 (2005).

59.   Mahmood, N. & Hou, Y. Electrode Nanostructures in Lithium-Based Batteries. *Adv. Sci.* **1,** n/a–n/a (2014).

60.   Malcolm A. Weiss, John B. Heywood, E. M. D. & Andreas Schafer, and F. F. A. ON THE ROAD IN 2020 - A life-cycle analysis of new automobile technologies. *Energy Lab. Rep.* **EL 00-003,** 3–6 to 3–14 (2000).

61.   Hopkins, B. J., Smith, K. C., Slocum, A. H. & Chiang, Y. Component-cost and performance based comparison of fl ow and static batteries. **293,** 1032–1038 (2015).

62.   Buzea, C., Pacheco, I. I. & Robbie, K. Nanomaterials and nanoparticles: sources and toxicity. *Biointerphases* **2,** MR17–R71 (2007).

63.   *Lithium-Ion Batteries: Advances and Applications*. (Newnes, 2013).

64.   Song, J. & Bazant, M. Z. Effects of Nanoparticle Geometry and Size Distribution on Diffusion Impedance of Battery Electrodes. *J. Electrochem. Soc.* **160,** A15–A24 (2013).

65.   Mozalev, A., Magaino, S. & Imai, H. The formation of nanoporous membranes from anodically oxidized aluminium and their application to Li rechargeable batteries. *Electrochim. Acta* **46,** 2825–2834 (2001).

66.   Zhang, J., Sun, Y., Yao, Y., Huang, T. & Yu, A. Lysine-assisted hydrothermal synthesis of hierarchically porous Fe2O3 microspheres as anode materials for lithium-ion batteries. *J. Power Sources* **222,** 59–65 (2013).

67.   Gulley, G. Final Report for 2014 Department of Energy Visiting Faculty Program. 1–7 (2014).

68.   Wu, H. *et al.* Stable cycling of double-walled silicon nanotube battery anodes through solid–electrolyte interphase control. *Nat. Nanotechnol.* **7,** 310–315 (2012).

69.   Zhu, X., Zhu, Y., Murali, S., Stoller, M. D. & Ruoff, R. S. Nanostructured Reduced Graphene Oxide/Fe2O3 Composite As a High-Performance Anode Material for Lithium Ion Batteries. *ACS Nano* **5,** 3333–3338 (2011).

70.   Huang, H., Zhang, W. K., Gan, X. P., Wang, C. & Zhang, L. Electrochemical investigation of TiO2/carbon nanotubes nanocomposite as anode materials for lithium-ion batteries. *Mater. Lett.* **61,** 296–299 (2007).

71.   Liu, N. *et al.* A pomegranate-inspired nanoscale design for large-volume-change lithium

battery anodes. *Nat. Nanotechnol.* **9,** 187–92 (2014).

72.   Oleshko, V. P. *et al.* Miniature all-solid-state heterostructure nanowire Li-ion batteries as a tool for engineering and structural diagnostics of nanoscale electrochemical processes. *Nanoscale* **6,** 11756–11768 (2014).

73.   Zaghib, K. *et al.* Review and analysis of nanostructured olivine-based lithium recheargeable batteries: Status and trends. *J. Power Sources* **232,** 357–369 (2013).

74.   Holtz, M. E. *et al.* Nanoscale imaging of lithium ion distribution during in situ operation of battery electrode and electrolyte. *Nano Lett.* **14,** 1453–1459 (2014).

75.   Long, J. W., Dunn, B., Rolison, D. R. & White, H. S. Three-dimensional battery architectures. *Chem. Rev.* **104,** 4463–4492 (2004).

76.   Pikul, J. H., Gang Zhang, H., Cho, J., Braun, P. V & King, W. P. High-power lithium ion microbatteries from interdigitated three-dimensional bicontinuous nanoporous electrodes. *Nat. Commun.* **4,** 1732 (2013).

77.   Gowda, S. R., Leela, A., Reddy, M., Zhan, X. & Ajayan, P. M. Building Energy Storage Device on a Single Nanowire. 3329–3333 (2011).

78.   Yi, T.-F., Xie, Y., Zhu, Y.-R., Zhu, R.-S. & Shen, H. Structural and thermodynamic stability of Li4Ti5O12 anode material for lithium-ion battery. *J. Power Sources* **222,** 448–454 (2013).

79.   Magasinski, a *et al.* High-performance lithium-ion anodes using a hierarchical bottom-up approach. *Nat. Mater.* **9,** 353–358 (2010).

80.   Martin, C. Driving change in the battery industry. *Nat. Nanotechnol.* **9,** 327–8 (2014).

81.   Zhang, H. & Braun, P. V. Three-dimensional metal scaffold supported bicontinuous silicon battery anodes. *Nano Lett.* **12,** 2778–2783 (2012).

82.   Xing, L. Y. *et al.* Improved cyclic performances of LiCoPO 4/C cathode materials for high-cell-potential lithium-ion batteries with thiophene as an electrolyte additive. *Electrochim. Acta* **59,** 172–178 (2012).

83.   Shi, S. J. *et al.* Synthesis and electrochemical performance of Li1.131Mn0.504Ni0.243Co0.122O2 cathode materials for lithium ion batteries via freeze drying. *J. Power Sources* **221,** 300–307 (2013).

84.   McArthur, M. a., Jorge, L., Coulombe, S. & Omanovic, S. Synthesis and characterization of 3D Ni nanoparticle/carbon nanotube cathodes for hydrogen evolution in alkaline electrolyte. *J. Power Sources* **266,** 365–373 (2014).

85.   McNulty, D., Buckley, D. N. & O'Dwyer, C. Synthesis and electrochemical properties of vanadium oxide materials and structures as Li-ion battery positive electrodes. *J. Power Sources* **267,** 831–873 (2014).

86.   Roy, P. & Srivastava, S. K. Nanostructured anode materials for lithium ion batteries. *J. Mater. Chem. A* **3,** 2454–2484 (2015).

87.   Peng, K. *et al.* Aligned single-crystalline Si nanowire arrays for photovoltaic applications.

Small **1,** 1062–1067 (2005).

88.   Li, C. Diameter-Controlled Growth of Single-Crystalline In 2 O 3 Nanowires and Their Electronic Properties**. *Adv. Mater.* 143–146 (2003). doi:10.1002/adma.200390029

89.   Wang, W. *et al.* Silicon Decorated Cone Shaped Carbon Nanotube Clusters for Lithium Ion Battery Anodes. *Small* **10,** 3389–3396 (2014).

90.   Park, M. S., Kang, Y. M., Wang, G. X., Dou, S. X. & Liu, H. K. The effect of morphological modification on the electrochemical properties of SnO2 nanomaterials. *Adv. Funct. Mater.* **18,** 455–461 (2008).

91.   Liu, H., Wang, G., Liu, J., Qiao, S. & Ahn, H. Highly ordered mesoporous NiO anode material for lithium ion batteries with an excellent electrochemical performance. *J. Mater. Chem.* **21,** 3046 (2011).

92.   Mai, L. *et al.* Lithiated MoO3 nanobelts with greatly improved performance for lithium batteries. *Adv. Mater.* **19,** 3712–3716 (2007).

93.   Lee, K. T. & Cho, J. Roles of nanosize in lithium reactive nanomaterials for lithium ion batteries. *Nano Today* **6,** 28–41 (2011).

94.   Etacheri, V., Marom, R., Elazari, R., Salitra, G. & Aurbach, D. Challenges in the development of advanced Li-ion batteries: a review. *Energy Environ. Sci.* **4,** 3243–3262 (2011).

95.   Liu, C. *et al.* An all-in-one nanopore battery array. *Nat. Nanotechnol.* **9,** 1031–1039 (2014).

96.   Huang, J. Y. *et al.* In situ observation of the electrochemical lithiation of a single SnO_2 nanowire electrode. *Science* **330,** 1515–1520 (2010).

97.   Sullivan, J. P. *et al.* Understanding Li-ion battery processes at the atomic- to nano-scale. *Proc. SPIE* **7683,** 76830B–76830B–11 (2010).

98.   Liu, X. H. *et al.* Anisotropic swelling and fracture of silicon nanowires during lithiation. *Nano Lett.* **11,** 3312–3318 (2011).

99.   Liu, X. H. & Huang, J. Y. In situ TEM electrochemistry of anode materials in lithium ion batteries. *Energy Environ. Sci.* **4,** 3844 (2011).

100.   Gu, M. *et al.* Probing the failure mechanism of SnO2 nanowires for sodium-ion batteries. *Nano Lett.* **13,** 5203–5211 (2013).

101.   Zhang, Y., Wang, Z., Li, Y. & Zhao, K. Lithiation of ZnO nanowires studied by in-situ transmission electron microscopy and theoretical analysis. *Mech. Mater.* (2015). doi:10.1016/j.mechmat.2015.05.004

102.   Xu, X. *et al.* In Situ Investigation of Li and Na Ion Transport with Single Nanowire Electrochemical Devices. *Nano Lett.* 150526082248002 (2015). doi:10.1021/acs.nanolett.5b00705

103.   Subramanian, a *et al.* On-chip lithium cells for electrical and structural characterization of single nanowire electrodes. *Nanotechnology* **25,** 265402 (2014).

104. Pohl, H. A. (Herbert A. 1916-1986. *Dielectrophoresis: the behavior of neutral matter in nonuniform electric fields*. (Cambridge University Press, 1978).

105. Xu, D. Simulation and experimental study of nanowire assembly by dielectrophoresis. *IEEE Trans. Nanotechnol.* **13,** 517–526 (2014).

106. Xu, D. DISS . ETH NO . 19732 OPTIMIZING DIELECTROPHORETIC ASSEMBLY FOR CARBON NANOTUBE-BASED NEMS DEVICES Doctor of Sciences. (2011).

107. Burg, B. R., Bianco, V., Schneider, J. & Poulikakos, D. Electrokinetic framework of dielectrophoretic deposition devices. *J. Appl. Phys.* **107,** 1–11 (2010).

108. Fatoyinbo, H. O., Hoettges, K. F. & Hughes, M. P. Rapid-on-chip determination of dielectric properties of biological cells using imaging techniques in a dielectrophoresis dot microsystem. *Electrophoresis* **29,** 3–10 (2008).

109. Palapati, N. K. R., Pomerantseva, E. & Subramanian, a. Single nanowire manipulation within dielectrophoretic force fields in the sub-crossover frequency regime. *Nanoscale* **7,** 3109–3116 (2015).

110. Palapati, N. K. R., Muth, A., Zhu, Y., Wang, C. & Subramanian, A. Elastic Modulus Measurements on Large Diameter Nanowires using a Nanoassembled Platform. *J. Nanotechnol. Eng. Med.* 1–20 (2014). doi:10.1115/1.4028045

111. Li, Y., Yang, J. & Song, J. Microscale characterization of coupled degradation mechanism of graded materials in lithium batteries of electric vehicles. **50,** 1445–1461 (2015).

112. Wang, C.-M. *et al.* In situ transmission electron microscopy observation of microstructure and phase evolution in a SnO_2 nanowire during lithium intercalation. *Nano Lett.* **11,** 1874–1880 (2011).

113. Bhattacharya, S., Riahi, a. R. & Alpas, A. T. In-situ observations of lithiati on/de-lithiation induced graphite damage during electrochemical cycling. *Scr. Mater.* **64,** 165–168 (2011).

114. Gregorczyk, K. E., Liu, Y., Sullivan, J. P. & Rubloff, G. W. *In Situ* Transmission Electron Microscopy Study of Electrochemical Lithiation and Delithiation Cycling of the Conversion Anode RuO_2. *ACS Nano* 6354–6360 (2013). doi:10.1021/nn402451s

115. Strelcov, E., Cothren, J., Leonard, D., Borisevich, A. Y. & Kolmakov, A. In situ SEM study of lithium intercalation in individual V\n 2\n O\n 5\n nanowires. *Nanoscale* **7,** 3022–3027 (2015).

116. Su, Q. *et al.* In Situ Transmission Electron Microscopy Investigation of the Electrochemical Lithiation-Delithiation of Individual Co9S8-Filled Carbon Nanotubes. *ACS Nano* **7,** 11379–11387 (2013).

117. McDowell, M. T., Lee, S. W., Nix, W. D. & Cui, Y. 25th anniversary article: Understanding the lithiation of silicon and other alloying anodes for lithium-ion batteries. *Adv. Mater.* **25,** 4966–4985 (2013).

118. Liu, X. H. *et al.* Lithium fiber growth on the anode in a nanowire lithium ion battery

during charging. *Appl. Phys. Lett.* **98,** 4–7 (2011).

119. Nytén, A., Abouimrane, A., Armand, M., Gustafsson, T. & Thomas, J. O. Electrochemical performance of Li2FeSiO4 as a new Li-battery cathode material. *Electrochem. commun.* **7,** 156–160 (2005).

120. Zheng, S. *et al.* In Situ Formed Lithium Sulfide / Microporous Carbon Cathodes for Lithium-Ion Batteries. *ACS Nano* **7,** 10995–11003 (2013).

121. Cui, Y. *et al.* (De) Lithiation Mechanism of Li / SeS x (x = 0 − 7) Batteries Determined by in Situ Synchrotron X - ray Di ff raction and X - ray Absorption Spectroscopy. *J. Am. Chem. Soc.* **135,** 8047–8056 (2013).

122. Zhang, W. *et al.* In Situ Electrochemical XAFS Studies on an Iron Fluoride High-Capacity Cathode Material for Rechargeable Lithium Batteries. *J. Phys. Chem. C* **117,** 11498–11505 (2013).

123. Kaus, M. *et al.* Electrochemical Delithiation/Relithiation of LiCoPO 4 : A Two-Step Reaction Mechanism Investigated by in Situ X-ray Diffraction, in Situ X-ray Absorption Spectroscopy, and ex Situ 7 Li/ 31 P NMR Spectroscopy. *J. Phys. Chem. C* **118,** 17279–17290 (2014).

124. Wei, W., Cui, X., Chen, W. & Ivey, D. G. Manganese oxide-based materials as electrochemical supercapacitor electrodes. *Chem. Soc. Rev.* **40,** 1697–1721 (2011).

125. Chen, K., Sun, C. & Xue, D. Morphology engineering of high performance binary oxide electrodes. *Phys. Chem. Chem. Phys.* **17,** 732–750 (2015).

126. Tompsett, D. A. & Islam, M. S. Electrochemistry of Hollandite α-MnO 2 : Li-Ion and Na-Ion Insertion and Li 2 O Incorporation. *Chem. Mater.* **25,** 2515–2526 (2013).

127. Gao, Y., Wang, Z., Wan, J., Zou, G. & Qian, Y. A facile route to synthesize uniform single-crystalline alpha-MnO2 nanowires. *J. Cryst. Growth* **279,** 415–419 (2005).

128. Byles, B. W., Palapati, N. K. R., Subramanian, A. & Pomerantseva, E. The role of electronic and ionic conductivities in the rate performance of tunnel structured manganese oxides in Li-ion batteries. *APL Mater.* **4,** 046108 (2016).

129. Tao, T., Ro, J., Melngailis, J., Xue, Z. & Kaesz, H. D. Focused ion beam induced deposition of platinum. *J. Vac. Sci. Technol. B Microelectron. Nanom. Struct.* **8,** 1826–1829 (1990).

130. Lee, J.-H. *et al.* The role of vacancies and defects in Na0.44MnO2 nanowire catalysts for lithium–oxygen batteries. *Energy Environ. Sci.* **5,** 9558 (2012).

131. Byles, B., Subramanian, A. & Pomerantseva, E. Acid-leached α-MnO 2 nanowires for electrochemical energy storage. **9174,** 91740Z (2014).

132. Yi, T.-F. *et al.* Recent development and application of Li4Ti5O12 as anode material of lithium ion battery. *J. Phys. Chem. Solids* **71,** 1236–1242 (2010).

133. Linden, D. Linden's Handbook of Batteries, Fourth Edition - Access Engineering from McGraw-Hill. Available at: http://accessengineeringlibrary.com/browse/lindens-handbook-of-batteries-fourth-edition. (Accessed: 10th November 2015)

134. Xu, B., Qian, D., Wang, Z. & Meng, Y. S. Recent progress in cathode materials research for advanced lithium ion batteries. *Mater. Sci. Eng. R Reports* **73,** 51–65 (2012).

135. Julien, C. M., Mauger, A., Zaghib, K. & Groult, H. Comparative Issues of Cathode Materials for Li-Ion Batteries. 132–154 (2014). doi:10.3390/inorganics2020132

136. Huang, S., Wen, Z., Zhu, X. & Gu, Z. Preparation and electrochemical performance of Ag doped Li4Ti5O12. *Electrochem. commun.* **6,** 1093–1097 (2004).

137. Ahn, S. *et al.* Development of high capacity, high rate lithium ion batteries utilizing metal fiber conductive additives. *J. Power Sources* **81-82,** 896–901 (1999).

138. Robertson, A. D., Trevino, L., Tukamoto, H. & Irvine, J. T. S. New inorganic spinel oxides for use as negative electrode materials in future lithium-ion batteries. *J. Power Sources* **81-82,** 352–357 (1999).

139. Taberna, P. L., Mitra, S., Poizot, P., Simon, P. & Tarascon, J.-M. High rate capabilities Fe3O4-based Cu nano-architectured electrodes for lithium-ion battery applications. *Nat. Mater.* **5,** 567–573 (2006).

140. Guyomard, D. Rechargeable Li1+ x Mn2 O 4/Carbon Cells with a New Electrolyte Composition Potentiostatic Studies and Application to Practical Cells. **140,** (1993).

141. Guyomard, D. The carbon/Li 1+ x Mn 2 O 4 system. **69,** 222–237 (1994).

142. Cerbelaud, M., Lestriez, B., Videcoq, a., Ferrando, R. & Guyomard, D. Understanding the Structure of Electrodes in Li-Ion Batteries: A Numerical Study. *J. Electrochem. Soc.* **162,** A1485–A1492 (2015).

143. Hu, J. *et al.* Enhanced electron coherence in atomically thin Nb3SiTe6. *Nat. Phys.* **11,** 4–10 (2015).

144. Walton, A. S. *et al.* Four-probe electrical transport measurements on individual metallic nanowires. **065204,** (2010).

145. Thelander, C. *et al.* Nanowire-based one-dimensional electronics. *October* **9,** 28–35 (2006).

146. Nolan, M., O'Callaghan, S., Fagas, G., Greer, J. C. & Frauenheim, T. Silicon nanowire band gap modification. *Nano Lett.* **7,** 34–38 (2007).

147. Cheng, Z., Liu, L., Xu, S., Lu, M. & Wang, X. Temperature Dependence of Electrical and Thermal Conduction in Single Silver Nanowire. *Sci. Rep.* **5,** 10718 (2015).

148. Lord, A. M. *et al.* Factors that determine and limit the resistivity of high-quality individual ZnO nanowires. *Nanotechnology* **24,** 435706 (2013).

149. Yang, Y. *et al.* Single nanorod devices for battery diagnostics: A case study on LiMn 2O4. *Nano Lett.* **9,** 4109–4114 (2009).

150. Tombler, T. *et al.* Reversible electromechanical characteristics of carbon nanotubes under local-probe manipulation. *Nature* **405,** 769–72 (2000).

151. Long, Y. Z. *et al.* Electrical Conductivity Studies on Individual Conjugated Polymer Nanowires: Two-Probe and Four-Probe Results. *Nanoscale Res. Lett.* **5,** 237–242 (2010).

152. Hochbaum, A. I. *et al.* Enhanced thermoelectric performance of rough silicon nanowires. *Nature* **451,** 163–167 (2008).

153. Bernal, R. A. *et al.* In Situ Electron Microscopy Four-Point Electromechanical Characterization of Freestanding Metallic and Semiconducting Nanowires. *Small* **10,** 725–733 (2014).

154. Lew, K.-K. *et al.* Structural and electrical properties of trimethylboron-doped silicon nanowires. *Appl. Phys. Lett.* **85,** 3101–3103 (2004).

155. Hao, Q., Kulikov, V. & Mirsky, V. M. Investigation of contact and bulk resistance of conducting polymers by simultaneous two- and four-point technique. *Sensors Actuators, B Chem.* **94,** 352–357 (2003).

156. Smith, P. a. *et al.* Electric-field assisted assembly and alignment of metallic nanowires. *Appl. Phys. Lett.* **77,** 1399–1401 (2000).

157. Marzi, G. De *et al.* Probing intrinsic transport properties of single metal nanowires: Direct-write contact formation using a focused ion beam. *J. Appl. Phys.* **96,** 3458–3462 (2004).

158. Okino, H. *et al.* In situ resistance measurements of epitaxial cobalt silicide nanowires on Si(110). *Appl. Phys. Lett.* **86,** 1–3 (2005).

159. NIH. ImageJ. Available at: http://imagej.nih.gov/ij/. (Accessed: 10th November 2015)

160. Gosselink, R. J. A. *et al.* Analytical protocols for characterisation of sulphur-free lignin. *Ind. Crops Prod.* **19,** 271–281 (2004).

161. Ōya, A. & Ōtani, S. Catalytic graphitization of carbons by various metals. *Carbon N. Y.* **17,** 131–137 (1979).

162. Demir, M. *et al.* Graphitic Biocarbon from Metal-Catalyzed Hydrothermal Carbonization of Lignin. *Ind. Eng. Chem. Res.* **54,** 10731–10739 (2015).

163. Palapati, N. K. R., Demir, M., Harris, C. T., Subramanian, A. & Gupta, R. B. Enhancing the Electronic Conductivity of Lignin- sourced , Sub-micron Carbon Particles. *IEEE Nanotechnol. Mater. Devices Conf.* (2015).

164. Kumagai, N., Komaba, S., Abe, K. & Yashiro, H. Synthesis of metal-doped todorokite-type MnO2 and its cathode characteristics for rechargeable lithium batteries. *J. Power Sources* **146,** 310–314 (2005).

165. TURNER, S. & BUSECK, P. R. Todorokites: A New Family of Naturally Occurring Manganese Oxides. *Science (80-.).* **212,** 1024–1027 (1981).

166. Byles, B. W., West, P., Cullen, D. A., More, K. L. & Pomerantseva, E. Todorokite-type manganese oxide nanowires as an intercalation cathode for Li-ion and Na-ion batteries. *RSC Adv.* **5,** 106265–106271 (2015).

167. Kadoma, Y., Oshitari, S., Ui, K. & Kumagai, N. Characterization and electrochemical properties of Li+ ion-exchanged products of hollandite-type Ky(Mn1 - xCox)O2 for rechargeable lithium battery electrodes. *Solid State Ionics* **179,** 1710–1713 (2008).

168. Cui, L.-F., Ruffo, R., Chan, C. K., Peng, H. & Cui, Y. Crystalline-Amorphous Core Shell Silicon Nanowires for High Capacity and High Current Battery Electrodes. *Nano Lett.* **9,** 491–5 (2009).

169. He, X. *et al.* Expansion and shrinkage of the sulfur composite electrode in rechargeable lithium batteries. *J. Power Sources* **190,** 154–156 (2009).

170. Zheng, S. *et al.* High Performance C/S Composite Cathodes with Conventional Carbonate-Based Electrolytes in Li-S Battery. *Sci. Rep.* **4,** 1–7 (2014).

171. Chan, C. K. *et al.* High Capacity Li-ion Battery Anodes using Ge Nanowires. *Nano Lett.* **8,** 307–9 (2008).

172. Zhang, W. J. A review of the electrochemical performance of alloy anodes for lithium-ion batteries. *J. Power Sources* **196,** 13–24 (2011).

173. Nithyadharseni, P., Reddy, M. V., Nalini, B. & Chowdari, B. V. R. Electrochemical investigation of SnSb nano particles for lithium-ion batteries. *Mater. Lett.* **150,** 24–27 (2015).

174. Huang, Y., Bai, X. & Zhang, Y. mechanical properties of individual ZnO nanowires and the mass measurement of nanoparticles. *J. Phys. Condens. Matter* **18,** L179–L184 (2006).

175. Zhang, H., Tang, J., Zhang, L., An, B. & Qin, L.-C. Atomic force microscopy measurement of the Young's modulus and hardness of single LaB[sub 6] nanowires. *Appl. Phys. Lett.* **92,** 173121 (2008).

176. Zhou, P., Wu, C. & Li, X. Three-point bending Young's modulus of nanowires. *Meas. Sci. Technol.* **19,** 115703 (2008).

177. Heidelberg, A. *et al.* A generalized description of the elastic properties of nanowires. *Nano Lett.* **6,** 1101–1106 (2006).

178. Kim, Y. J. *et al.* Exploring nanomechanical behavior of silicon nanowires: AFM bending versus nanoindentation. *Adv. Funct. Mater.* **21,** 279–286 (2011).

179. Guz, N., Dokukin, M., Kalaparthi, V. & Sokolov, I. If Cell Mechanics Can Be Described by Elastic Modulus: Study of Different Models and Probes Used in Indentation Experiments. *Biophys. J.* **107,** 564–575 (2014).

180. Hart, F. X. & Bates, J. B. Lattice model calculation of the strain energy density and other properties of crystalline LiCoO[sub 2]. *J. Appl. Phys.* **83,** 7560 (1998).

181. Qi, Y., Hector, L. G., James, C. & Kim, K. J. Lithium Concentration Dependent Elastic Properties of Battery Electrode Materials from First Principles Calculations. *J. Electrochem. Soc.* **161,** F3010–F3018 (2014).

182. Lee, S., Park, J., Sastry, a. M. & Lu, W. Molecular Dynamics Simulations of SOC-Dependent Elasticity of LixMn2O4 Spinels in Li-Ion Batteries. *J. Electrochem. Soc.* **160,** A968–A972 (2013).

183. Cammarata, R. C. Surface and interface stress effects in thin films. *Prog. Surf. Sci.* **46,** 1–38 (1994).

184. Miller, R. E. & Shenoy, V. B. Size-dependent elastic properties of nanosized structural elements. *Nanotechnology* **11,** 139–147 (2000).

185. Withers, J. R. & Aston, D. E. Nanomechanical measurements with AFM in the elastic limit. *Adv. Colloid Interface Sci.* **120,** 57–67 (2006).

186. Wen, B., Sader, J. E. & Boland, J. J. Mechanical properties of ZnO nanowires. *Phys. Rev. Lett.* **101,** 2–5 (2008).

187. Lee, H., Shin, W., Choi, J. W. & Park, J. Y. Nanomechanical properties of lithiated Si nanowires probed with atomic force microscopy. *J. Phys. D. Appl. Phys.* **45,** 275301 (2012).

188. Sader, J. E., Chon, J. W. M. & Mulvaney, P. Calibration of rectangular atomic force microscope cantilevers. *Rev. Sci. Instrum.* **70,** 3967–3969 (1999).

189. Ngo, L. T. *et al.* Ultimate-strength germanium nanowires. *Nano Lett.* **6,** 2964–2968 (2006).

190. Maksud, M., Yoo, J., Harris, C. T., Palapati, N. K. R. & Subramanian, A. Young ' s Modulus of [111] Germanium Nanowires.

191. Lin, Y. et. al. Compressional Behavior of Bulk and Nanorod LiMn2O4 under Nonhydrostatic Stress. *Journal, Chinese Met. Nonferrous* **18,** 1–5 (2008).

192. Jiang, Y. et. al. Preparation and Research on the Lateral Elastic Modulus of the MnO2 Nanowires. *10.4028/www.scientific.net/AMR.662.84* Available at: http://www.scientific.net/AMR.662.84.

193. Wu, B., Heidelberg, A. & Boland, J. J. Mechanical properties of ultrahigh-strength gold nanowires. *Nat. Mater.* **4,** 525–529 (2005).

194. C. R. Barrett, W. D. Nix, A. S. T. *The Principles of Engineering Materials (Prentice Hall: Englewood Cliffs, NJ, 1973).*

195. Pokluda, J. Theoretical Strength of Solids: a Bridge From Interatomic Bonds To Local Plasticity and Fracture. *Structuralintegrity.Eu* **25,** (2012).

196. West, P. & Starostina, N. A Guide to AFM Image Artifacts. *Pacific Nanotechnology-http://www. pacificnano. com/files/pdf* 15–r1076152090 (2002).

197. Marinello, F., Carmignato, S., Voltan, A., Savio, E. & De Chiffre, L. Error Sources in Atomic Force Microscopy for Dimensional Measurements: Taxonomy and Modeling. *J. Manuf. Sci. Eng.* **132,** 030903 (2010).

198. Neugirg, B. R., Koebley, S. R., Schniepp, C. & Fery, A. AFM-based mechanical characterization of single nano fi bres. 8414–8426 (2016). doi:10.1039/c6nr00863a

199. Evarts, E. C. Lithium batteries: To the limits of lithium. *Nature* **526,** S93–S95 (2015).

200. Goodenough, J. B. & Manthiram, A. A perspective on electrical energy storage. *MRS Commun.* **d,** 135–142 (2014).

201. Janicek, K. In race to improve batteries , nanotechnology provides hope. 1–4 (2016).

202. Liang, Z. *et al.* Sulfur cathodes with hydrogen reduced titanium dioxide inverse opal structure. *ACS Nano* **8,** 5249–5256 (2014).

203. de Lara, L. S., Rigo, V. A. & Miranda, C. R. The stability and interfacial properties of functionalized silica nanoparticles dispersed in brine studied by molecular dynamics. *Eur. Phys. J. B* **88,** 1–10 (2015).

Journal Articles

1) Palapati, Naveen KR, et al. "Single nanowire manipulation within dielectrophoretic force fields in the sub-crossover frequency regime." *Nanoscale* 7.7 (2015): 3109-3116.

2) Palapati, Naveen KR, et al. "Elastic Modulus Measurements on Large Diameter Nanowires Using a Nano-Assembled Platform." *Journal of Nanotechnology in Engineering and Medicine* 5.2 (2014): 021001.

3) Maksud, M., et al. "Dependence of Young's modulus on the sodium content within the structural tunnels of a one dimensional Na-ion battery cathode." Nanoscale 7.42 (2015): 17642-17648.

4) Demir, Muslum, et al. "Graphitic Biocarbon from Metal-Catalyzed Hydrothermal Carbonization of Lignin." Industrial & Engineering Chemistry Research 54.43 (2015): 10731-10739.

5) Maksud, M., et al. "Young's modulus of [111] germanium nanowires." APL Materials 3.11 (2015): 116101.

6) Byles, B. W., et al. "The role of electronic and ionic conductivities in the rate performance of tunnel structured manganese oxides in Li-ion batteries." APL Materials 4.4 (2016): 046108.

7) Hossain, Md I., et al. "Super-giant magnetoresistance at room-temperature in copper nanowires due to magnetic field modulation of potential barrier heights at nanowire-contact interfaces." Nanotechnology 27.30 (2016): 30LT02.

Conferences

1) Palapati, Naveen KR, et al. "Enhancing the Electronic Conductivity of Lignin-sourced, Sub-micron Carbon   Particles" – *IEEE NMDC conference [Anchorage, Alaska: September 2015].*

2) Demir, Muslum, et al. "Graphitic Bio-Carbon from Lignin Biomass Synthesized with Nickel Nitrate Catalyst" – 2015 AICHE Annual meeting [Salt Lake City, UT: November 2015].

3) Mechanical characterization of battery nanomaterials – Submitted – IMECE 2016.

NAVEEN KUMAR REDDY PALAPATI

300 W Franklin St Apt 301E, Richmond, Virginia, 23220 | palapatinkr@vcu.edu | Phone: 804-928-8955
www.linkedin.com/in/naveenkumarreddypalapati/

SUMMARY: - Graduate student researching in the field of nanotechnology with specialization in testing electrochemical induced mechanical, size and electrical changes in nanomaterials for battery energy applications. Fabrication of devices, material characterization, electrochemistry and Li-ion batteries are my broad areas of study. Worked as a software engineer for 2.5 years.

EDUCATION: - **Ph.D., Mechanical and Nuclear Engineering, August 2016**　　　　**GPA: 3.82/4**

Specialization: Nanotechnology, Virginia Commonwealth University, Richmond, VA

Bachelor of Technology, Mechanical Engineering, May 2008　　　**GPA: 4/4**

GRIET, Jawaharlal Nehru Technological University, India　　　**Gold Medal**

EXPERIENCE: - **CINT User: CINT, Sandia National Laboratories, New Mexico, USA**
March 2015, Summer 2013, Summer 2012

- Conducted research on a DOE user proposal in the facility, fabricated chips using advanced equipment's such as electron beam lithography, electron beam deposition etc. and performed lithiation tests on single nanowires.

Research and Teaching Assistant: Mechanical and Nuclear Eng., Virginia Commonwealth University
August 2011- Present

- Dissertation Title (July 2016): Diagnostics and Degradation Investigations of Li-Ion Battery Electrodes using Single Nanowire Electrochemical Cells
- Teaching Assistant: Dynamics - fall 2011
　　　　　Process System Dynamics - spring 2012
　　　　　Mechanics of Deformables - spring 2013
　　　　　Mechatronics lab - fall 2012; TA Advisor - fall 2013, fall 2014

Software Engineer: Tata Consultancy Services Limited (TCS), New Delhi, India
November 2008 – July 2011

- Projects: Carnival Cruise Lines (Launchpad Applications) | July 2009-July 2011
　　　　Hilton Hotels Corporation | December 2009
　　　　Software Skills Training | November 2008 – June 2009

SKILLS:-

Nanotechnology	:	Scanning electron microscope (SEM), atomic force microscope (AFM), Dielectrophoresis, probe station, glove box, electron beam lithography (EBL), transmission electron　microscope (TEM), fabrication, electrochemistry, XRD
CAD, Simulation	:	CATIA, Pro-E, ANSYS
Programming Languages	:	Matlab, Python, JMP, Latex, LabVIEW, Mathematica, VB.NET 3.5, HTML, C, C++, Visual Basic, SQL Server 2008, VSS, IBM Rational ClearCase & ClearQuest

HONOURS AND AWARDS:-

1) Alpha Epsilon Lambda – Inducted 04/29/16 (Top 1% in VCU)
2) Gold Medal – Bachelors in Mechanical Engineering – Top 20 among students from 200+ colleges
3) Lean Six Sigma Green belt certified in Tata Consultancy Services (TCS), India
4) Awarded a consolation prize by Institution of Engineers India (IEI), India for proposing a new model which can increase the power output from Low Head Natural waterfalls using Siphonic action

PUBLICATIONS:-

1) Palapati, Naveen KR, et al. "Single nanowire manipulation within dielectrophoretic force fields in the sub-crossover frequency regime." *Nanoscale* 7.7 (2015): 3109-3116.
2) Palapati, Naveen KR, et al. "Elastic Modulus Measurements on Large Diameter Nanowires Using a Nano-Assembled Platform." *Journal of Nanotechnology in Engineering and Medicine* 5.2 (2014): 021001.
3) Maksud, M., et al. "Dependence of Young's modulus on the sodium content within the structural tunnels of a one dimensional Na-ion battery cathode." Nanoscale 7.42 (2015): 17642-17648.
4) Demir, Muslum, et al. "Graphitic Biocarbon from Metal-Catalyzed Hydrothermal Carbonization of Lignin." Industrial & Engineering Chemistry Research 54.43 (2015): 10731-10739.
5) Maksud, M., et al. "Young's modulus of [111] germanium nanowires." APL Materials 3.11 (2015): 116101.
6) Byles, B. W., et al. "The role of electronic and ionic conductivities in the rate performance of tunnel structured manganese oxides in Li-ion batteries." APL Materials 4.4 (2016): 046108.
7) Hossain, Md I., et al. "Super-giant magnetoresistance at room-temperature in copper nanowires due to magnetic field modulation of potential barrier heights at nanowire-contact interfaces." Nanotechnology 27.30 (2016): 30LT02.

CONFERENCES:-

1) Palapati, Naveen KR, et al. "Enhancing the Electronic Conductivity of Lignin-sourced, Sub-micron Carbon Particles" – *IEEE NMDC conference [Anchorage, Alaska: September 2015].*
2) Demir, Muslum, et al. "Graphitic Bio-Carbon from Lignin Biomass Synthesized with Nickel Nitrate Catalyst" – 2015 AICHE Annual meeting *[Salt Lake City, UT: November 2015].*
3) Mechanical characterization of battery nanomaterials – Accepted – *IMECE 2016.*

INVENTION DISCLOSURE:-

1) Nanowire magnetic field sensor based on contact barrier modulation by a magnetic field – Submitted 05/02/16
   Contact: Dr. Supriyo Bandyopandhyay, Commonwealth Professor, VCU; Phone: 804-827-6275

LEADERSHIP | COMMUNITY SERVICE:-

1) President: Grad Mechanical and Nuclear Engineering Association (GradMNEA), VCU
2) Vice President and Secretary: Engineering Graduate Student Association (EGSA), VCU
3) Advisor, General Secretary, Webmaster, Technical Head: Tiranga-Indian Nationals at VCU
4) Member: VCU Engineering Alumni Association, VCU Engineering council, Formula SAE of VCU

5) Founder & President: Telugu@VCU
6) Volunteered in TEDxRVA 2014, Colour Run 2014, Monument 10k 2012, Broad Street Mile 2014 etc.